Master's Thesis in Biomedical Engineering

Academic year 2024/2025

Graduation Session October 2024

Different Gold Nanoparticles used to optimize DNA-PAINT microscopy

Investigation of their properties and new applications in nanomedicine

Relatore

Prof. Laura Fabris

Correlatore

Prof. Silvia Pujals Riatós

Candidato

Giorgia Rotondella

Mtr. 303995

Abstract

Gold nanoparticles (AuNPs) are widely used in nanomedicine because of their biocompatibility, stability, and ability to deliver drugs in a targeted manner. Gold, being inert and nontoxic, is ideal for clinical applications. Another aspect is their ease of functionalization, that is, the ability to easily bind biological molecules, such as proteins, nucleic acids, or polymers onto their surface. Because of their optical properties, AuNPs can be used as probes in advanced imaging techniques such as Point accumulation for Imaging in Nanoscale Topography (DNA-PAINT) microscopy. This technique consists of exploiting fluorescent molecules that temporarily bind to a target, producing intermittent signals to accurately determine the location of emitters. Binding of the imager to the target occurs via short complementary DNA sequences. The "docking strand" is attached to the particles while the "imager strand" containing the fluorophore is free in the buffer. During DNA hybridization, the imager is excited by laser light and the emission is captured resulting in a super-resolution microscopy image. In this thesis, our aim was to demonstrate how the use of AuNPs helps, with its reflection signal, to guide DNA-PAINT microscopy to where the NP is and, in the future, to be able to do dynamic and fixed assays in cells. The effectiveness of such improvements depends on the shape and size of the Nps used, and the aim is to identify the optimal configuration that offers the best performing results. To achieve this goal, we developed a DNA-PAINT imaging approach using different AuNPs, analyzing each sample separately to assess its influence on imaging performance. In the future, it will be possible to analyze multiple samples simultaneously, allowing for rapid assessment of different biological conditions, such as drug response or genetic mutations. This approach, called the 'one-pot bar-coded assay', will use unique synthetic DNA sequences as molecular 'barcodes' to localize individual nanoparticles, reducing time and resources and obtaining comprehensive data in a single experiment. In our work, we focused on the formulation and conjugation of AuNPs with docking oligonucleotides, characterizing them through analytical techniques such as Dynamic Light Scattering (DLS), Zeta Potential (ZP) and UV-VIS spectroscopy. We then used two different 'imagers strands' (one complementary to the 'docking strand' and one non-complementary) to view the different interactions by DNA-PAINT microscopy and processing the data obtained with ad hoc MatLab codes. In parallel, we conducted a study on their ability to adhere to the coverslips to allow AuNPs to remain attached to it for the extended time required during DNA-PAINT microscopy. The results of our research revealed that spherical NPs proved to be the most suitable for analysis by DNA-PAINT microscopy. On the other hand, the complex morphology of star-shaped NPs created challenges in accurate signal localization, making data interpretation less straightforward than with spherical particles. Using the images obtained, we were able to visualize the interaction between the docking strand and the corresponding imager, making it possible to conduct large-scale analyses efficiently ensuring high image resolution. The ability to directly observe these interactions provided us with valuable information about the conjugation and adhesion process, allowing us to further optimize the experimental conditions to obtain more accurate and reproducible results.

Index

1. Introduction

1.1 Nanomedicine

Nanomedicine is a field that involves many disciplines and has evolved over time. The U.S. National Nanotechnology Initiative (NNI) research and development program defined nanomedicine in 2001 [1]. The European Science Foundation (ESF) defined nanomedicine in 2004 as the science and technology that uses nanometer-sized tools, such as analytical instruments, nanoimaging, nanomaterials, and nanodevices for new therapeutic and drug delivery systems [2]. Nanomedicine is an important and innovative part of nanotechnology research and development to achieve personalized and targeted medicine (drug delivery) for the prevention, diagnosis, treatment and follow-up of many diseases. In addition, nanomedicine is potentially useful for the aforementioned medical applications as it works on biological molecules, systems, and mechanisms [3]. Nanoscience research has grown unprecedentedly in recent years. The transfer of nanomedicine into routine clinical practice requires a multidisciplinary approach and is based on a careful consideration of clinical, ethical, and societal perceptions. Numerous types of first-generation nanomedicines, such as liposomes, nanoparticles, monoclonal antibodies, and polymer-drug conjugates, have been designed and developed by scientists and companies [4]. Nanomedicine employs nanotechnology to enhance healthcare by utilizing the unique properties of materials at the nanoscale. Biological processes in the human body often occur at this level, and nanoparticles, due to their small size (1 to 100 nanometers), can potentially penetrate natural barriers and interact with biomolecules in various bodily tissues. This capability holds promise for more effective drug delivery, gene therapy, and imaging techniques. However, like other medical interventions, nanomedicine products undergo rigorous regulatory scrutiny, including extensive testing for toxicity and efficacy through clinical trials. The potential of nanomedicine to improve healthcare affordably and effectively underscores its significance in advancing medical treatments and making them more accessible to patients. [5], [6], [7]. In recent years, nanomedicine has been developed to overcome the limitations of anticancer drugs and regulate the tumor microenvironment. Vasculature and blood flow are not homogeneous among tumors, leading to uneven drug distribution within these tissues. To further enhance the targeting effect, active targeting strategies have been exploited by leveraging ligand-receptor interactions to increase nanoparticle accumulation in tumors. However, effective targeted delivery strategies with precise control are needed [8]. The surface of nanomaterials can be coated or functionalized to increase their biocompatibility and circulation time in blood and to ensure highly selective binding to the target molecule/cell. It can be said, therefore, that nanomedicine aims to improve clinical outcomes and reduce adverse side effects caused by the lack of selectivity for target tissues of small molecule drugs. [9]

1.2 Nanoparticles used in nanomedicine

The field of nanomedicine is expanding rapidly, and nanoparticles are part of it, bringing many changes and advantages over traditional medicine. Taking advantage of the permeable vascular system, when an inflammation process is occurring , nanoparticles can cross biological barriers and accumulate specifically in areas of interest [8]. Because of their size, which is comparable to that of biomolecules and cellular systems, NPs have special and remarkable physical properties. They can, for instance, encapsulate and/or adsorb a medication for therapeutic purposes or an imaging probe for monitoring or detection. Alternatively, they can be functionalized with biocompatible molecules to offer specific or selective recognition in target cells and safeguard against enzymatic and chemical

degradation. Last but not least, NPs' increased selectivity and controlled release enable the administration of drugs at lower doses, reducing toxicity in the body and increasing therapeutic efficacy while minimizing side effects [10]. Like all pharmaceuticals and medical devices, NPs are subject to strict regulations that include characterization, toxicity assessment, and multi-stage clinical trials to determine side effects and benefit/risk ratio. There are many types of NPs depending on their morphology, size, and chemical properties. Let's look at some examples of the main nanoparticles most commonly used: Lipid nanoparticles are composed of a lipid layer enclosing a cargo, such as drugs or genetic material; they are biocompatible, protect the genetic material and facilitate its delivery into target cells, enabling its release. Gold nanoparticles are used for both diagnostic and therapeutic purposes. Because of their unique optical properties, they are used in photothermal therapy, whereby exposure to light causes the particles to increase in temperature, destroying cancer cells to which they have been delivered, or in their close proximity. They can also be coated with biologically active molecules and used as imaging agents or drug carriers. Polymeric nanoparticles are made of biocompatible and biodegradable polymers. They are used for controlled and sustained release of drugs. Dendrimers are highly branched and symmetrical macromolecules with spherical morphology with a central core and a functionalized surface that allows them to interact with specific molecules. They are used to deliver drugs or genes because of their ability to enclose molecules within them. Quantum dots are semiconductor nanoparticles that fluoresce when illuminated. They are widely used in diagnostics for imaging cells and tissues. Magnetic nanoparticles, often based on iron oxide, are used for drug delivery and hyperthermic therapy, in which they are heated by an external magnetic field to destroy cancer cells. Herein, I will focus on metallic NPs as they exhibit unique optical properties. Another key aspect of metal nanoparticles is their high biocompatibility and extraordinary ease of functionalization. On the industrial applications front, metal nanoparticles exhibit remarkable catalytic properties and versatility in diagnostic techniques. They have great chemical stability, and finally, due to the possibility of using these nanoparticles to transport drugs in a targeted manner, they enable a reduction in side effects. In particular, in this thesis I will discuss metallic gold nanoparticles (AuNPs), which hold great promise in the field of nanomedicine because of their special optical, electrical, and biochemical properties, as well as their high surface functionalization adaptability and inherent gold core properties, that facilitate their application in sensing. Because of these properties, NPs can be also used for drug delivery as well as biodetection or diagnostics [11]. In biomedical research, Au NPs are extensively employed for both therapeutic and diagnostic purposes. They have optical characteristics such as the localized surface plasmon resonance (LSPR), which is their most frequently leveraged feature in medicine and diagnostics. Because of their exceptional light-to-heat conversion efficiency, Au NPs are mostly used in precision oncology, in point-of-care and biosensing applications, as well as, to a lesser degree, in therapeutics [12]. The LSPR is a phenomenon that occurs when light impinges on a noble metal nanoparticle (such as gold because of their free electron density and specific conductive properties.) and induces the collective oscillation of free electrons present on the surface of the particle. When the gold nanoparticle is irradiated by light with a specific wavelength, the surface electrons oscillate in resonance with the electromagnetic field of the light. This oscillation amplifies the intensity of the electromagnetic field near the nanoparticle surface, producing strong absorption and scattering of light. The LSPR phenomenon is responsible for the characteristic ruby red color of spherical gold nanoparticles. Due to the LSPR, gold nanoparticles respond sensitively to changes in the refractive index of their surroundings, making them ideal for the development of optical biosensors. [12]

1.3 Super- resolution microscopy

Super-resolution techniques break the diffraction limit of conventional optical microscopy by temporally or spatially modulating the excitation or activation light [13]. Super-resolution microscopy (SRM) is a technology that overcomes the diffraction limit and has revolutionized the field of cell biology since its emergence, enabling researchers to visualize cell structures with nanometer resolution, multiple colors, and single-molecule sensitivity. The impact of SRM and has extended to nanomedicine, materials science, and nanotechnology, and has given significant impetus to important discoveries in these fields. SRM has revolutionized our traditional knowledge from cell science to biological materials and cell-material interactions, transforming our understanding of the structures and functions of biological systems, shedding light on the study of bio related materials and cell-material interactions, holding great promise for clinically accurate detection and prognosis of diseases and for nanomedicine research. SRM techniques enable comprehensive observation of nanomaterial behaviors within biological environments and help provide crucial information on endocytic events, intracellular nanoparticle trafficking, therapeutic payload localization, ultimately providing a guideline for more a rational design of nanomaterials for medical applications [14]. SRM allows visualization of samples down to tens of nanometers and even at the single-molecule level due to its spatiotemporal resolution. Nanoparticle size and morphology and time-lapse tracking of drug payloads in nanoparticles can be accurately determined *in vitro* and within cells. The multicolor capability of SRM allows for labeling targets of interest and cellular compartments with different colors, thus achieving observation and localization of multiple species over cellular compartments. SRM also enables real-time *in vivo* imaging with minimal invasiveness. Because of these properties, one can directly visualize the real-time behavior of nanoparticles in response to the intracellular microenvironment and obtain dynamic interactions between nanoparticles and specific organelles. The most frequently used SRM techniques can be divided into three types: structured illumination microscopy (SIM), super-resolution microscopy using spatially patterned excitation, called stimulated emission depletion (STED), and super-resolution microscopy based on single molecule localization (SMLM). Single molecule localization microscopy (SMLM) aims to accurately detect individual fluorophores and can thus achieve the best spatial resolution down to 5 nm [15]. SMLM techniques require photoactivatable or photo commutative probes, molecule that changes its chemical or physical properties in response to a light stimulusSingle-molecule detection is based on switching between a fluorescently active state (localized) and a non-fluorescent off state (non-localized) and building the image with point-by-point super-resolution. Based on the mechanism of probes flashing between ON and OFF states, SMLM techniques are divided into three categories: (i) PALM (Photo-Activated Localization Microscopy); (ii) stochastic optical reconstruction microscopy (STORM) and direct stochastic optical reconstruction microscopy (dSTORM), which are based on photoswitching; and (iii) point accumulation for imaging in nanoscale topography (PAINT) and DNA-PAINT [16], which are based on reversible probe binding (Figure1). dSTORM is used to obtain images of subcellular structures with higher resolution than the limits of conventional optical microscopy. dSTORM can achieve resolutions on the order of 20-30 nanometers, allowing molecular details to be observed with great precision. dSTORM microscopy is based on a principle known as stochastic activation and deactivation of fluorescent molecules. Fluorescent molecules (such as fluorescent dyes or fluorescent proteins) are activated and deactivated stochastically (randomly). Under normal conditions, if all fluorescent molecules were activated at the same time, their image would appear blurry and lacking in detail due to the diffraction limit. Instead, dSTORM takes advantage of the fact that only a very limited number of fluorescent molecules are active at a given time. The imaging process consists of a series of imaging cycles, and in each cycle only a fraction of the fluorophores in the field of view are turned on, so that each of the active fluorophores is optically resolvable from the rest, that is, their images do not overlap. This approach allows for the position of these fluorophores

to be determined with high accuracy. Repeating this process for multiple cycles, each of which causing the activation of a stochastically different subset of fluorophores, allows the positions of many fluorophores to be determined and thus an overall image to be reconstructed. [17]

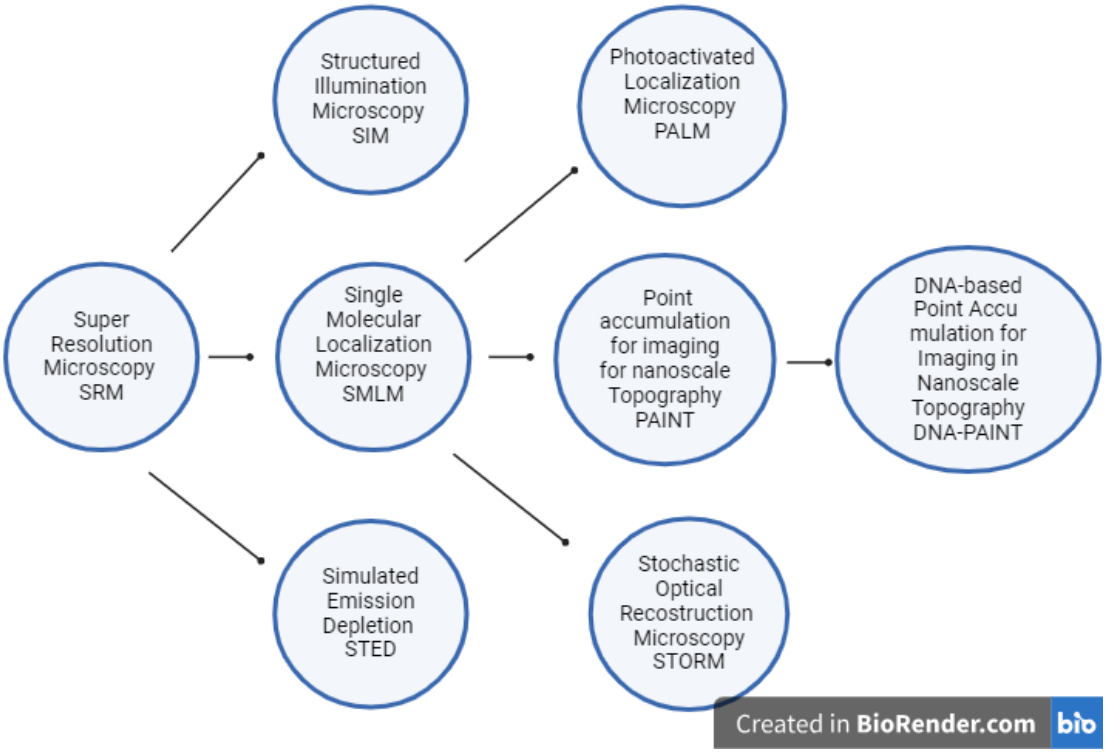

Figure 1: Diagram showing the various types of super-resolution microscopy. Image created by BioRender.

1.4 DNA-PAINT

The PAINT concept is based on the premise that fluorescent probes, targeted to a molecule of interest, diffuse freely through the solution. Once bound to the target, they are reversibly immobilized for a short time-frame and the fluorescent signal of the individual molecule appears on the camera, which can be localized by a fitting procedure. As the thermodynamics of the probe ensures dynamic binding and detachment, the fluorescent signal is turned off again until a new molecule binds, and the process can be followed kinetically. Because the probes are continuously replenished, they are not sensitive to photobleaching, which is a major advantage of this method over other SMLM techniques, allowing for longer imaging times and thus greater accuracy. In addition, by combining multiple probes with different dyes, multiplexing can be achieved. In PAINT, molecules are localized with high accuracy to each individual binding event, and thus the super-resolution map can be obtained based on the localization of each individual molecule. Following the conceptualization of the PAINT technique, another single-molecule assay was proposed for the study of DNA origami, exploiting the specific reversible binding of labeled oligonucleotides to DNA nanostructures for super-resolution imaging (DNA-PAINT) [16]. In recent years, the technique has evolved to become a standard method, and its potential has spanned a wide range of disciplines. Recent developments in DNA-PAINT have enabled spectrally unrestricted multiplexing, precise molecule counting, and ultra-high spatial resolution at the molecular scale (less than 5 nm), achieving localization accuracy of about 1 nm. DNA-PAINT can be applied to a multitude of *in vitro* and cellular applications. It is based on two short (8-10

nucleotides) and complementary single-stranded DNA sequences that can temporarily bind to each other: a "docking" strand bound to the target of interest and an "imaging" strand that serves as an affinity probe. A major advantage of this DNA-based PAINT approach is that the interaction is highly tunable in terms of specificity and affinity by changing the sequence and length of the base pair. As a result, acquisition times can be optimized, and multicolor imaging can be achieved by having a combination of specific docking/imaging pairs. DNA can be used to label a wide variety of molecules using intermediate targeting agents [18]. Although the docking filament is attached to a biological target of interest, the imager filament is conjugated to a dye docking filament that diffuses freely into the imaging buffer. Because of their complementary sequence, the imager filaments can temporarily bind to the docking filaments. During the bound state, the imager filaments are fixed in the same spot for a long period of time, allowing the camera to accumulate enough photons from the dye to detect them. The binding duration depends solely on the stability of the formed DNA duplex and can therefore be programmed. After a DNA-PAINT image has been acquired, the buffer can be swapped to introduce a different species of imager strand. Repeated imaging, washing, and reintroduction of new imager strand species thus allow researchers to create a multiplex image of many biological targets. Finally, by programming the binding duration, an extremely large number of photons can be detected from a single binding event (or blink), enabling optimal localization accuracy.

1.5 Bar-code one-pot assay – future goal

DNA-PAINT microscopy will be used in the future to identify specific barcoded particles using a process of selective hybridization between DNA strands. Specifically, this technique exploits the interaction between a docking strand, which acts as a barcode, and a complementary imager strand. Detection is accomplished by incorporating several imager strands, each of which is added sequentially, interspersed with washing steps to ensure accuracy. A significant advantage of DNA-PAINT microscopy is the ability to simultaneously analyze distinctly formulated NPs in a single experiment, meaning that all the different nanoparticles, appropriately mixed, can be evaluated simultaneously in the same container. Ultimately, this approach, known as a “one-pot bar-coded assay,” will enable not only the detection and localization of individual nanoparticles based on their barcodes, but also offer the convenience of rapid and efficient evaluation of drug-loaded nanoparticles. This method has the potential to accelerate the translation of nanoparticles into clinical practice, as it facilitates the process of evaluating and optimizing them [19] (Figure2)

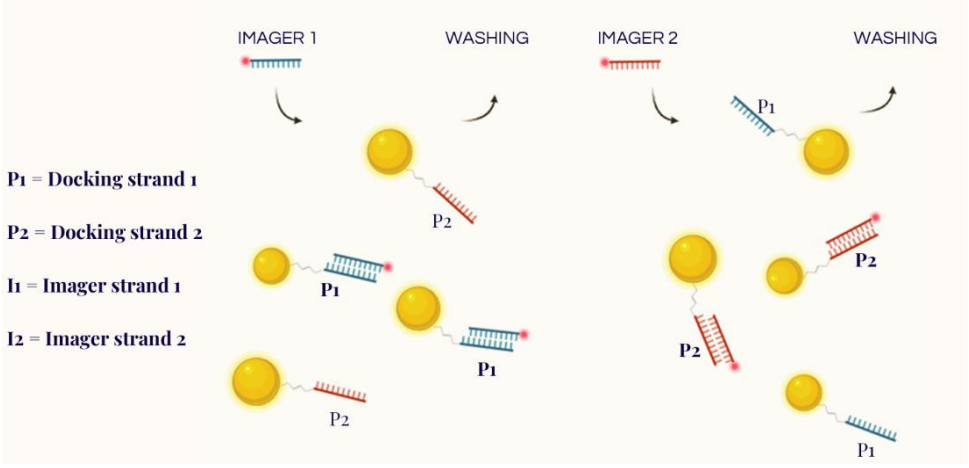

Figure 2: Scheme representing the functioning of DNA-PAINT for the detection of bar-coded NPs. Image created by BioRender

1.6 Objectives and challengers.

Our goals in this thesis are: 1) To synthetize gold nanoparticles with different shape and size. These will then be conjugated with different oligonucleotides for DNA-PAINT imaging. 2) To characterize the synthesized AuNPs before and after conjugation with oligonucleotides by DLS((Dynamic Light Scattering), ZP(Zeta Potential) and UV-Vis(Ultraviolet-Visible Spectroscopy). 3) To optimize the attachment of NPs on cover slips following different protocols and to study their optical reflection intensity. Finally, 4) the DNA-PAINT performance will be optimized with Matlab analysis. While the high flexibility of DNA is the strength of this method, it also presents challenges. Imaging strands give rise to nonspecific binding events due to charge interactions, which complicates data interpretation. In addition, the low stability of DNA within cells and target tagging within living cells are obstacles to imaging living cells. The latter obstacle requires labeling the target of interest with a docking strand, which usually means that an endogenous molecule or antibody is modified with a small strand of DNA. This approach introduces an intermediate affinity probe, which means the measurements are indirect [18]. However, many challenges must be overcome if the application of nanomedicine is to lead to improved understanding of the pathophysiological basis of diseases, to provide opportunities for more sophisticated diagnosis, and to produce more effective therapies. The goal of nanomedicine can be broadly defined as the comprehensive monitoring, repair, and improvement of all human biological systems by working from the molecular level engineered devices and nanostructures to achieve medical benefits [20]. Based on this premise, our goal is to optimize DNA-PAINT with gold nanoparticle for the future implementation of this technology in nanomedicine. We will use nanoparticles of different shapes and sizes to study such a new technique and to optimize.

2. Materials and methods

2.1 Materials

In this thesis, using specific protocols, spherical gold nanoparticles and stellate nanoparticles were synthesized. Two methods for the synthesis of gold nanostars were employed: The first is not seed-mediated and does not employ surfactants; the second, which is seed mediated, uses the surfactant TritonX-100 as a shape-directing and stabilizing agent. Gold (III) chloride trihydrate and trisodium citrate dihydrate were used for the synthesis of spherical nanoparticles, while Gold (III) chloride trihydrate, trisodium citrate dihydrate, silver nitrate ($AgNO_3$) and L-ascorbic acid were used for the synthesis of surfactant-free nanostructures. Gold chloride trihydrate, sodium borohydride ($NaBH_4$), TritonX-100, $AgNO_3$ and L-ascorbic acid were used for the synthesis of surfactant-mediated 6-arm gold nanostructures. Hydrodynamic diameter and surface charge were recorded on a Malvern Zetasizer Nano ZS analyzer. Water (RI 1.330) was chosen as the dispersing material, and the temperature was kept at 25°C. The plastic cuvette used during characterization is the ZETA Potential Sample Cell Malvern Cuvette for Particle Size Analyzer DTS1070 Disposable Folding Capillary PS Cuvette 1 / PK. Agilent's Cary 60 was used for the UV-Vis analysis. The cuvette used was made of polystyrene with a capacity of 1.5 ml. The reference oligonucleotide used as the docking strand was Thiol P1 5'-/5ThiolMC6-D/TAA TAC ATC TA- 3' with a molecular weight of 3.618 g/mol. Since thiol modifier-containing oligos are in their oxidized (disulfide) form, they require chemical reduction with tris(2-carboxyethyl) phosphine (TCEP) before each use. Phosphate buffered saline (PBS) [21] was used to suspend the DNAs at the desired concentration. After the synthesis of the nanoparticles, they were functionalized with this oligonucleotide. The functionalized nanoparticle solution was then

centrifuged using a Eppendorf 5430 R centrifuge. To analyze the nanoparticles under the microscope, they must remain attached to the 1 1/2 thick 22x22 mm cover glass from Corning. To achieve this goal, they were fixed onto rectangular microscope slides made from Superfrost ISO 8037/1 glass. (3-Aminopropyl)triethoxysilane 99% (APTES) and (3-Mercaptopropyl)trimethoxysilane 95% (MPTES) were used to bind the nanoparticles onto the cover slips. The microscope used for image acquisition at the IBEC institute in Barcelona was a Nikon NSTORM SMLM Microscope (Figure 3). All nanoparticle syntheses were performed with ultrapure MilliQ 18.2 MΩ·cm water, and the used gold was stored under vacuum after each of its uses. The 2 Imager filaments used were, 5'-/5ATTO647NN/CTA GAT GTA T-3' (I1-complementary) while the second 5'-/5ATTO647NN/TAT GTA GAT C-3' (I2-non-complementary) was used as control. All glassware was cleaned in aqua regia (HCl: HNO3= 3:1). All reagents and consumables were purchased from Merck.

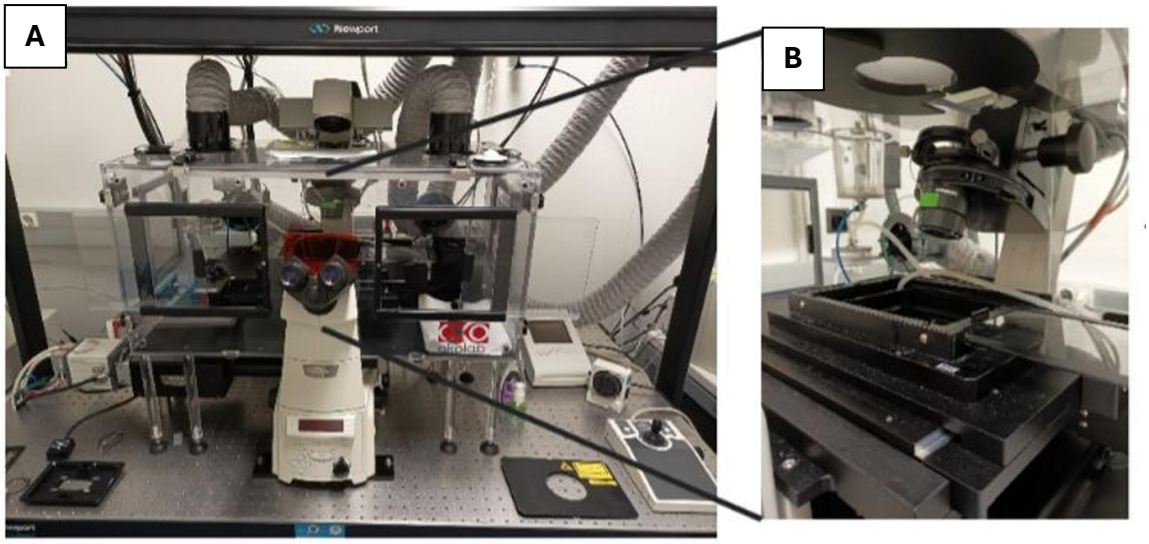

Figure 3: A) Nikon NSTORM system configured for total internal reflection Fluorescence (TIRF) and a Perfect Focus System (PFS). B) Zoom of the stage.

2.2 Methods - Synthesis of different nanoparticles

Gold nanoparticles are versatile materials with well-characterized electronic and physical properties by virtue of very well-developed synthesis processes; therefore, they find numerous applications in a variety of technological fields. In addition, their surface chemical properties can be easily modified. The interaction of gold nanoparticles with light is strongly influenced by their surroundings (electron density, solvent, molecules adsorbed on the surface), their size, and their shape. When a beam of light moves near a small particle in a liquid, the oscillating magnetic fields of light interact with free electrons on the surface of the particle. This interaction causes the electrons to move in a coordinated and rhythmic manner, in tune with the frequency of visible light. These collective electron motions are called localized surface plasmons. For small monodispersed gold nanoparticles, the phenomenon of localized surface plasmon resonance (LSPR) results in absorption of light in the blue-green portion of the spectrum (~450 nm) while red light (~700 nm) is reflected, resulting in a bright red coloration of the colloidal suspension. As the particle size increases, the wavelength of light absorbed due to the LSPR shifts toward the red (longer wavelengths). Red light is then absorbed and blue light is reflected, resulting in blue or violet solutions. The LSPR phenomenon can be modulated by varying the size or shape of the nanoparticles, thereby obtaining particles with specific optical properties for different

applications such as delivery of therapeutic agents, sensors, probes, photodynamic therapies, or diagnostics. Spherical gold nanoparticles are synthesized using reducing agents such as sodium citrate or sodium borohydride. Compared with spherical nanoparticles, the irregular "spiky" surface of gold nanostars results in a red-shifted LSPR peak and a more pronounced intensification of the scattered electric field at the tips of the spikes [22]. Functionalized gold nanoparticles are widely used in drug delivery, biological sensing, sensors and even clinical treatment [23]. Due to the extraordinary properties of gold nanoparticles, they have long been considered a potential tool for various cancer diagnosis and drug delivery applications. These properties include a high surface area/volume ratio, the presence of a localized surface plasmon resonance, the ease of functionalization with multiple moleculs, reproducible synthesis and stability. In addition, the nontoxic and nonimmunogenic nature of gold nanoparticles, in addition to the high permeability and retention effect, provide additional advantages by allowing easy penetration and accumulation of drugs at tumor sites [24]. Let us now analyze the main synthesis protocols by which I proceeded to obtain the nanoparticles of interest.

2.2.1 Spherical nanoparticles

Gold nanoparticles were synthesized by Turkevich's standard method using trisodium citrate ($Na_3C_6H_5O_7$), gold tetrachloride ($HAuCl_4$). Two solutions were prepared: the first of trisodium citrate with milliQ water (38.6 mg in 52.5 ml, 2.5 mM) while the second solution of $HAuCl_4$ in milliQ water (5.91 mg in 60 ml, 0.25 mM). Both were placed on two previously heated magnetic stirrers. A 100-mL round-bottom glass flask was used for the citrate-containing solution. This solution underwent constant temperature control by a thermometer placed inside the hole in a metal accessory (Velp Scientifica, Hemispheric Bowl for 100 ml) placed on a magnetic stirrer at 200°C at 300 rpm (rotation per minute) for 5 minutes. This action is essential to allow total dissolution of the citrate, and constant stirring is allowed by a magnetic stirbar placed inside the flask. The gold solution was also placed on a magnetic stirrer at 200°C and 300 rpm using a 100-mL glass flask. It is necessary to wait for bubbles to form on the flask wall (nucleate boiling). At this point, one must quickly add the citrate solution to the boiling gold solution. The solution changes color from colorless to dark purple in 15 minutes and then to bright red in 45 minutes. The reaction was continued for a total of 60 minutes (Figure 4) Then, the solution was removed from stirring and allowed to cool in aluminum-lined glass vials for use. Using the same procedure and same reaction times, we next tried to obtain nanospheres of larger diameter (about 70 nm) using a solution of $HAuCl_4$ at a concentration of 10^{-2} % by weight and a solution of citrate at a concentration of 1% by weight. In this case, to obtain nanoparticles of the desired size, it was necessary to add 0.30 ml of citrate solution to the gold solution after the latter was boiled down. A dark orange solution was obtained as expected (Figure 5) [25], [26].

.

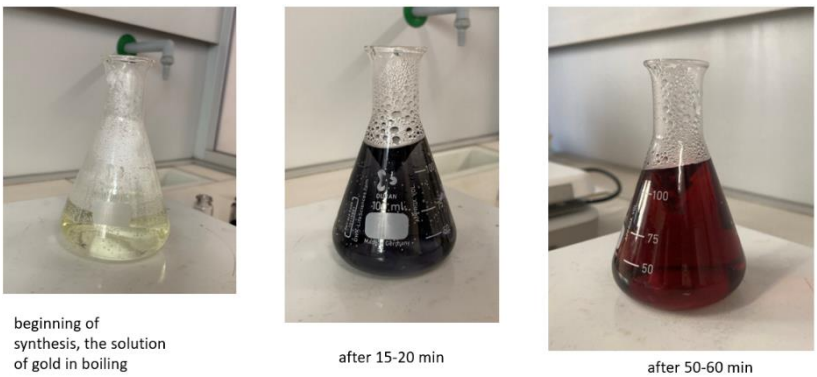

Figure 4: Steps in the procedure of synthesizing spherical gold nanoparticles between 10 and 20 nm in diameter. Color change after a given timing.


Figure 5: Steps in the procedure of synthesizing spherical gold nanoparticles of 70nm in diameter. Color change after a given timing.

2.2.2 Seedless and surfactant-free synthesis of nano stars

The protocol procedure to produce this type of nanostructure is very simple. For our purpose, it was decided to use 15ml of MilliQ 18.2 MΩ·cm water inside a 20 ml vial. We proceeded to the correct weighing of all reagents in different vials coated with aluminum to reduce photodecomposition throughout the entire synthesis. We first added 540 µL of gold ($HAuCl_4$) to the solution at a concentration of 10^{-2} M followed by 30 µL of silver nitrate ($AgNO_3$) at a concentration of 10^{-2} M. The solution, after being capped, was stirred on a vortex for 10 s at maximum speed. We then proceeded with the addition of 90 µL of ascorbic acid (L-AA) at a concentration of 10^{-1} M followed by stirring for 5 min, to stabilize to the solution while allowing the reaction to occur. This done, one can continue with maximum stirring on the vortex for 20 s. In this reaction, silver nitrate controls the length and tip of the star arms. The last step was the addition of 15 µL 1 M sodium citrate to stabilize and terminate the growth of the nano star with subsequent vortex agitation for 5 s. It is important that the citrate is well dissolved to achieve a successful colloidal solution and to avoid the formation of aggregates. For this reason, it was planned to heat the citrate for 20 min inside a hot bath at 50° and then to be used only after it was completely cooled and returned to room temperature. During such synthesis it is essential that the solution does not see light, and, for this reason, in addition to the use of aluminum around the vial, the entire synthesis was carried out inside a red light room to protect it from light. We also performed a second test using a flask so that we weighed the required citrate and then brought it up to volume with milli Q water. Doing so was thought to result in better dissolution of the citrate and thus better nanostars but no differences were noticed [27], [28].

2.2.3 Seed-mediated and surfactant-mediated nanostructures

This kind of synthesis requires the use of TritonX-100 at 0.142 M, which was first brought to volume with the use of a flask, and then shaken for dissolution. This process produces bubbles and for this reason it is important to let it rest before starting with the synthesis; therefore, this procedure is usually carried out the previous day. It is important to point out that there are two stages for this seed-based synthesis; the first in which seeds are produced and the second in which the growth of the actual nanostars takes place. First, 10 ml of TritonX are measured with a graduated cylinder and placed in the flask in which the magnet will be present to allow stirring of the solution when placed on the magnetic plate at 300 rpm. It is necessary to cover the flask with aluminum. To generate the seeds, it is necessary to add 0.1 mL of $HAuCl_4$ from a 25 mM stock into the 10 mL of 0.142 M Triton-X while

stirring for 2 min. Next, 0.6 mL of cold 0.01 M $NaBH_4$ are added, which will be needed as the reducing agent to bring Au (III) to Au (0). A color change from pale yellow to orange can be noticed as a consequence. The solution is kept stirring for 7 minutes and then allowed to cool to 4°C for 10 min. To create the stock of 0.01 M $NaBH_4$, 1.892 mg/5mL were required. Meanwhile, the flask containing pre-cooled MilliQ water inside ice was inserted. Before proceeding with the growth, the obtained seeds should be examined by a spectrophotometer at 2 specific wavelengths: 510 nm and 600 nm. The two values corresponding to these wavelengths are divided, and a value of (1.9 ±0.1) will have to be obtained in order to affirm the success of the seeds. In the second growth phase, it is necessary to use two 20-mL flasks with TritonX 100 to which 0.4 mL of 25 mM HAuCl4 are added. Then it will be necessary to add 40 µL of 0.789 M ascorbic acid (L-AA), 500 µL of AgNO3 and finally 14 µL of seeds synthesized earlier during the first phase, in quick succession within the solutions on the stirrer. Ascorbic acid is a weaker reducing agent than sodium boron hydride and thus it allows the crystal to grow more slowly, causing the nanostructures to be larger. For ascorbic acid, 69.5 mg/ 500 µL are required and for silver nitrate, 0.67 mg/ mL. We proceeded with stirring on a magnetic stirrer for 7 min and then storing the solution in a refrigerator at 4°C. Then, purification is carried out by centrifuging the product for 10 minutes at 4000 g twice; a successful synthesis allows for resuspension of the produced nanostars in water or buffer. Despite the ability to succesfully synthesize these nanostructures, it was decided not to continue with this type to carry out DNA-Paint because the presence of Triton X-100 could have hindered the successful functionalization with oligonucleotides and the subsequent optimization of the technique involved. Further studies will be needed to understand how to best remove Triton X-100 and employ these nanostars in this imaging technique.

2.2.4 Washing with aqua regia

Aqua regia, used for the removal and cleaning of all glassware that has come in contact with gold nanoparticles, consists of 3 parts hydrochloric acid and 1 part nitric acid, by volume. It is essential to prepare the aqua regia only in a fume hood and to remove all organic solvents from the vicinity. It is important to add nitric acid to hydrochloric acid and not the other way around. Then it will be sufficient to wait 10-15 minutes before use, and the colorless solution will turn red-orange with bubble formation. It is not advisable to store the solution for a long time because it becomes unstable and also do not put a lid on it because the pressure buildup may break the container. After using it, it is important to consider its disposal, to rinse all glassware with plenty of water, to collect the rinse in a beaker or a clean glass flask and to dilute 3 to 5 times its volume with water using a separate waste stream of only aqua regia or acids. The protocol used to clean the glassware consists of washing 4 times under fume hood with aqua regia, washing 8 times with distilled water under fume hood and then washing 10 times with distilled water out of the fume hood and draining into the sink. The final step consists of washing three times with MilliQ and let the glassware dry before further use [29], [30].

2.3 Characterization of AuNPs

The increasing use of engineered nanoparticles in research and product development in application areas related to medicine, sensors, environmental science, and consumer products generates a growing need to understand their properties and behaviors as they are synthesized and then applied in particular applications. It is widely recognized that as particle sizes decrease to the nanoscale, there

are a number of reasons why their physical and chemical properties differ from those associated with their bulk i.e., macroscopic form [31]. It is necessary to characterize the physicochemical properties of nanoparticles (particle size, shape, structure, chemistry, etc.) to qualify nanoparticles for use in various applications. Considering that most of the nano formulations developed or under development in research laboratories are intended for intravenous injection, understanding their characteristics is very important. As the particle size decreases, the surface area relative to volume increases dramatically, which allows for greater interaction between the particle and its surroundings. Therefore, nanoparticle size and surface area are characteristics that greatly influence the fate of a nanoparticle in the body. Nanoparticles can be administered to a patient through different routes, such as injection, inhalation, or ingestion, and can penetrate organs and tissues through endocytosis-mediated cellular uptake or other mechanisms, which depend largely on the particle size. Particle size and surface characteristics also influence their degradation, which is just as important as their uptake. The diameter of the smallest blood capillaries in the human body is about 4 μm, so for nanoparticles to reach all locations in the body, the particle diameter should be smaller. We will look at some of the most widely used techniques to characterize a nanoparticle.

2.3.1 Dynamic Light Scattering

Dynamic light scattering (DLS), is used to determine the size of nanoparticles in the colloidal suspension. DLS measures the hydrodynamic size of the particles, by analyzing the modulation of the scattered light of a laser passing through the colloidal suspension as a function of time. Brownian motion of particles is related to their hydrodynamic diameter: The smaller the particle, the faster it will scatter compared to a larger one, and the DLS tool will generate a correlation function mathematically related to particle size and its time-dependent light scattering capacity. DLS has been used to measure the particle size of dispersing colloidal samples, to study the stability of formulations, and to detect the presence of aggregation or agglomeration. DLS is the definitive tool for determining and measuring the agglomeration state of nanoparticles. DLS is an analytical technique used to measure particle size distribution across the submicron size ranges of about 0.3 nm to 10 μm. DLS measurements use scattering angles of 90 or 173 degrees using a helium-neon laser as the light source, i.e., detector position at a back angle of 173 degrees and right angle of 90 degrees to the incident light. The Brownian motion of individual particles is converted to particle size, which is calculated by the embedded software using the Stokes-Einstein equation. For this particle size measurement, a cuvette can be placed in the Nano-ZS Zetasizer. The polydispersity index (PDI) is another important parameter that describes the width or spread of the particle size distribution. In fact, the PDI value can range from 0 to 1, where colloidal particles with PDI less than 0.1 imply monodisperse particles and values greater than 0.1 can imply polydisperse particle size distributions where PDI=the square of the standard deviation divided by the average particle diameter [32]. The main limitation of DLS is that it is often difficult to accurately quantify the amounts of any aggregates that may be present, so size fractions cannot be correlated with a specific composition. For example, interferences can be caused by a range of possible artifacts (e.g., dust particles), which affect the scattering intensity with respect to smaller particles, so that they affect the scaling result. In addition, particles are considered spherical by DLS techniques, so that the actual particle size in the scattering can be underestimated. In addition, data obtained from samples containing particles with heterogeneous size distributions are difficult to interpret, as is often the case in environmental applications [33]. The cuvettes that are used are made of plastic and need a filling of about 730 microliters of colloidal solution to obtain a good

measurement. The solution was inserted by pipette and removed from the cuvette by syringe and then the solution was reused for subsequent measurements.

2.3.2 ZP

The Zeta potential is a measure of the surface charge of a nanoparticle and it is thus another parameter measured by light scattering techniques, such as light scattering by electrophoresis (ELS), also called laser Doppler microelectrophoresis. Zeta potential can be measured by taking the difference between the potential of the nanoparticle surface and the solution in which the nanoparticle resides, measured by the change in the velocity of particles moving toward an electrode by varying the electric field throughout the sample. The body's immune system prevents any foreign material from entering the body. Because nanoparticles are also foreign particles, when administered intravenously, they are recognized and phagocytosed by components of the immune system, leading to the removal of nanoparticles from the circulation. For this reason, the surface charge of nanoparticles also plays an important role as it affects the adsorption of proteins (onto the surface of nanoparticles, a process called opsonization. In addition to affecting the opsonization process, the ZP directly influences the stability of nano dispersions Therefore, it can provide a good prediction of its stability. High potentials (negative or positive) are electrically stabilized; generally, repulsive forces outweigh attractive forces, resulting in a stable system. Usually, particles with ZPs larger than ±30 mV are considered normally stable [34]. The measurement of ZP and DLS are carried out one after the other since the same instrument and cuvette are to be used. Attention must be paid to the absence of bubbles to obtain a reliable measurement and proceed with the measurement of a solution that is adequately concentrated. In the case of excessively dilute solutions, the measurement of ZP is no longer reliable [35].

2.3.3 Transmission Electron Microscopy

To verify or refute the results obtained by DLS, transmission electron microscopy (TEM) has been employed for precise measurement of nanoparticle size and distribution. TEM is the preferred method for analyzing the size and distribution of nanoparticles because it can visualize particles ranging from less than 1 nm to several micrometers. This technique is also utilized to examine the morphology of nanoparticles due to its ultra-high resolution, which enables the investigation of particle surface texture or even crystal lattice structure. In TEM, a focused electron beam passes through a sample, forming images in a manner similar to optical microscopy, but with a higher resolution due to the use of an electron source. Because of these instrumental constraints, the samples are placed on TEM grids that are inserted in a hold then is kept perpendicular to the beam inside the microscope (Figure 6). The variations in amplitude and phase of the transmitted beam create imaging contrast based on the sample's thickness and material type. TEM captures images of nanoparticles by contrasting the sample against its background. Preparing samples for TEM analysis is relatively simple and straightforward. A small drop of nanoparticles or colloidal suspension (approximately 5 µL) is placed on a TEM grid, typically made of copper with a thin carbon layer. Alternatively, the drop can be placed on a piece of parafilm, and then the grid is inverted onto the drop and left in place for a minute (Figure 7). Before use, the grids can be activated with ultraviolet radiation. The sample is then allowed to air-dry at room temperature. Once the solvent has evaporated, the grid is directly examined under TEM. TEMs operate at accelerating voltage in the range of 80 to 300 kV. In this thesis, I used a TEM with an acceleration of 100 kV which generally provides superior resolution and a flat focus with less than 0.1 percent distortion at a magnification of 150,000×[32].

When comparing data from Dynamic Light Scattering (DLS) and Transmission Electron Microscopy (TEM) images, it becomes clear whether the nanoparticles are in an aggregated or non-aggregated state. In cases where the nanoparticle suspension is well-dispersed and not aggregated, the sizes reported by both DLS and TEM will be quite similar, showing little to no variation. However, if the nanoparticles are aggregated, the particle size measured by DLS will appear significantly larger compared to the size observed through TEM analysis. This difference in size measurement helps to distinguish whether the particles are aggregated or remain as individual units within the suspension. Additionally, because TEM contrast allows to image only heavy atoms (e.g., Au), it does not enable imaging soft materials, such as organic polymers or DNA. As a consequence, in the evidence of a monodispersed suspension, the size discrepancy between TEM and DLS allows one to determine the thickness of the organic layer functionalized on the surface of the NP.

Figure 6: In the red circle is where the samples are inserted. Two TEM grids can be inserted at a time and then analyzed individually one after the other.

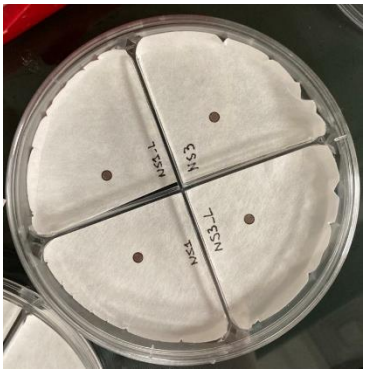

Figure 7: 4 ready-made copper TEM grids waiting to be microscopically analyzed

2.3.4 UV-Visible Spectroscopy

UV-visible spectroscopy is a fast analytical method used to measure the absorbance or transmittance of light by a sample. While UV wavelengths span from 100 to 380 nm and visible light extends up to 800 nm, most spectrophotometers operate within a wavelength range of 200 to 1100 nm. The practical range for UV-vis spectroscopy typically lies between 200 and 800 nm; wavelengths above 800 nm fall into the infrared region, while those below 200 nm are referred to as deep UV. The color of a substance is determined by its ability to absorb and emit light, with the human eye capable of distinguishing up to 10 million different colors. Light interacts with materials by passing through them (transmission), reflecting off surfaces—whether opaque or transparent—or being refracted, as

occurs in crystals. Covalently unsaturated compounds that have electronic transition energy differences matching the energy of UV-visible light will absorb light at specific wavelengths. These compounds, known as chromophores, are responsible for the colors we observe. When UV-vis light interacts with chromophores, the electrons in their ground state absorb energy and move to an excited state, a process referred to as electronic excitation. Substances like water and alcohols are generally transparent and do not absorb light in the UV-vis range, making them ideal solvents for UV-vis spectroscopy. In this technique, a light source passes through the sample, and a detector on the opposite side measures the amount of light that gets through. The resulting data is typically plotted with the baseline at the bottom, peaks pointing upward, and the x-axis showing wavelength in nanometers (nm) while the y-axis displays absorbance (A), which is unitless. The transmittance (T) can be correlated to the amount of light absorbed at each wavelength through the relationship A+T=1, with particular attention given to the highest peak in the data. UV-visible spectroscopy is based on the electronic transitions of light-absorbing organic molecules that excite electrons from a lower energy orbital (higher occupied molecular orbital, HOMO) to a higher energy unoccupied orbital (lower unoccupied molecular orbital, LUMO). The wavelength energy of the absorbed light must be equal to of the energy gap between those two orbitals, as light can be absorbed only in form on whole quanta of energy. The absorbance of light (A), is proportional to the length of the path through the sample (b) , the concentration (C), and to the extinction coefficient (ε) , which is characteristic for each compound: the Beer-Lambert law $A=\varepsilon bC$, is, as we shall see later, indispensable for calculating the moles of oligonucleotides needed to cover the surface of nanoparticles. The primary sources of error in spectrophotometry often stem from issues with sample preparation, handling, and cleaning of the cells. The cell, which is integral to the spectrophotometer's optical system, can influence accuracy depending on its composition and shape. To maintain consistency, experiments should always be conducted using the same cell. At high concentrations, certain compounds may not follow the Beer-Lambert law due to phenomena like dimerization, decomposition, aggregation, or precipitation. Despite these potential errors, UV-vis spectroscopy remains one of the simplest and most effective methods for determining the concentration of substances in a liquid. The Beer-Lambert law typically describes the relationship between absorbance and concentration accurately for most compounds up to a certain limit, often without needing a calibration curve. The cuvette used in our experiments needs a fill of at least 1 ml for the colloidal solution to pass through the laser. Our analysis was carried out at an average speed and in the absorbance range of 200 to 800 nm. To obtain the most accurate analysis possible, a baseline measurement is always taken first to verify that the instrument is working properly and then to subtract the baseline value from the measurement so that the error is reduced and the various measurements are comparable to each other [36].

2.4 Functionalization of nanoparticles with oligonucleotides

Oligonucleotides with thiol modifications are shipped by the vendors in an oxidized form, with the sulfur atoms protected in an S=S bond. Before the oligos are used, the S=S bond must be reduced to release the thiol groups. There are several methods to reduce the S=S bond, and one of them is chemical reduction with Tris (2-carboxyethyl) phosphine (TCEP) before each use. This protocol is best performed in a pH-controlled environment. It is recommended to use a buffer, such as TE buffer. After treatment, one must freeze oligonucleotides that are not used immediately to avoid oxidation and denaturation. TCEP is stored at room temperature, and one must add it in 100X excess (i.e., 30 mM TCEP per 300 μM oligo). It is not necessary to remove the TCEP from the oligo before using it in the conjugation. TCEP (Tris(2-carboxyethyl) phosphine hydrochloride, pH = 7.0, supplied by

Merck Life Sciences) was used in our experiments. The reducing agent TCEP (0.5 M) was added in a molar excess of 100x relative to the docking filament in a PBS (Phosphate-Buffered Saline, pH = 7.3) buffer solution, and left unopened and stirred at room temperature [37]. Before functionalization between oligo and nano can be carried out, it is important to resuspend the oligo as it is in a solid state inside a tube. It is centrifuged and resuspended in a TE (10 mM tris-0.1 mM EDTA) buffer that prevents DNA digestion by nucleosides at a Ph=8. Milli Q water could also be used to resuspend the DNA, but it is less accurate at the pH level. Oligonucleotide solutions can be stored for about 1 year at a temperature of -24°C. We stored the oligos at a concentration of 1 mM (range within which you need to stay is between 1 μM and 10 mM).

Gold nanoparticles can be conjugated with thiol-terminated oligonucleotides containing 10 to 100 base pairs. The synthetic oligonucleotide, after being modified so that it contains a thiol group, to attach the strand to the gold surface of the particle creates a strong Au-S covalent bond with the nanoparticles by simply mixing the two components. To do this, we need to quantify the concentration of the nanoparticle solution we synthesized. Using the spectrophotometer, one must measure the absorbance of an aliquot of aqueous solution of gold nanoparticles. Each colloidal solution, depending on the size and shape of the nanoparticles, will have an absorbance peak at different wavelengths. For example, for nanoparticles between 5 and 20 nm, the peak is at a wavelength of 520 nm. The larger the nanoparticles, the more the peak relative to the wavelength increases, even though for spherical NPs this shift is generally minimal.

To estimate the concentration of the nanoparticle suspension (cn is the concentration in M) we use the Beer-Lambert law as follows:

$$\mathrm{Cn} = \mathrm{A}(\varepsilon\mathrm{n})\mathrm{b}\ ;$$

Where εn is the molar extinction coefficient of the nanoparticle in this case at 520 nm (10-20 nm in diameter) and b is the path length of the cuvette (typically 1 cm).

To calculate the required number of moles of oligonucleotide to be conjugated to the particles, one must multiply the total surface area of the nanoparticles available for the reaction by the expected surface density of the oligonucleotide bound to the nanoparticles. For each nanoparticle synthesized, after measuring the size of the nanoparticle, one has to calculate the actual amount of oligo and consequently of TCEP to be used in order for the entire nanoparticle to be coated appropriately. The formula used is as follows:

$$mol\ conjugated = 4 \times \pi \times r^2 \times \frac{Cn}{2} \times D_0 \times V_0 \times N_0;$$

where D_0 and V_0, respectively, are given to us, N_0 i.e., Avogadro number is a const equal to 6.02×10^{23} while r and Cn must be calculated unless the nanoparticles are purchased already synthesized. Cn is the concentration of the nanoparticle solution, D_0 is the density of the oligonucleotide on each particle (~35 pmol of oligonucleotide/cm^2), V_0 is the volume of the nanoparticle solution (in L), which in our case will be 0.002 L, and r is the radius of the nanoparticles. The value used for D_0 is based on Demers et al. (2000) [39].

The radius is calculated by considering the formula for the area of a circle:

$$A = \pi r^2;$$

where the area was calculated considering the TEM images analyzed using the image J program.

The remaining part that remains to be calculated is the most complex, because to calculate the concentration Cn we will first need to calculate the molar extinction coefficient of the nanoparticle, εn.To do this, we found a method to be able to calculate this coefficient and then compared the results obtained with values in the literature for nanoparticles that have already been synthesized and put on the market. Data used are that of the protocol table 12.2.1, and the graph representation was found in the literature [38]. Experimental data and linear fit curve of the natural logarithm of the extinction coefficients versus the logarithm of the average core diameter of the nanoparticles (Figure9).

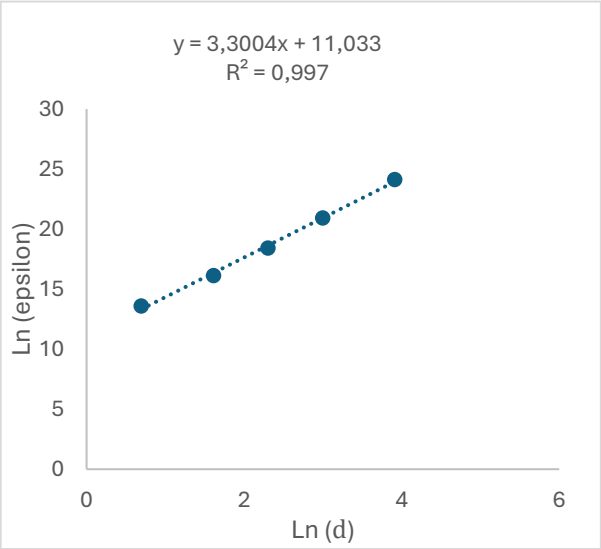

Figure 8: Linear fit curve of the natural logarithm of the extinction coefficients versus the logarithm of the average core diameter of the nanoparticles. From [38]

Using equation :

$$y= 3.3004x + 11.033;$$

the extinction coefficients were determined.

Data used are that of the protocol table 12.2.1, and the graph representation was found in the literature [38]. Experimental data and linear fit curve of the natural logarithm of the extinction coefficients versus the logarithm of the average core diameter of the nanoparticles (Figure 9).

For the calculation of the extinction coefficient, this formula was used:

$$\varepsilon n = e^{3,3004\, x \ln(d)+11,033};$$

where the values of ln(d) and ln (ε) were taken from the literature and we report them below (Table1) [40].

d (nm)	ε (M-1cm-1)	Ln d	Ln ε
2	8,00E+05	0,693147181	13,59236701
5	1,00E+07	1,609437912	16,11809565
10	1,00E+08	2,302585093	18,42068074
20	1,20E+09	2,995732274	20,90558739
50	3,00E+10	3,912023005	24,12446322

Table 1: Table of values found in literature use to obtain the previous line and then the εn

Next, Cn was calculated using the Berr-Lambert law reported above.

Given the concentration of oligo and TCEP 0.001 M and 0.005 M, respectively, it is possible to calculate the exact amount of oligo and TCEP to be used in microliters for proper functionalization of the nanoparticle.

$$\mu l\ of\ oligo = n\ mol \div concentration\ M\ ;$$

$$\mu l\ of\ TCEP = n\ mol \div concentration\ M\ ;$$

We multiplied the volume values obtained by 10 so that the amount was adequate both to cover the nanoparticle entirely and to be able to measure the amounts correctly using pipettes. To conjugate nanoparticles and oligonucleotide to the gold nanoparticle solution, we added an amount of oligonucleotide solution containing 1.5 times the moles of oligonucleotide calculated previously (i.e., an excess of 0.5 molar). Finally, we stored the conjugate solution at 4°C in the dark. The reducing agent TCEP 0.5M was added in a molar excess of 10:1 relative to the docking strand in a PBS buffer solution (Phosphate-Buffered Saline, pH = 7.3) [34], and left unopened and shaken at room temperature. The nanoparticle plus oligo solution was centrifuged in an Eppendorf centrifuge (miniSpin plus Eppendorf) using Amicon Ultra-4 filters (regenerated cellulose, M.W.C.O. 100 kDa provided by Merck Life Sciences) for 3 min at 5000 rcf at room temperature to remove excess free oligonucleotide. Once the solution was centrifuged, 3 more centrifugations with milliQ water (washing process) were performed to finish the removal of unconjugated docking filaments. Finally, NPs conjugated to P1 oligonucleotide sequences were stored in milliQ water in the dark at 4◦C. The same procedure was performed for the control with NPs as-synthetized without oligo to verify that only specific conjugation is produced [40] [9]. In practice, this procedure generates particles with a statistically distributed number of oligonucleotides attached to each particle. To perform nano functionalization with oligonucleotides, the first step is to take our oligonucleotides and react them with TCEP used as a reducing agent so that we can reduce the protective disulfide groups of the thiol group of our oligonucleotide. The TCEP was used at a concentration of 0.5 M. We mixed TCEP and oligos with a ratio of 10:1 and allowed to stir for two hours. Next, we added PBS reaching a volume of 1 ml. To that volume we added 1 ml of colloidal solution of the previously synthesized nanoparticles to reach a final volume of 2 ml. This was left stirring on the plate for another 30 min covering it with aluminum foil. After this is done, one proceeds with centrifugation of the obtained solution, so that thanks to the special filters one can remove all the excess oligos. This is done until the solution ends and then concludes with last three centrifuges with resuspension in milliQ water. Centrifugation is performed at 5000 rcf for 3 minutes each time the solution is inserted. After the centrifugation is finished, it will be necessary to recover whatever is left in the filter i.e., the now functionalized nanoparticles (Figure 8). The centrifugation process was carried out for both the functionalized nanoparticles with oligo and the synthesized nanoparticles without oligo that will serve as a control for subsequent analysis. The procedure for recovering the particles at the top of the filter

is to perform a final spin at 1100 rcf for 2 minutes only after, however, turning the filters upside down. Anything that was left in the filter will precipitate and then be recovered. The recovered portion is measured by pipette and a suitable amount of milliQ water is added for subsequent analysis. For DLS and ZP analysis, a minimum of 730 microliters is required to fill the cuvette to the correct level to obtain a result while in the case of UV-Vis, 1 ml of solution is required. For this reason, after retrieving the sample from the filter we resuspended it in 1 ml of milli Q water. Initially we tried to resuspend it directly in 2 ml to return to the initial volume from which we had started before centrifugation. In doing so, however, it was realized that the overly diluted final solution did not allow for accurate analysis, and thus it became difficult to tell whether the functionalization was successful or not. Only after analysis and obtaining suitable results was the missing volume added to ultimately reach 2 ml of colloidal solution as the starting one. The resulting solution of milli q water and nano particles with and without oligonucleotide was covered with aluminum to protect it from light and stored in a refrigerator at 4 °C [38]. Nanoparticles functionalized with oligonucleotides can then be isolated by centrifugation or gel electrophoresis.

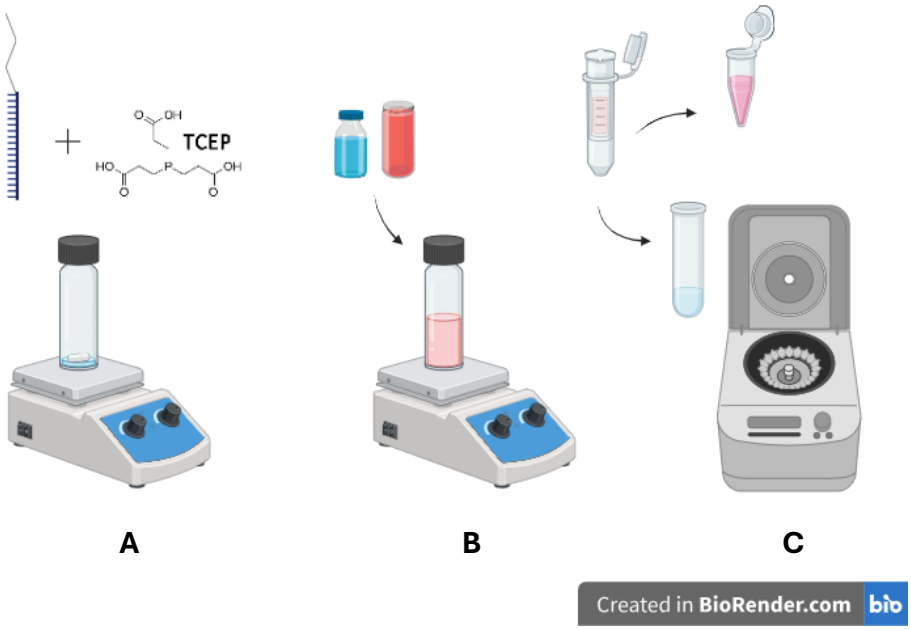

Figure 9: Oligo conjugation procedure with nanoparticles. A) 2 h of stirrer with oligo and TCEP; B) insertion of nanoparticles for another 30 min for functionalization; C) Centrifugation of sample to remove unconjugated oligo and preserve the functionalized nano

2.5 Attachment on the coverslip

In order to continue with the study, a key step is the attachment of our nanoparticles to the glass substrate i.e., the object cover slip that will be placed under the microscope lens on which our reference sample will be placed. Once the nanoparticles are placed, the important thing is that they remain attached to the slide for an extended time. Considering that the duration of the subsequent analysis by DNA-PAINT has a duration of about 25 min it is important that the nanoparticle, once docked, remains there for as long as possible. For this reason, finding a methodology and protocol that allows to attach the nanoparticles on the substrate is not at all simple. We tried different protocols that we will illustrate below but only one allowed us to get the desired result. The different protocols

allowed the attachment of nanoparticles but only for a limited time and this was visible under a microscope as the nanoparticles on the substrate seemed to float away. It was also noted that the smaller nanoparticles made it much more difficult than the larger ones to attach and stay attached. The nanoparticles to be analyzed microscopically must be resuspended again in PBS. Therefore, after centrifuging the previously resuspended solutions in water because of the characterization analysis performed on the samples, 400 microliters of solution must be centrifuged again so as to recover the nano concentrates and resuspended in 2000 microliters of PBS. These then will be the samples used for DNA-PAINT analysis. To obtain an image in DNA-PAINT microscopy, it is necessary to prepare the sample in a DNA-PAINT flow chamber. The flow chamber consists of a microscopy slide (76 x 26 mm SuperFrost Microscopy Slides) and an object cover slide (22 x 22 mm Corning Cover Glass and a thickness of 1/2) (Figure10).

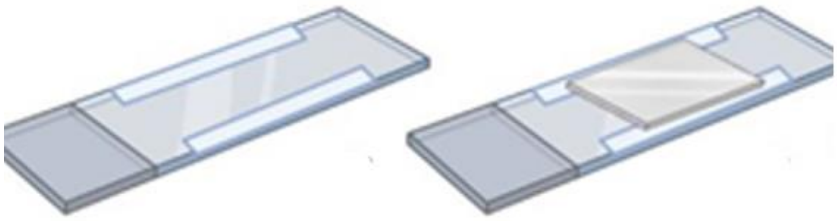

Figure 10: Example of microscopy slide and coverslip. The two lighter bands on the outside are double-sided tape to attach the coverslip.

Before assembling the flow chamber, the object cover slips were cleaned to remove impurities and improve particle attachment. What we are going to analyze in this section is the cleaning and eventual functionalization of the square glass object coverslips (Figure11). The first cleaning protocol (A1) [41] we are going to analyze is characterized by an initial immersion inside acetone and isopropyl alcohol (IPA). Then they are immersed in (3-Aminopropyl)triethoxysilane (APTES-221.37 g/mol(M), 0.946 g/ml (ρ)) 10 % v/v and IPA for between 10 and 15 min. Once this was completed, drying with nitrogen was carried out. The objective coverslips were dipped both vertically and horizontally to see if there were any differences, and none were found. The second treatment (A2) tried consisted of washing the coverslips in a methanol bath for 20 min immersed within an ultrasonic bath, then proceeding with drying with N2 and then immersing in a bath of (3-Mercaptopropyl)trimethoxysilane, (MPTMS) at 5% v/v in ethanol for 3 min, followed by rinsing with more ethanol and drying with nitrogen. The third protocol (A3), on the other hand, consisted of an initial immersion in ultrasonic bath inside potassium hidroxide KOH (0.1M) for 10 minutes, followed by washing in milliQ water for 10 minutes and bathing in ethanol for another 10. Next (A3) was a treatment with APTES for 1.5 hours and a 5% v/v concentration of the latter in methanol. After rinsing in methanol and milli Q water, everything was dried by nitrogen. The protocols A1-A2-A3, did not lead to any effective results. The nanoparticles kept coming off and floating on the object cover which actually APTES or MPTMS should have avoided. (Figure 11).

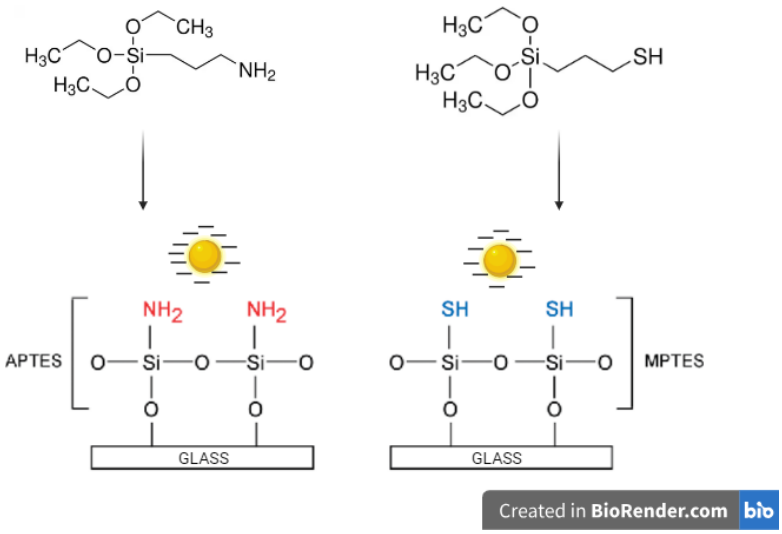

Figure 11: Different protocols of attachment, coverslip functionalized with APTES and MPTMS. Image obtained by BioRender.

Therefore, an additional protocol (A4) was sought, the steps of which we report below. The coverglass was placed in a bath of methanol and hydrochloric acid HCl 1:1 for a duration of 30 minutes. Then they were immersed in a bath of H_2SO_4 sulfuric acid for another 30 minutes. The use of such aggressive acids will have caused the glass to melt slightly and this will have allowed the nanoparticle to settle within it subsequently. After these immersions, washing in distilled water and a wash in ethanol in an ultrasonic bath for 15 min was carried out, after which nitrogen drying was done. We moved on to the use of APTES and tried two different concentrations and then noted no significant difference between the two (0.5 % and 5% v/v APTES in ethanol) for a duration of 1 hr. For the final tests, the first case i.e., 0.5% APTES was used, and every three slides used 59.700 microliters of ethanol and 300 microliters of APTES. After this time, a second wash in ethanol was performed with subsequent drying with nitrogen. After completing the cleaning procedure, this protocol involved leaving the object cover slips in contact with the colloidal nanoparticle solution overnight. A total of 600 microliters of solution were used for each object cover slip so that it was completely covered. The whole was left in the refrigerator overnight inside petri plates sealed with parafilm and with a piece of paper inside humidified with PBS preventing the sample from drying overnight [42], [43], [44], [45].

2.6 DNA Point Accumulation for Imaging in Nano scale Topography (DNA-PAINT)

The next stage of the experimental procedure involves a series of operations aimed at precise visualization of the position of gold nanoparticles and associated imager filaments. This step is performed using the advanced microscopy technique called DNA-PAINT (Point Accumulation for Imaging in Nanoscale Topography), which allows high-resolution images of the observed structures to be obtained. After the images are acquired through DNA-PAINT microscopy, the resulting data are subjected to a detailed analysis, aimed at extracting specific information about the spatial arrangement of the nanoparticles and imager filaments, thus providing a deeper understanding of their organization and interaction at the nanoscale level.

2.6.1 Sample preparation

To obtain an image through DNA-PAINT microscopy, careful sample preparation must be followed within a flow chamber specifically designed for this purpose. The flow chamber is composed of a microscopy slide, 76 x 26 mm in size, known as the SuperFrost Microscopy Slide, and a 22 x 22 mm cover glass, produced by Corning. These components must be thoroughly cleaned to ensure that there are no impurities that could interfere with the imaging process. Once cleaning of the slides is complete, the next step is to assemble the flow chamber, which is designed to hold a precise volume of 40 µL. To carry out this assembly, two strips of double-sided tape are applied over the microscopy slide, parallel to each other, in order to create the necessary space for the sample. Next, the clean coverslip is carefully placed over the strips of adhesive tape, applying light pressure to ensure proper adhesion and formation of the flow chamber [46]. There are two methods for introducing the sample into the chamber. The first method used in A1, A2 and A3 involves using a pipette to add 100 µL of a solution containing nanoparticles in PBS directly into the flow chamber (Figure 12). The second method used in A4, however, consists in inverting the coverslip which has previously been prepared with the sample solution, left to dry on its surface overnight (Figure 13). After numerous attempts, it was found that the second method provides more satisfactory and reproducible results, therefore, it was decided to exclusively use this approach in the subsequent stages. Once the presence of the nanoparticles is confirmed, well placed and firm on the surface of the slide, we proceeded with the addition of the imager filament, which is fundamental for the DNA-PAINT microscopy process. The next step involves washing the flow chamber with 100 µL of buffer B, composed of 5 mM Tris-HCl, 10 mM MgCl2, 1 mM EDTA, and 0.05% Tween-20, with a pH adjusted to 8. This wash is intended to remove unabsorbed nanoparticles that may compromise image quality. Next, a solution is prepared containing the imager filaments, I1 or I2, diluted in buffer B until the desired concentration is reached. The imager strand I1 consists of an oligonucleotide sequence of 9 nucleotide bases (5'-CTA GAT GTA T/Atto647N/3') complementary to the docking strand attached on the NP, while the imager strand I2 (5'-TAT GTA GAT C/Atto647N/ 3') is non-complementary and is used as a control sample to verify the absence of non-specific hybridization. Throughout this thesis, a 1 nM concentration of imager strands was used, with the combination of docking strand P1 and imager strand I2 as a negative control, as no specific hybridization should occur between these two strands. Finally, the flow chamber is filled by pipetting 100 µL of the buffer solution containing the prepared imager filaments, mixed with buffer B, into the flow chamber. To conclude the preparation, the coverslip is sealed with nail polish to prevent evaporation of the sample during image acquisition and rotated. This seal ensures sample stability and allows DNA-PAINT imaging to be performed efficiently, enabling accurate visualization of structures at the nanometer level.

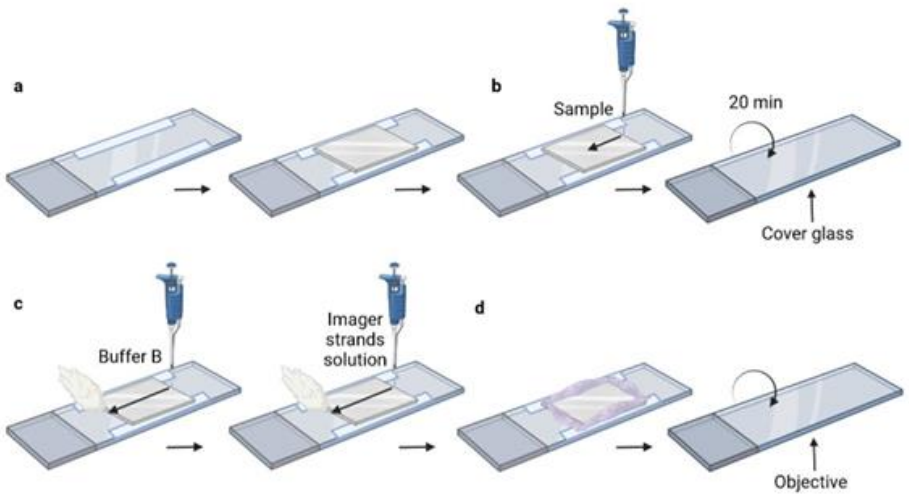

Figure 12: Steps of the procedure used for the attachment of the first method. Image obtained by BioRender.

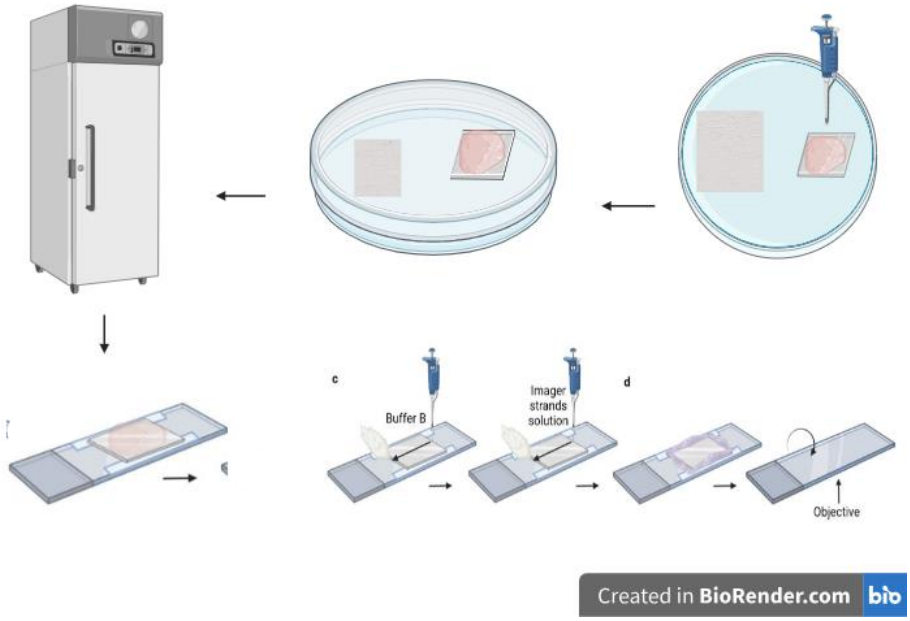

Figure 13: Steps of the procedure used for the attachment of the second method. Image obtained by BioRender.

The sample will be ready to be observed with the coverslip facing the DNA-PAINT microscopy objective [16].

2.6.2 DNA-PAINT microscopy

2.6.2 DNA-PAINT microscopy

The DNA-PAINT microscope is an extremely powerful tool that allows one to obtain detailed images of the position of nanoparticles through continuous monitoring of the localization of imager filaments labeled with the ATTO-647N fluorophore. This process allows for precise visualization of

the hybridization and subsequent disconnection of the imager filaments from the nanoparticle attachment filaments, providing crucial information on the molecular dynamics of the nanoparticles themselves (Figure14).

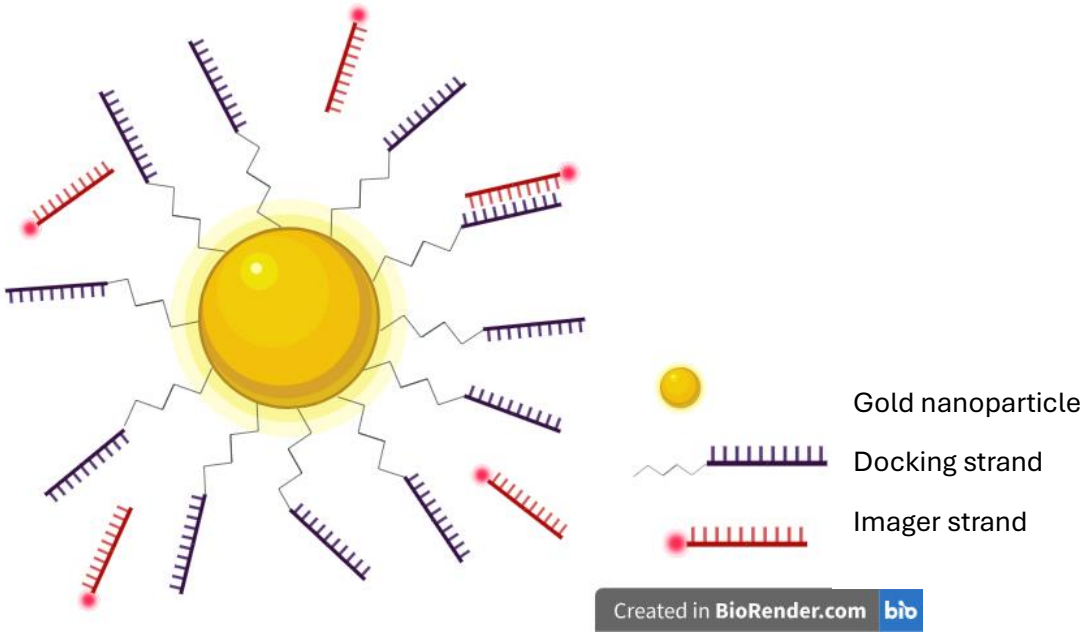

Figure 14: Scheme representing how DNA-PAINT Microscopy works on gold nanoparticles. Image created in BioRender.

DNA-PAINT imaging was performed using a Nikon N-STORM system configured for total internal reflection (TIR) microscopy and equipped with a perfect focus system (PFS). This configuration allows you to obtain high resolution images, minimizing the background and increasing the contrast of the visualized structures. To achieve these results, it was necessary to precisely adjust the angle of incidence of the lasers. In particular, the red laser with a wavelength of 647 nm and the green laser with a wavelength of 561 nm were set at an angle of approximately 60°, which allowed the background to be minimized and to illuminate only a thin sample layer, optimizing image quality. The focus of the lasers was adjusted to the minimum to ensure that the density of photons per unit area was maximized, thus improving the resolution of the final image. The signal from the Atto647N-Imager filament was collected using the 647 nm red laser, set at 60% power (160 mW), while the reflection signal of the gold nanoparticles (AuNPs) was acquired using the laser green at 561 nm, with a power of 10% (80 mW). Regarding the collection of fluorescence, a Nikon 100x objective, with a numerical aperture (NA) of 1.49, oil immersion was used, which allowed a high-quality image to be captured. The fluorescence was passed through a quadruple-band dichroic filter (97335 Nikon) to effectively separate the signals. Images were captured in a 256 x 256 pixel region, with a pixel size of 0.16 µm, using a Hamamatsu ORCA Flash 4.0 camera. The integration time for each frame was 70 milliseconds, allowing fine details to be captured and noise to be reduced. For the Atto647N-Imager filament, 20,000 frames were acquired in channel 647, and for drift correction, one frame was acquired every 100 frames in channel 561. The time taken for image acquisition was approximately 25 minutes [46].After acquisition, the first 100 frames were discarded to improve data quality, because during the first few frames, the acquisition system may not yet be completely stable, for example, the sample may move or the illumination may not be uniform. and a density filter was applied to define

the minimum localization (with a minimum count of 10) within a circle of variable radius, depending on the nanoparticle used, using the NIS-elements software. Furthermore, the data were further filtered based on the minimum number of photons detected per count, set at 15,000 for the 647 nm channel and 5,000 for the 561 nm channel, thus ensuring the reliability and precision of the final results [47], [48],[49].

2.6.3 Drift correction

One of the main problems in DNA-PAINT is drift, that is, uncontrolled displacement of the sample over time, which can be due to multiple causes, such as mechanical vibrations, thermal fluctuations, or pressure changes. Drift can introduce significant errors into measurements, degrading the quality of the final image. To correct drift, various drift correction methods are used, which can be classified into two main categories:

-Active correction: uses real-time feedback systems to keep the sample position stable during data acquisition.

-Post-acquisition correction: is based on algorithms that analyze the collected data and compensate for drift retrospectively. Post-acquisition correction methods are commonly used in DNA-PAINT and may include cross-correlation, which relies on correlation between consecutive frames to determine and correct the relative displacement of the sample over time, tracer localization, that uses fluorescent tracers (fiducials) fixed in the sample allows the drift to be monitored during acquisition (these tracers are identified in each frame and their displacement is used to calculate the drift, which is then subtracted from the signal localization data) and advanced fitting algorithms, that are statistical algorithms that use machine learning techniques or physical models to estimate and correct drift in a more sophisticated way [51].

Without accurate drift correction, the accuracy of localizations in DNA-PAINT could be compromised, significantly reducing the resolution and quality of the final image. Therefore, drift correction is an essential step to ensure the reliability of results in DNA-PAINT-based super-resolution analysis by ensuring that artifacts due to sample motion are minimized or eliminated [52].

2.7 Data analysis

Once the drift correction was carried out, the images were processed by applying specific filter parameters, using the Nis-Elements module integrated into the N-STORM system. This process improved data quality and reduced background noise, facilitating the identification of target structures. Subsequently, the processed data were saved in an appropriate format to be further analyzed using an ad hoc MatLab program, a powerful and versatile software for the quantitative and statistical analysis of the images and data collected.

2.7.1 Matlab code

To conduct the DNA-PAINT analysis on gold nanoparticles (NPs), the MatLab software was used, which played a fundamental role thanks to the use of two distinct scripts. These scripts were designed to analyze and process the x,y,t coordinates extracted from the text file (.txt), thus allowing to count the number of localizations in channels 647 (associated with the fluorescent dye ATTO-647N) and 561 (referred to to nanoparticles). The first step of the analysis involves the use of an algorithm called

"ReadCoords2.m". which obtains the drift-corrected X,Y coordinates. This algorithm was employed to identify clusters of localizations in the fiducial channel 561, which represents the reference point for determining the center of each gold nanoparticle. The clustering process is essential to distinguish the regions occupied by the nanoparticles from background noise signals, thus allowing accurate mapping of their positions. Next, a second script called "Cluster2.m" is used for the clustering phase. This script requires manual setting of specific parameters, which must be carefully selected to optimize the analysis. These parameters are essential to ensure that only localizations that actually correspond to individual nanoparticles are considered. Among these parameters are the maximum size of the nanoparticles and the minimum number of localizations necessary to form a cluster. These values are crucial to eliminate noise, aggregates or elongated structures that could compromise the accuracy of the analysis. Accordingly, the “Cluster2.m” script allows one to identify nanoparticle clusters by applying the mean shift clustering algorithm to the nanoparticle dye localizations (channel 561). The bandwidth of the algorithm must be calibrated to avoid fragmentation of nanoparticles and to separate neighboring ones. Furthermore, to further reduce the risk of erroneous detections due to false positions in the background region, a minimum number of positions has been set for a cluster to be considered valid (10 in the case of this thesis) [50]. In this thesis, the following parameters were adopted: a bandwidth of 50 nm, used as a criterion for clustering, a minimum of 10 points per cluster to ensure that a set of locations is identified as a valid cluster, and a diameter maximum particle size, variable based on the type of nanoparticle used, measured along the major axis, for the positions recorded in channel 561. The maximum distance between the particle centers, for the locations identified in channel 647, was set to 160 nanometers. Additionally, the script includes several default parameters, including a maximum ellipse stretch of 10.0 nm, an ellipse-fit scaling factor of 1.0, a minimum distance of 300 nm between clusters, and a minimum distance between clusters to ensure that they are not considered aggregated, established by the MinClustDist parameter. Finally, the software determined the number of localizations for each nanoparticle. This script also allows to validate nanoparticles based on their shape and size, thus providing some tolerance. To do this, the center of mass of each group that was not eliminated needs to be calculated and an ellipse is fitted to the positions of the molecules assigned to that group using a least squares fitting method. Clusters in which the aspect ratio of the ellipse (i.e., the ratio of the major axis to the minor axis) exceeds 1.7 or in which the major axis of the ellipse is greater than 80 nm are excluded. Finally, the script generates a histogram showing the frequency of localizations per individual nanoparticle, based on thousands of measurements taken along the imaging chain. (Attachment 1).

2.7.2 Nis-elements (N-STORM)

The reference channel corrects mechanical drift during acquisition. After removing the first 2,000 frames, a density filter is applied to obtain filtered images with Nis-Elements software [50]. Multicolored images are then created with ImageJ to distinguish the positions of each channel. The nanoparticle appears yellow, while ATTO-647N is red. The positions of channels 561 and 647 are saved in the text file for further analysis in Matlab [47]. The analysis in Matlab uses a script to count the localizations in the two channels (561 and 647) starting from the (x,y,t) coordinates. Channel 561 clusters are identified with a mean shift clustering algorithm to find the center of each NP. Subsequently, a manual filter is applied that selects the nanoparticles based on parameters such as the minimum number of localizations (10), the bandwidth (50), and the maximum diameter (with a margin of 40-50 nm compared to the NP). Finally, channel 647 localizations within 160 nm of the

NP center are analyzed, calculating the number, coordinates, and diameter of each NP. The radius of the NP is estimated as the distance from the center that includes 90% of the cluster locations.

3. Results and discussion

3.1 Synthesis of gold nanoparticles

In this thesis, I successfully synthesized nanoparticles of various shapes and sizes, specifically focusing on spherical and star-shaped nanoparticles. The colloidal suspension exhibited distinct color variations depending on the size and shape of the nanoparticles. For the spherical nanoparticles, we observed that the colloidal solution displayed a deep red color when the particles were smaller in size. As the size of the spherical nanoparticles increased, the color of the solution shifted to a more orange-pink. In contrast, the colloidal solution containing star-shaped nanoparticles consistently presented an intense blue color, regardless of the size of the particles (Figure15A-B). By meticulously following the protocols detailed earlier in the methods section, we were able to obtain nanoparticles with a range of sizes, specifically 16 nm, 19 nm, and 70 nm. The spherical nanoparticles were obtained following a reduction process of metal salts in the presence of a reducing agent, sodium citrate which leads to the nucleation and subsequent growth of the metal nuclei until the formation of spherical particles. Key parameters that influence the final size of the nanoparticles include the concentration of the metal precursor, the rate of addition of the reducing agent, the reaction temperature, and the concentration of stabilizers or surfactants. The latter, in our case citrate, play a crucial role in controlling particle growth, stabilizing newly formed nanoparticles and preventing their aggregation. For example, by increasing the concentration of the metal precursor or decreasing the concentration of stabilizer, an increase in the size of the nanoparticles can be obtained, as observed in the case of the larger spherical particles, which brought about a chromatic variation of the colloidal solution, going from an intense red to a pink-orange. Star-shaped nanoparticles, on the other hand, were synthesized using a similar method, but with different reaction conditions that favor anisotropic growth, leading to the formation of branched structures typical of stellate morphology. In this case, the presence of surfactants or directional agents is particularly important, since they can influence the growth rate of the various crystalline planes of the nanoparticle, determining their final shape. The concentration of the reducing agent can be modulated to obtain particles with more or less pronounced ramifications, influencing their shape and optical properties. Star-shaped nanoparticles have a different plasmonic response than spherical ones, with absorption extending towards longer wavelengths, which is why the colloidal solution of star-shaped nanoparticles had a deep blue color. These size variations were confirmed through several characterization techniques, including UV-Vis absorption spectroscopy, dynamic light scattering (DLS), zeta potential (ZP) measurements, and transmission electron microscopy (TEM). These methods provided comprehensive insights into the size distribution, surface charge, and morphological characteristics of the synthesized nanoparticles, which will be analyzed in detail in the subsequent sections.

A

Figure 15 A :Gold nanoparticles in colloidal solution: in red the spherical nanoparticles(10-20nm) and in blue the star-shaped nanoparticles (>70 nm).

B

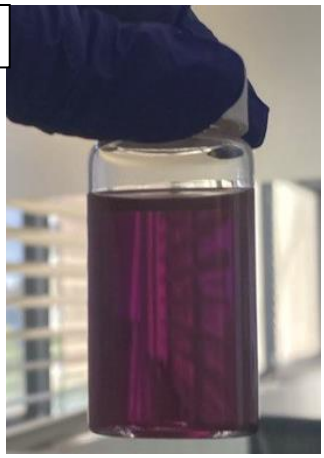

Figure 15 B: Gold nanoparticles in colloidal solution; the spherical nanoparticles (70nm)

3.2 TEM

We report below some of the images obtained by TEM microscopy of our spherical and star-shaped nanoparticles. Shots were taken both considering different points in the grid of the same sample and using different magnifications of the point under investigation. The areas of the particles were measured using the image J program, and after collecting all the excel data, we proceeded to calculate the diameters and average them to get an approximate idea of the avearge size of the particle. The magnifications considered for the images below are 500k , 200k and 100k (Figure 28-32) [54].

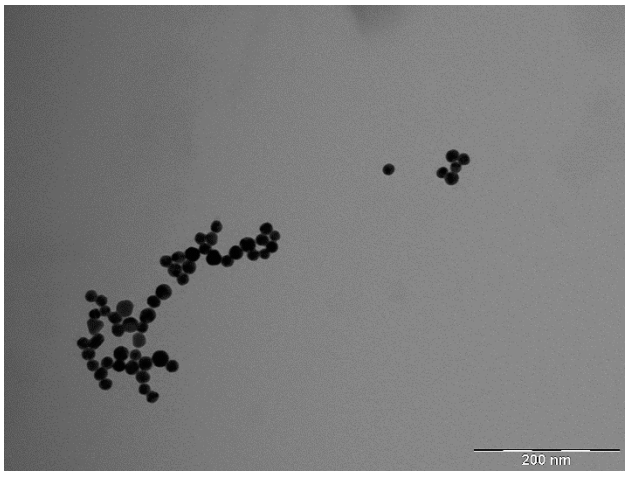

Figure 28: Spherical nanoparticles of 19nm seen by TEM microscopy at 200k magnification

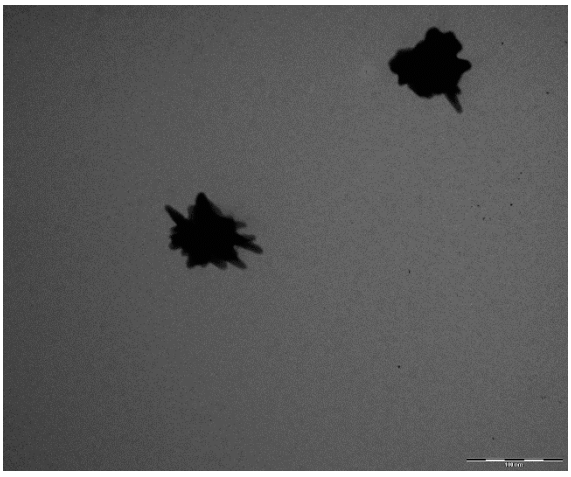

Figure 29: Star-Shape nanoparticles seen by TEM microscopy at 100nm magnification

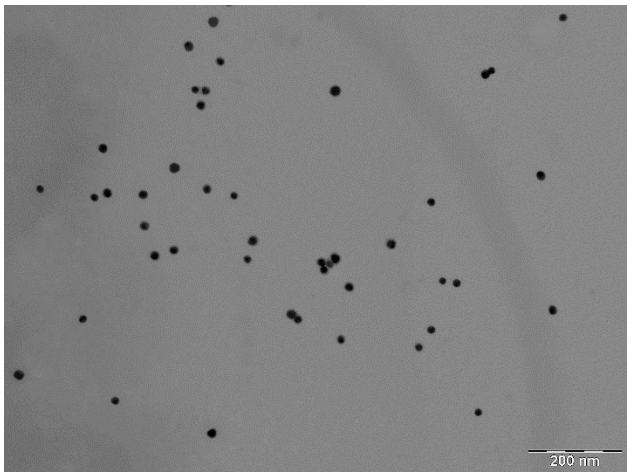

Figure 30: Spherical nanoparticles of 16nm seen by TEM microscopy at 200k magnification

Figure31: Star-Shape nanoparticles of 19nm seen by TEM microscopy at 500nm magnification

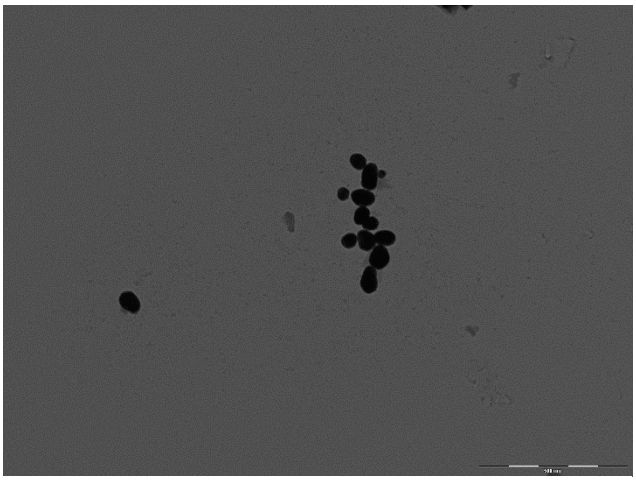

Figure 32: Spherical nanoparticles of 70nm seen by TEM microscopy at 500nm magnification

In excel we reported the sizes of as many nanoparticles as measured using the ImageJ program and averaged them. (Table7) (Table8).

Np1	average	dev.standard	error
diameter	18,8	2,7	0,3
radius	9,4	1,4	0,1

Np2	avarage	dev standard	error
diameter	16,8	2,6	0,5
radius	8,4	1,3	0,2

Np3	average	dev.standard	error
diameter	71,7	9,4	0,9
radius	35,8	4,7	0,5

Table 2: Average of spherical nanoparticles diameters, standard deviation and measurement error.

S1	average	St. deviation	error
diameter	75,2	24,9	4,9
radius	37,6	12,4	2,4

S3	average	St. deviation	error
diameter	70,3	19,6	3,5
radius	35,2	9,8	1,8

S4	average	St. deviation	error
diameter	82,0	31,0	9,8
radius	41,0	16,5	5,2

S5	average	St. deviation	error
diameter	114,1	144,8	40,2
radius	57,0	72,4	20,1

S6	average	St. deviation	error
diameter	129,7	487,8	199,1
radius	64,8	243,8	99,6

Table 3: Average of star-shape nanoparticles diameters, standard deviation and measurement error.

The data reported here were obtained by performing mean and standard deviation while the error by formula:

$$error = dev.standard/\sqrt{N}$$

Where N represents the number of nanoparticles for which the measurement was made. In the case of the stars, DNA-PAINT analysis was then performed with S1, S3, and S4 only. S5 and S6 were neglected both because of the large measured size that was not of interest to us and because of the high variability of the measurement and the low number of nanoparticles that we were able to detect with TEM microscopy [55].

3.3 Functionalization of nanoparticles with oligonucleotides

After synthesizing the nanoparticles, we proceeded with functionalizing them with oligonucleotides. The aim is to coat the surface the entire surface of the nanoparticle with oligonucleotides. For each sample we have two avenues as we can see from the Figure 16. One contains the synthesized nanoparticles while the other contains the nanoparticles with the oligo. As you can see from the picture (Figure 16) the nanoparticles functionalized with oligos have a slightly lighter color. During the centrifugation process, some of the sample may be removed along with the supernatant, reducing the concentration of nanoparticles in the solution. This process can lead to a decrease in color intensity and can thus be a disadvantage when analyzing new samples with UV-Vis or ZP or DLS.

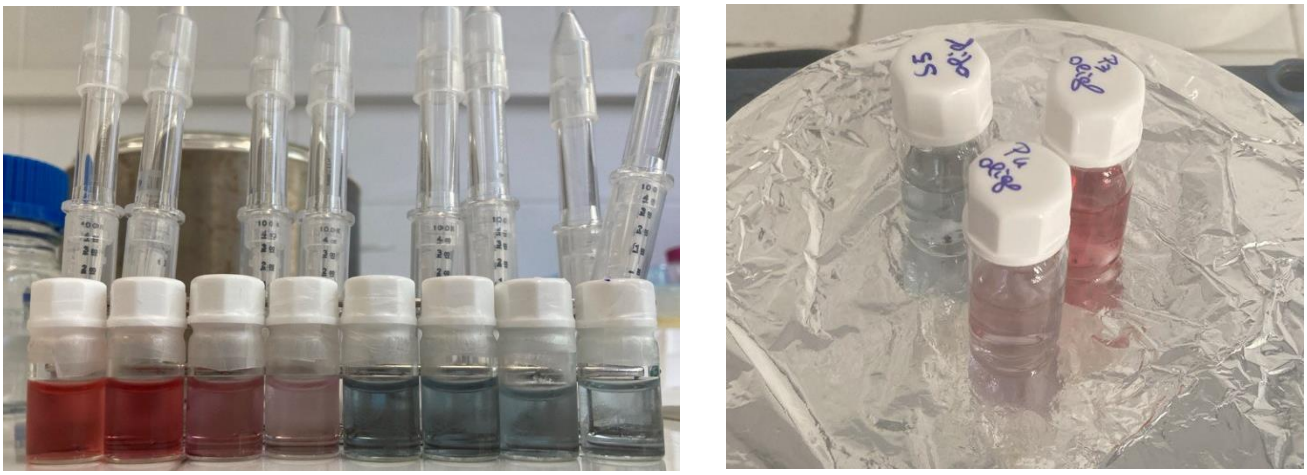

Figure 16: A)the synthesized nanoparticles and the nanoparticles with the oligo. B) Nanoparticles during funcinalization steps on the stirrer.

We performed all the necessary calculations in order to functionalize the nanoparticles properly. As we can see from the data below, we performed more tests for nano stars than for nano spheres and this is because in the case of stars there is less colloidal stability. Star-shaped nanoparticles have a shorter stability lifetime than spheres. In addition, aggregate formation occurs more easily, making the speed of the reaction crucial. We used a 10-fold concentration of oligo; since the nanoparticles are very small, we assumed that more oligo would make the presence or absence of functionalization more obvious. Np1, Np2 and Np3 represent nanoparticles with sizes of 19 nm, 16 nm and 70 nm, respectively.

- In the case of nanosphere (Table2) (Table3)

AuNps G.	epsilon(M^-1*cm^-1)	potenza di 10	Cn (M)	Cn(nM)
Np2	695650381,1	6,96*10^8	1,05552E-09	1,05552
Np1	1004913309	1,00*10^9	5,68334E-10	0,568334
Np3	82210367299	8,22*10^10	1,64189E-11	0,0164189

Table 4: Calculations. Started from the epsilon and then got the concentration Cn, depending on the size of Nps.

Np1=18,87	oligo (ul)	Tcep (ul)
x1	0,2	4
x10	2	40
Np2=16,88	oligo (ul)	Tcep (ul)
x1	0,3	6
x10	3	60
Np3=71	oligo (ul)	Tcep (ul)
x1	0,08	1,67
x10	0,8	16,7

Table 5:Results obtained from previous Cn values and in relation to spherical particle size. In the first column is x1 concentration while in the second is x10(used by us)

- In the case of nano star (Table4) (Table5)

NANO STAR					
star	S1	S3	S4	S5	S6
d (nm)	75	70	82	114	130
ε (M-1cm-1)	95504363063	76055843998	1,2821E+11	3,80347E+11	5,86718E+11
pot di 10	9,50E+10	7,60E+10			
UV_VIS_Abs	0,867172191	0,763328926	1,15348	1,009569	1,1007
Cn(M)	9,13E-12	1,00E-11	8,99679E-12	2,65434E-12	1,87603E-12
Cn(nM)	0,009	0,01	0,0089967	0,00265434	0,00187603

Table 6: Table 2: Calculations done on excel. Started from the epsilon and then got the concentration Cn, depending on the size of Nps.

S1=75nm	oligo (ul)	Tcep (ul)
x1	0,05	1,025
x10	0,5	10,2

S3=70nm	oligo (ul)	Tcep (ul)
x1	0,049	0,98
x10	0,49	9,8

S4=82nm	oligo (ul)	Tcep (ul)
x1	0,06	1,2
x10	0,6	12

S5=114	oligo (ul)	Tcep (ul)
x1	0,034	0,68
x10	0,34	6,8

S6=130	oligo (ul)	Tcep (ul)
x1	0,031	0,63
x10	0,31	6,3

Table 7: Results obtained from previous Cn values and in relation to particle size. In the first column is x1 concentration while in the second is x10(used by us)

3.4 Characterization of nanoparticles

The nanoparticles were analyzed before and after functionalization to verify that they had been functionalized correctly. This applies to the three characterization techniques we will see below.

3.4.1 DLS

In this thesis, DLS was used to verify that conjugation between the nanoparticles and the docking strands had occurred. That is, the size of the NPs without conjugation was measured first as a control and then compared with the size of the NPs conjugated with the docking strands. If the conjugation of NPs with docking strands was performed correctly, a slight increase in the size of conjugated NPs will be observed compared with control NPs. Next, DLS results, representative of all samples in this thesis, will be presented. In particular, the results for the formulation of spherical nanoparticles P1, P2 and P3 will be presented, corresponding to 19, 16, 70 nm in diameter, as determined by TEM. The stars were not analyzed by DLS because, measuring the hydrodynamic diameter, it would not make much sense given their articulated shape. All measurements were made considering water as the solvent since the nanoparticles are suspended in water. The most significant are those for number and intensity that allow me to understand the size of the nanoparticle and how many nanoparticles there are of that size. The data shown were obtained using the Zetasizer software. As you can see the peaks in the graph of the DLS of oligo functionalized nanoparticles are shifted to the right, which means a

larger size. Remember that the dimension measured through DLS is a hydrodynamic radius and not the actual radius we measure with TEM. (Figure 17) (Figure 18) (Figure 19) (Figure 20) [53]

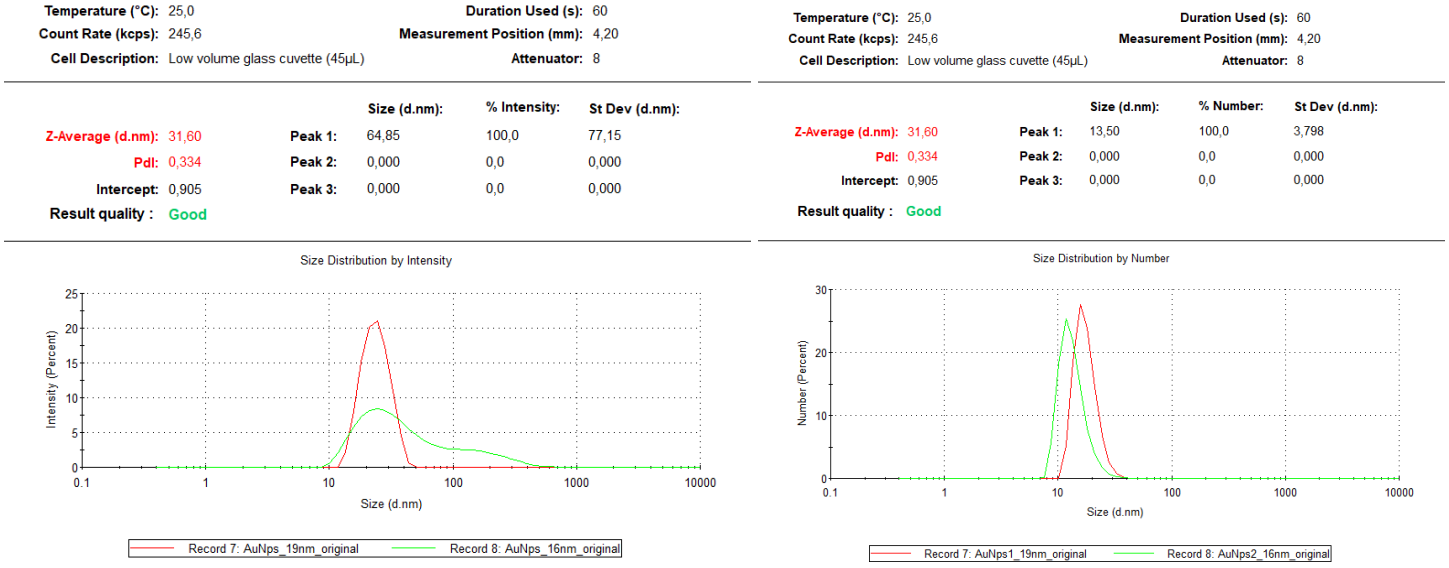

Figure 17: Obtained with the Zetasizer softwer. Is a comparison of 16- and 19-nm nanoparticles as synthesized .On the right are the data obtained by intensity while on the left by number.

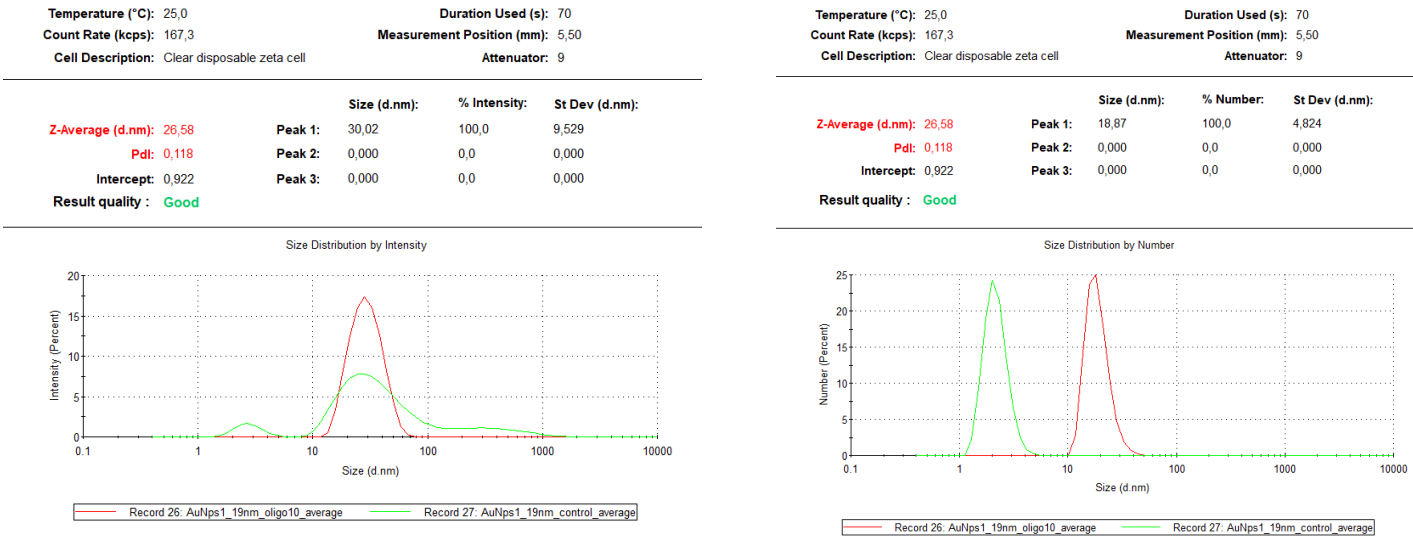

Figure 18: obtained with the Zetasizer software. The peaks in the graph of oligo-functionalized nanoparticles (19 nm) are shifted to the right, which means having a larger size (red peak). On the right are the data obtained by intensity while on the left by number.

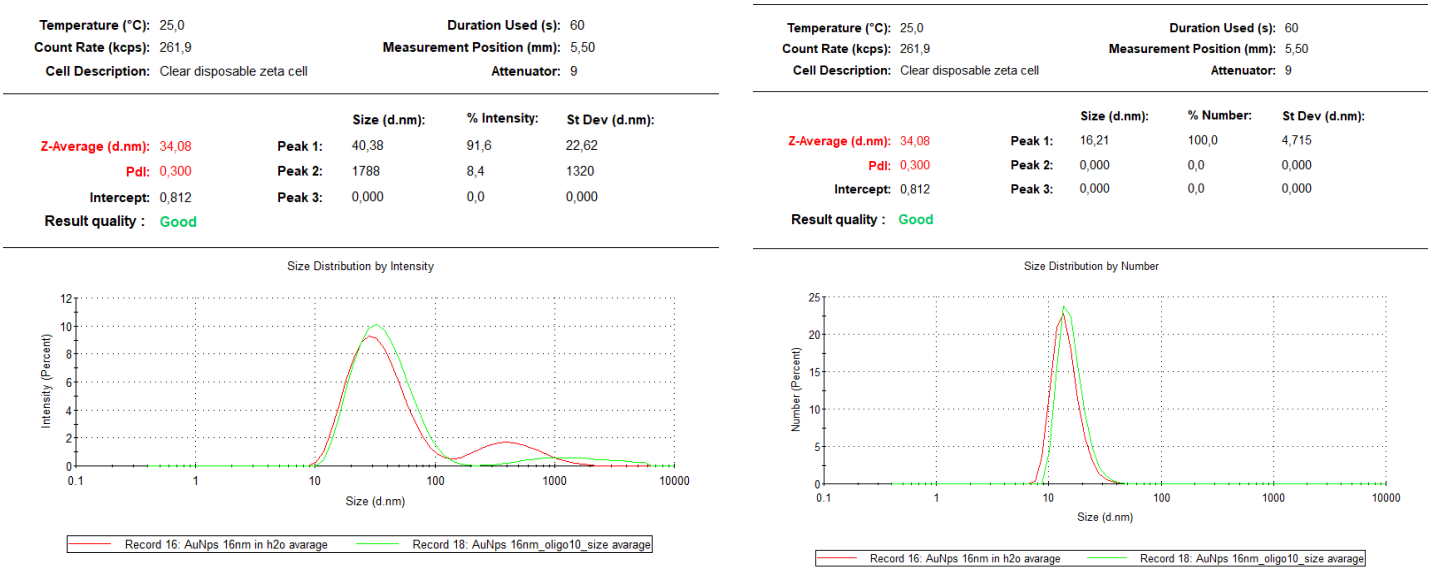

Figure 19: Obtained with the Zetasizer software. The peaks in the graph of oligo-functionalized nanoparticles (16 nm) are shifted to the right, which means having a larger size (red peak). On the right are the data obtained by intensity while on the left by number.

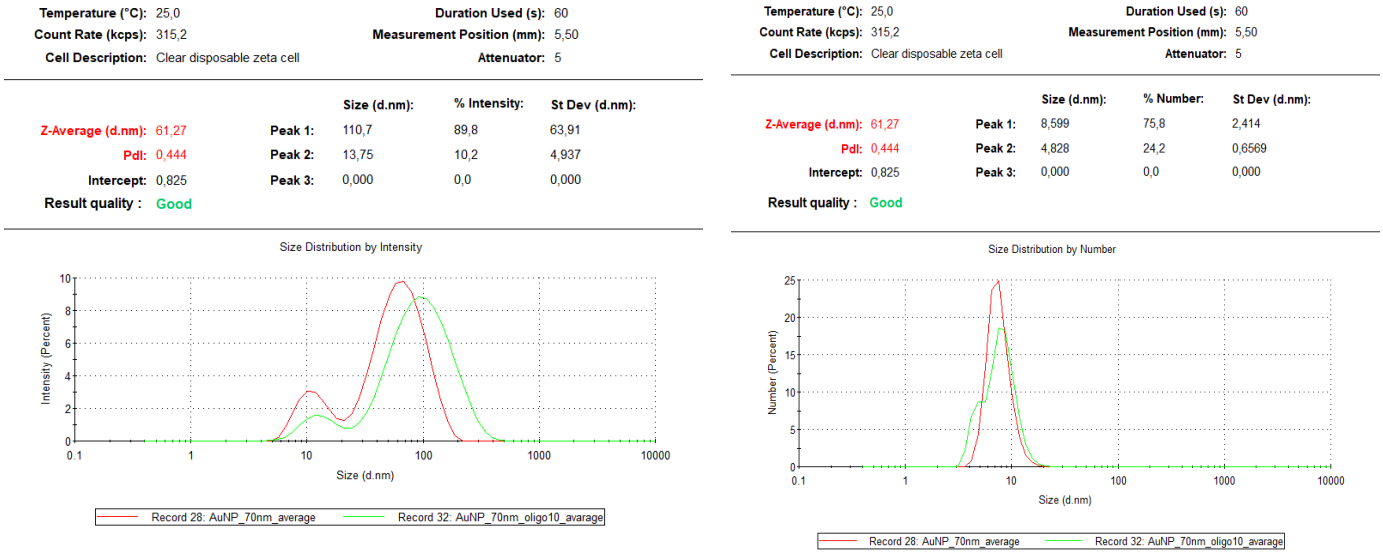

Figure 20: Obtained with the Zetasizer software. The peaks in the graph of oligo-functionalized nanoparticles (70 nm) are shifted to the right, which means having a larger size (red peak). On the right are the data obtained by intensity while on the left by number.

The DLS analysis was done only for nanospheres since using the DLS to measure the hydrodynamic radius of nanostars does not make much sense in consideration of the fact that the software analyzing the data assumes spherical morphology.

3.4.2 Zeta potential

In this thesis, ZP was used to verify that conjugation between gold nanoparticles and DNA strands. That is, the surface charge of NPs without conjugation was first measured as a control, and then the surface charge of those conjugated with docking strands was measured. If conjugation is performed correctly, a significant increase in negative charge in the surface charge of the conjugated NPs compared with the control NPs should be observed, because the docking strands provide more negative charge on the surface of the NPs. Next, ZP results, representative of all samples in this thesis, will be presented. In particular, results for spherical nanoparticles P1, P2 and P3 and star particles S1, S3, S4 and S5 will be presented corresponding to 19 nm, 16 nm, 70 nm and 75 nm, 70 nm, 82 nm,114 nm in diameter respectively. All measurements were made considering water as the solvent since the nanoparticles are suspended in water. The data shown were obtained using Zetasizer software (Figure 21-27) [35]

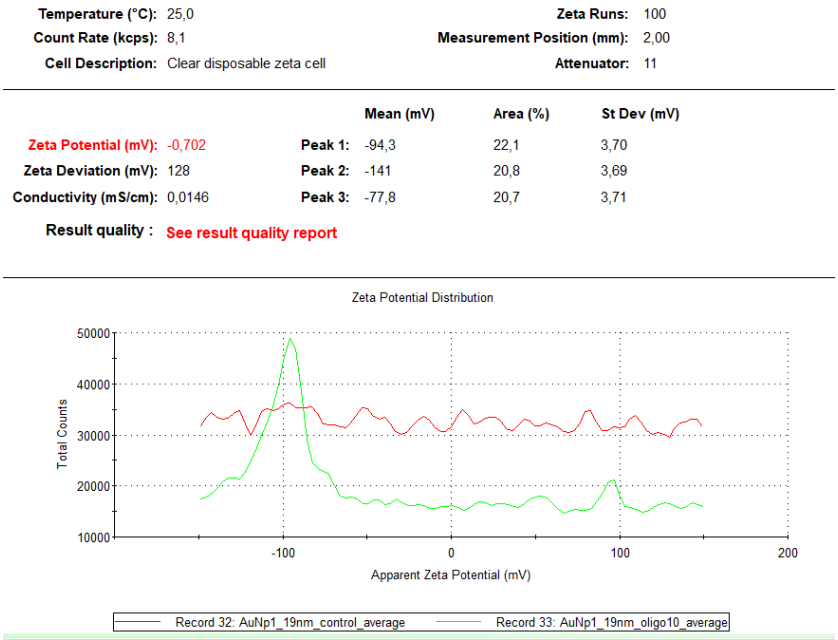

Figure 21:Representation of the surface charge of control AuNPs (without conjugation) and with conjugation. ZP distribution. Conjugates are more electronegative so the peak is at negative values.(Spherical Nps 19nm)

For the 19 nm Nps an unclear control peak was obtained, probably due to the excessive decrease in concentration of the nanoparticles after centrifuging which also led to a color change towards lighter shades.

Temperature (°C):	25,0		**Zeta Runs:**	71
Count Rate (kcps):	267,9		**Measurement Position (mm):**	2,00
Cell Description:	Clear disposable zeta cell		**Attenuator:**	11

		Mean (mV)	**Area (%)**	**St Dev (mV)**
Zeta Potential (mV):	-5,60	**Peak 1:**	-88,0	56,7	21,7
Zeta Deviation (mV):	126	**Peak 2:**	32,8	12,4	8,58
Conductivity (mS/cm):	0,0388	**Peak 3:**	-28,4	11,7	7,54

Result quality : See result quality report

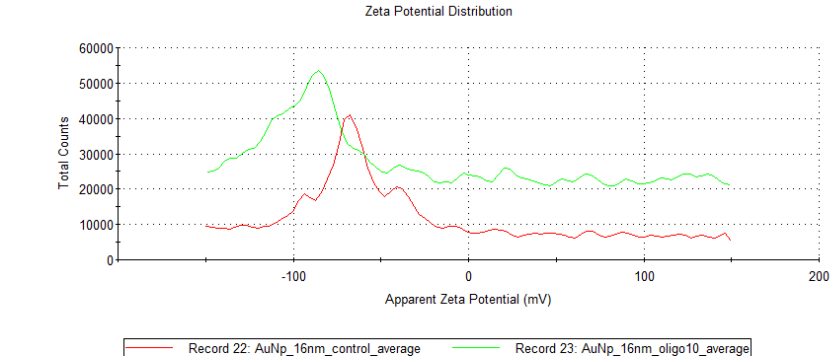

Figure 22: Representation of the surface charge of control spherical AuNPs (16 nm, without conjugation) and with conjugation. ZP distribution. Conjugates are more negative so the peak is at negative values.

Temperature (°C):	25,0		**Zeta Runs:**	33
Count Rate (kcps):	243,6		**Measurement Position (mm):**	2,00
Cell Description:	Clear disposable zeta cell		**Attenuator:**	9

		Mean (mV)	**Area (%)**	**St Dev (mV)**
Zeta Potential (mV):	-13,2	**Peak 1:**	-135	38,0	8,41
Zeta Deviation (mV):	111	**Peak 2:**	-90,4	30,0	9,24
Conductivity (mS/cm):	0,374	**Peak 3:**	-46,1	13,6	3,63

Result quality : See result quality report

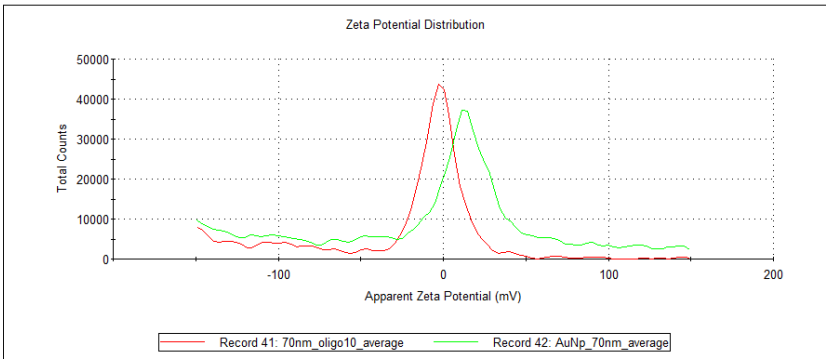

Figure 23: Representation of the surface charge of control spherical AuNPs (70 nm, without conjugation) and with conjugation. ZP distribution. Conjugates are more negative so the peak is at negative values.

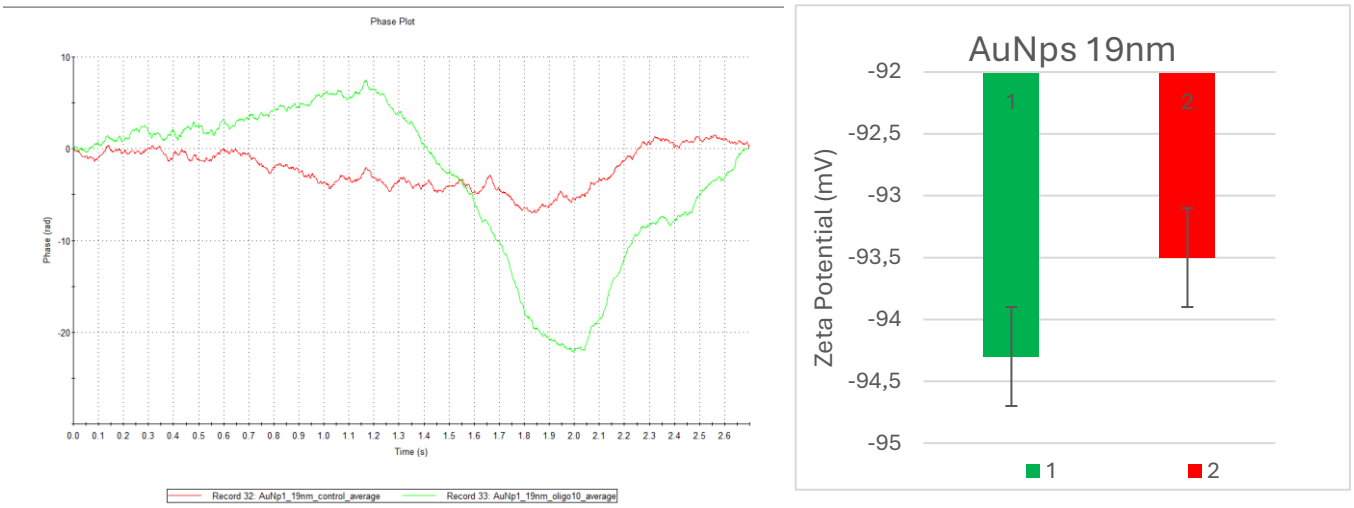

Figure 24: Representation of the surface charge of control spherical AuNPs (without conjugation) and with conjugation. Conjugates are more negative. On the right a representation obtained from Zetasizer program and on the left a histogram representation.

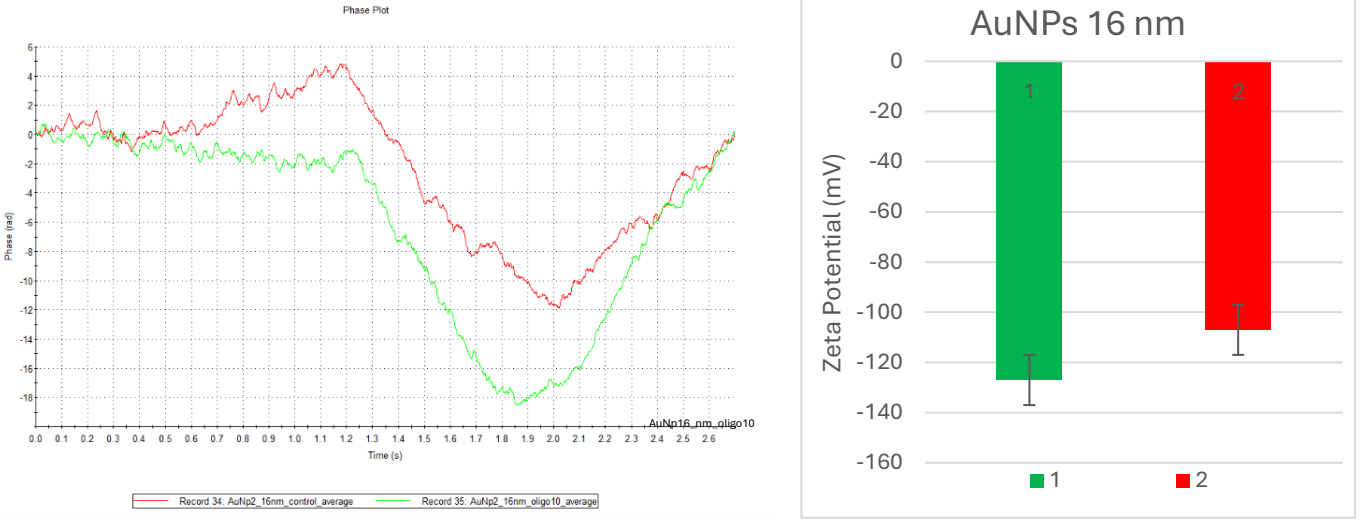

Figure 25: Representation of the surface charge of control AuNPs (16 nm, without conjugation) and with conjugation. Conjugates are more negative. On the right a representation obtained from Zetasizer program and on the left a histogram representation.

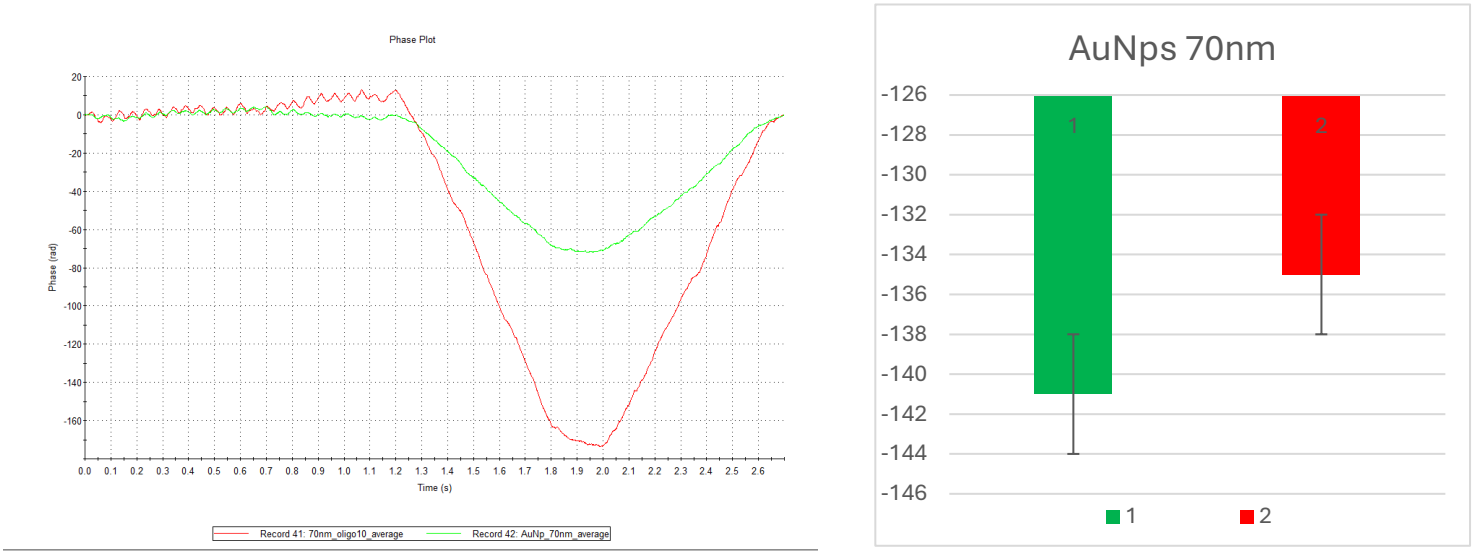

Figure 26: Representation of the surface charge of control AuNPs (70 nm, without conjugation) and with conjugation. Conjugates are more negative. On the right a representation obtained from Zetasizer program and on the left a histogram representation.

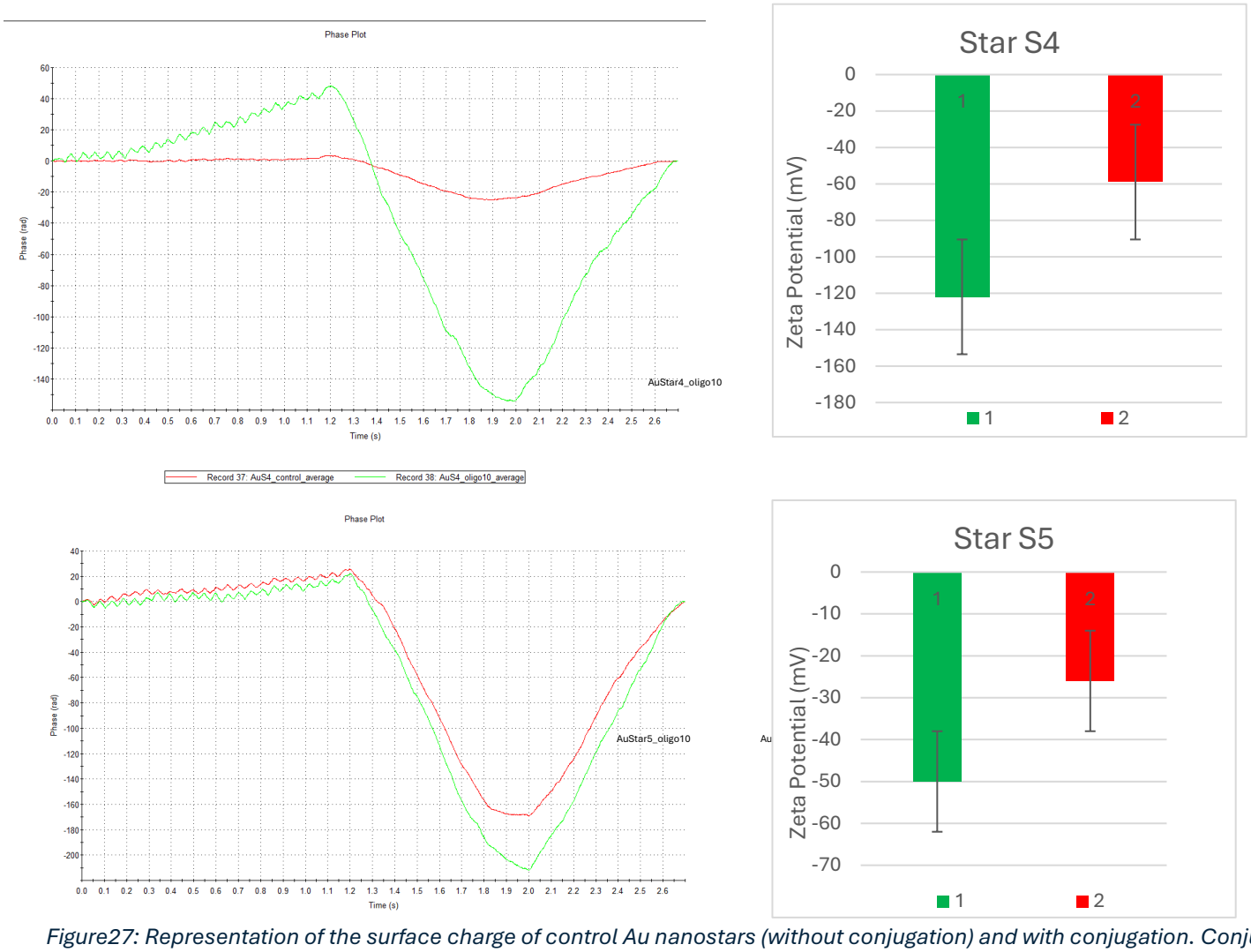

Figure27: Representation of the surface charge of control Au nanostars (without conjugation) and with conjugation. Conjugates are more negative. On the right a representation obtained from Zetasizer program and on the left a histogram representation.

37	Zeta	AuS4_control_average	lunedì 26 agosto 2024 20:46:45	25,0	-3,48	-0,2726	0,00434
38	Zeta	AuS4_oligo10_average	lunedì 26 agosto 2024 20:47:01	25,0	-27,8	-2,176	0,0152
41	Zeta	AuS5_control_average	lunedì 26 agosto 2024 20:48:25	25,0	-18,0	-1,413	0,00227
42	Zeta	AuS5_oligo10_average	lunedì 26 agosto 2024 20:50:40	25,0	-28,9	-2,267	0,00570

Table 8: penultimate column is the one we are interested in considering because it shows the data of higher negativity in the cases of oligo-conjugated particles.

As expected nanoparticles with oligonucleotides on the surface are more negatively charged (Table 6). This can be seen from both the zeta potential distribution graph and the phase plot. Oligonucleotides are short sequences of nucleic acids (DNA or RNA) made up of repeating units of nucleotides. Each nucleotide is made up of a nitrogenous base, a five-carbon sugar (ribose or deoxyribose) and a phosphate group. The phosphate group (PO_4^{3-}) is negatively charged, giving an overall negative charge to the oligonucleotide. When oligonucleotides bind to the surface of the nanoparticles, these phosphate groups bring their negative charge with them, thus increasing the net negative charge on the surface of the nanoparticles. The nanoparticles, before functionalization, have a weakly negative charge, due to the synthesis with citrate. After functionalization with oligonucleotides, the negative charge of the phosphate groups of the oligonucleotides adds to the surface charge of the nanoparticles, making them significantly more negative.

3.4.3 UV-Vis

From the ultraviolet-visible we can obtain the absorption spectrum. Depending on the size of the nanoparticle we will get a different spectrum with an absorbance peak at different wavelengths. The wide-path cuvette is filled with 1 ml of colloidal solution (Figure 33) after, however, performing a baseline check with milliQ water.

Figure 33 : The wide-path cuvette with 1 ml of colloidal solution of spherical Nps for UV-Vis analysis.

Metallic nanoparticles, such as gold nanoparticles, exhibit a phenomenon known as localized surface plasmon resonance (LSPR), which manifests as a characteristic absorption peak in the UV-Vis spectrum due to the collective oscillation of conduction electrons on the nanoparticle surface in response to incident light. The position and intensity of the LSPR peak are strongly dependent on the size of the nanoparticles. As the nanoparticle size increases, the LSPR peak shifts to longer wavelengths (red shift). For example, elongated or aggregated nanoparticles may show more than one peak, corresponding to different directions of electron oscillation; this is not what we want to achieve.

A broader peak may suggest a broader size distribution or a nonspherical shape of the nanoparticles, and finally by comparing different UV-Vis spectra, it is possible to determine which sample has larger or differently shaped nanoparticles. By correlating the position, intensity and shape of the absorption peak with the size of the nanoparticles, you can get a clear picture of their characteristics. The first two spectra represent the absorbance spectrum of the NP1 and NP2 nanoparticles, which are about 16 nm and 19 nm in diameter, respectively. As we can see, the absorbance peak of the oligo-functionalized nanoparticles is shifted toward longer wavelengths by a few nanometers, meaning that even if only slightly, the nanoparticle has increased its diameter as we expected (Figure 34) In the third graph, on the other hand, the peak is a little wider due perhaps to the nanoparticles being a little less stable and precise because of size. Here we compared the nanoparticles as we synthesized them both before and after performing the centrifuge procedure. In the case after centrifugation we see how the peak is almost not visible due to the very low absorbance . That is why we decided to also include the nanoparticles without centrifugation, so that the difference in the wavelength of the peak would be more obvious. In both cases, however, it can be seen that the nanoparticles with oligo show a peak at a longer wavelength, which means they will be larger in diameter as expected [56]. (Figure 34)

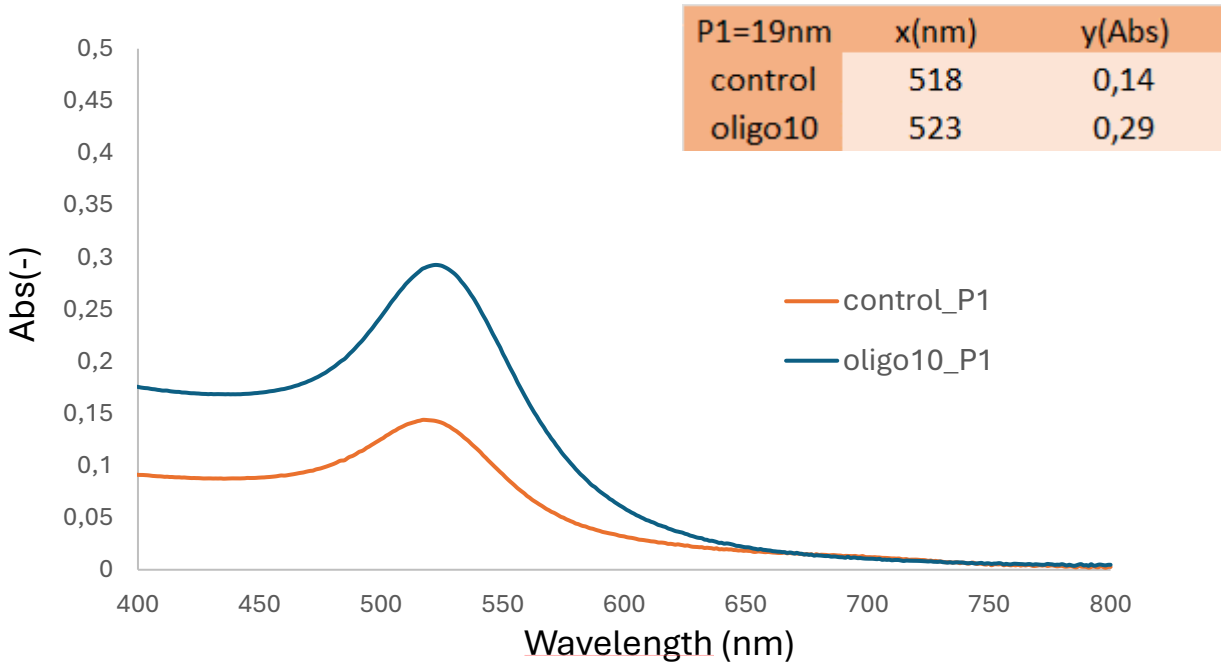

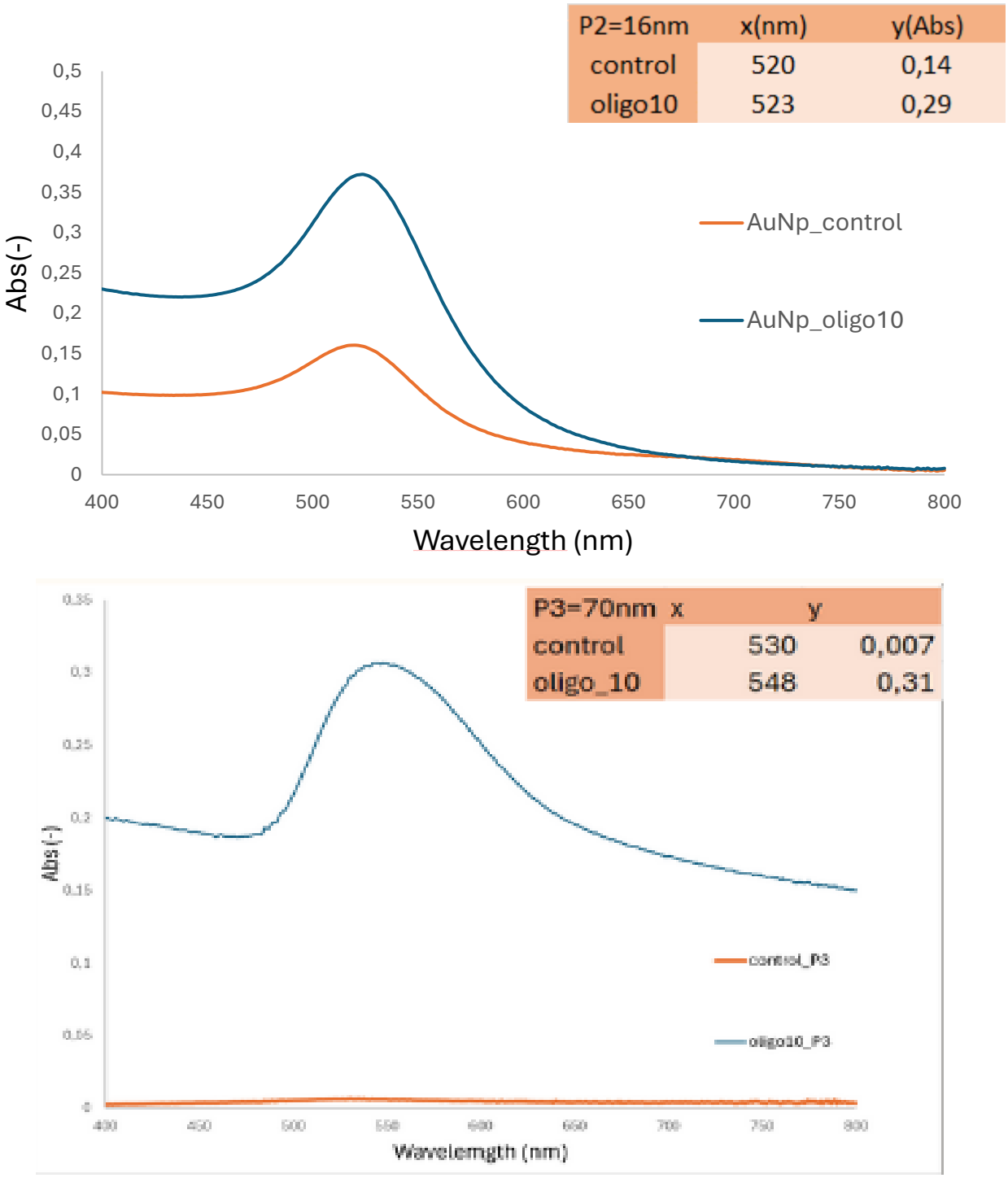

Figure34 : Absorption spectrum of AuNPs of different sizes in which the shift of the absorbance peak changes when the particles are conjugated (at higher wavelengths).

Now we can consider the star; given the results obtained from the TEM images we have just analyzed, it was decided to functionalize the nanostructures S1, S3, S4, and S5. With the latter, as we shall see, it was then decided not to continue with subsequent analyses. (Figure 35)

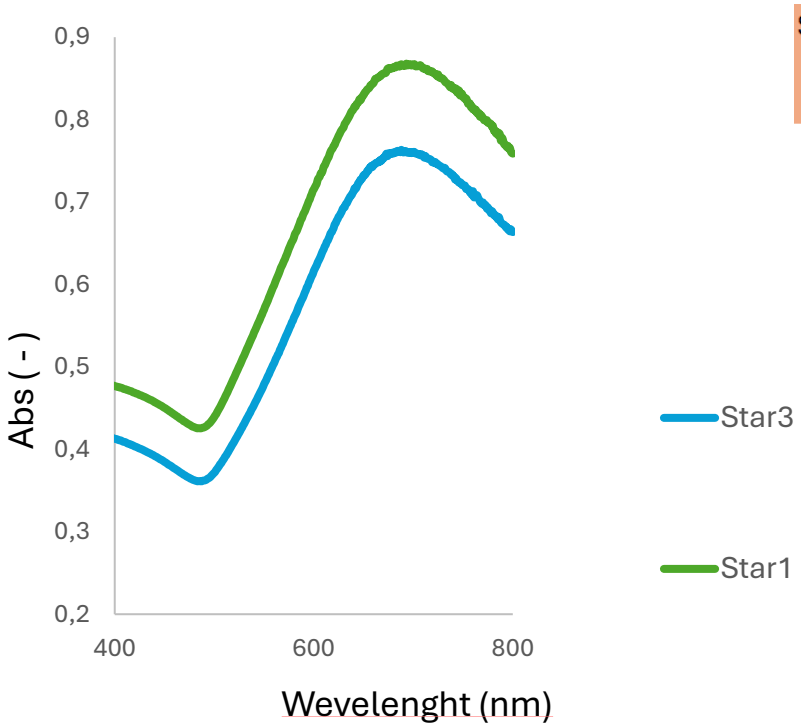

Stars synthesized	x (nm)	y (Abs)
S1	700	0,740558
S3	688	0,763328

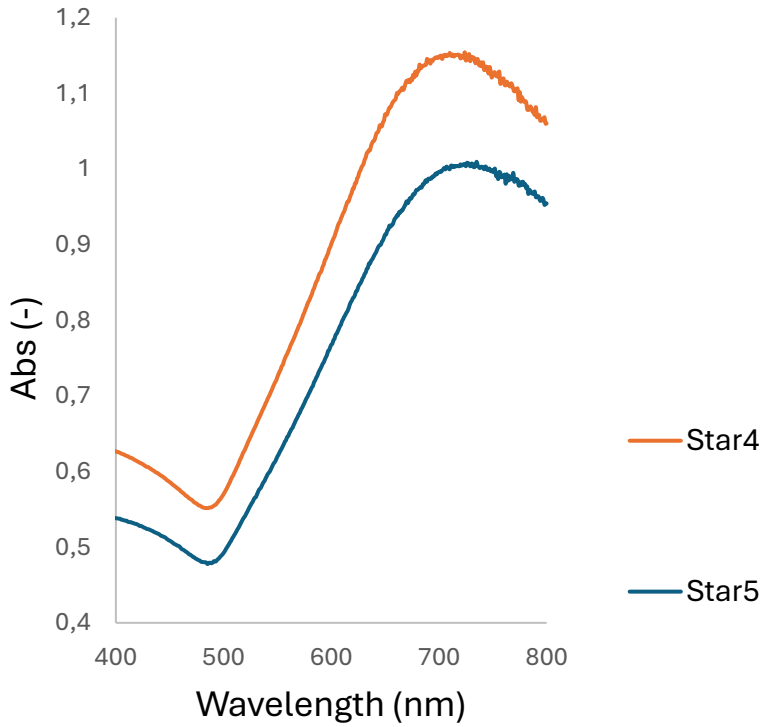

Star synthesized	x(nm)	y(Abs)
S4	710	1,15
S5	735	1

Figure35 : Absorption spectrum of star-shape AuNPs of different stars. We tried different times.

The graphs just shown represent the newly synthesized stars and their respective relative absorbances at the corresponding wavelengths. For each graph we have also represented a table showing the peak

data. Now, however, let us see what happens to such nanoparticles after functionalization with oligonucleotide and report a comparison between the two situations. (Figure36).

S1=75nm	x(nm)	y(Abs)
control	682	0,08
oligo10	663	0,004

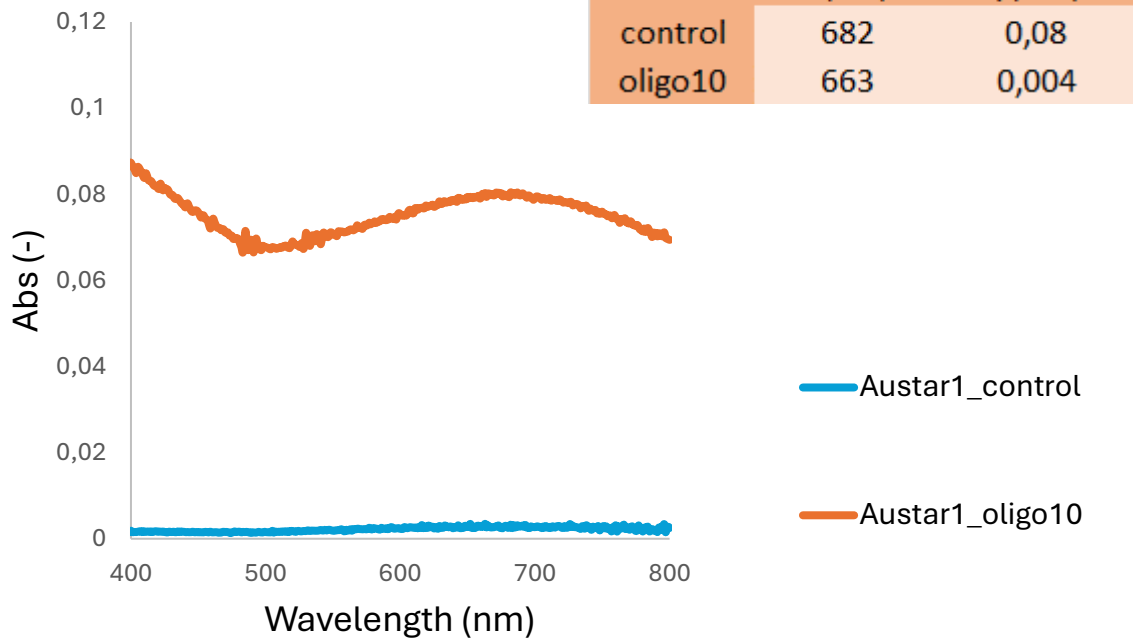

S3=70nm	x(nm)	y(Abs)
control	673	0,005
oligo10	701	0,19

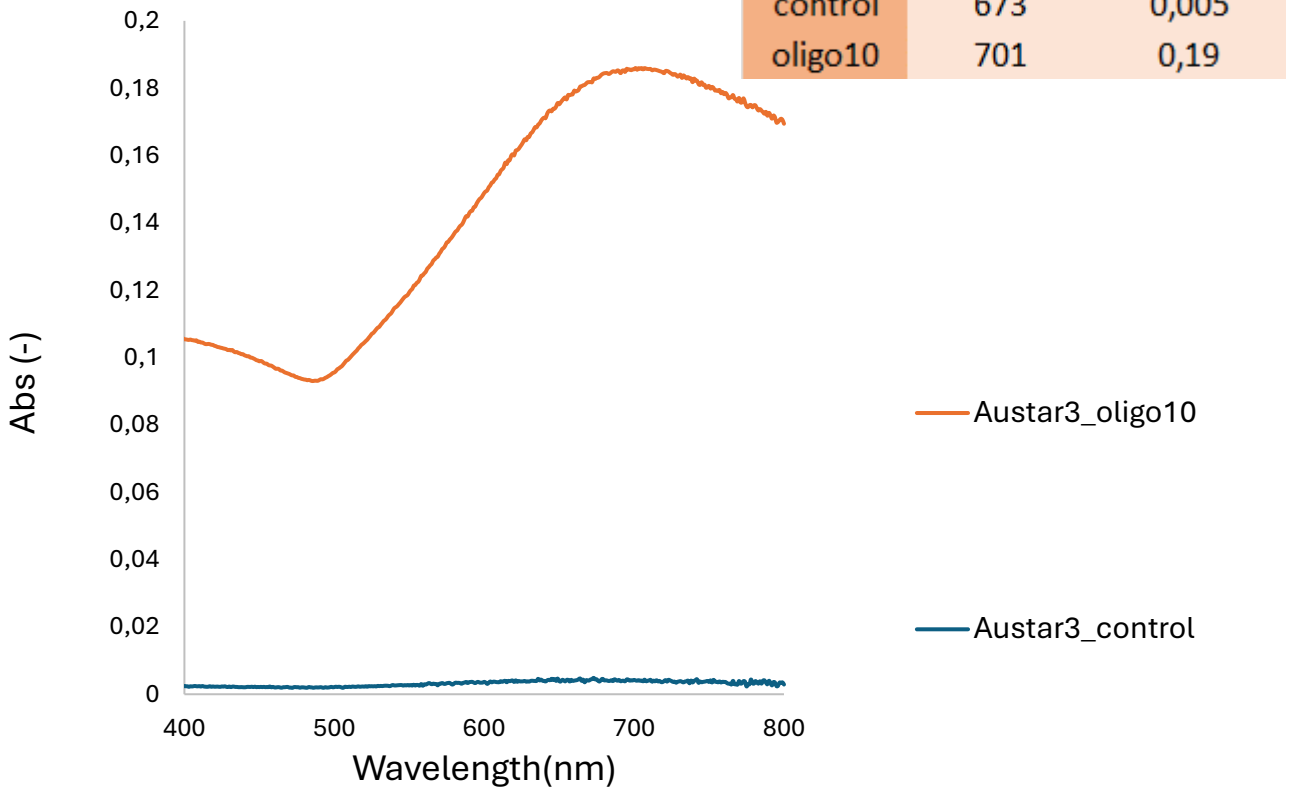

Figure36: Absorption spectrum of star-shape AuNPs in which the shift of the absorbance peak changes when the particles are conjugated with oligo (at higher wavelengths).

Stars in general, compared to spheres, have an absorption peak more shifted toward the red so toward longer wavelengths. As can be seen from the results obtained, after performing the centrifugation procedure with and without oligo the value of maximum peak absorbance is lowered. However, in the case of stars 3 and 4 the same case noted in the spheres occurred, namely that after functionalization the wavelength of the peak increases and thus also the size, as expected. This does not occur in the case of stars 4 and 5, which were therefore excluded and DNA-PAINT analysis was not carried out thereafter. In fact, the opposite occurs in these two cases, and this is anomalous. We thought that functionalization was not done correctly. Because of their articulated shape, it is more difficult to estimate their exact size, and therefore consequently all calculations are more approximate. In addition, since they are not spherical, one cannot actually know where the oligonucleotide will have positioned itself with respect to the irregular surface of the star [57], [58].

3.5 Super resolution microscopy

3.5.1 Functionalization of slides

As described earlier in the experimental section, 4 different treatments of the coverslip were tested to achieve longer adhesion of AuNPs. Visualization by TIRF microscopy showed that the first three treatments did not work as expected, since only a few AuNPs adhered to the coverslip, and this was visible for both the newly synthesized nanoparticles and the docking strand-functionalized particles. Finally, A4 treatment with APTES allowed the functionalization of the coverslip through ether bonds, letting the positively charged amine groups at the ends bind to the AuNPs through the negative charge of citrate or phosphate in the case of oligonucleotides. In general, it was noted that the larger nanoparticles (70 nm or stars in our case) had greater adhesion than the smaller particles, which had a much harder time sticking in all the treatments tried. The protocols that seemed to be most promising were A1 and A4 (Figure 37). For this reason, we will report below only a few of the most significant examples from the tests performed, just to provide an idea of the difference that was noticed between one protocol and another.

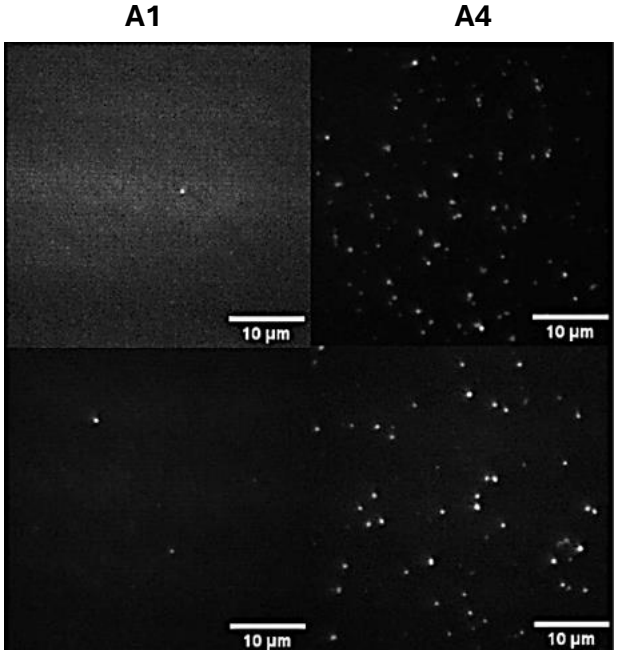

Figure 37: Images of the NIS-Elements of the N-STORM for the protocols A1, A4 of attachment of AuNPs of 70

As an example, 70 nm nanoparticles functionalized with the DNA strand will be discussed. The first column of Figure 37 shows an example of protocol A1 application while the second column shows an example of protocol A4 application. As can be seen, in the second case there is a higher amount of nanoparticles attached to the cover slip demonstrating that the A4 protocol is the most effective of all. Another important difference we can see is how using the same A4 attachment protocol smaller nanoparticles are much more difficult to visualize than larger ones, whether they are spherical or star-shaped (Figure38 A-D). We report below an example that highlights this.

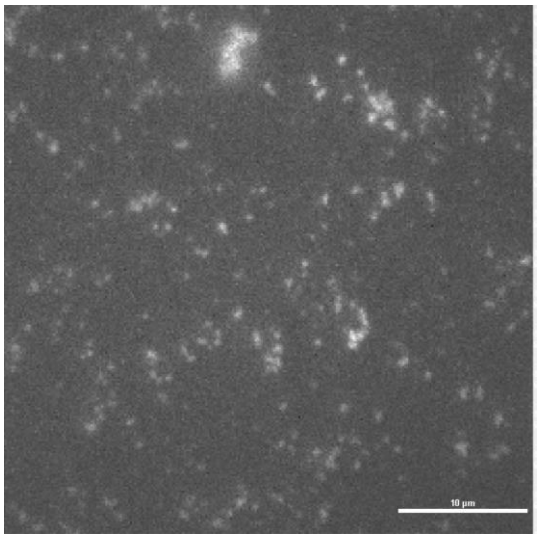

Figure 38A: Images of the NIS-Elements of the signal of 19 nm.

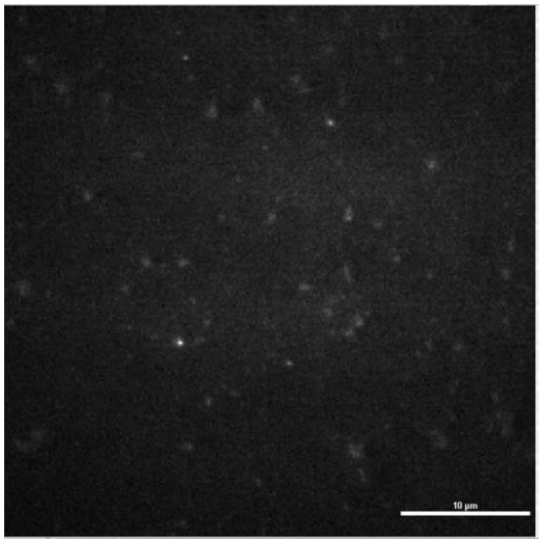

Figure 38B:Images of the NIS-Elements of the signal of 16nm.

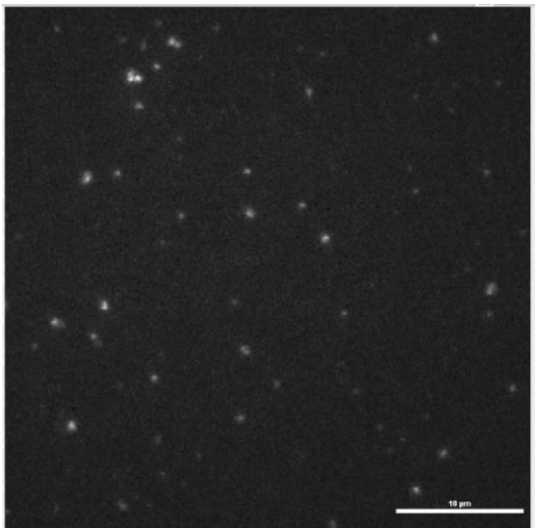

Figure 38C: Images of the NIS-Elements of the signal of 70nm.

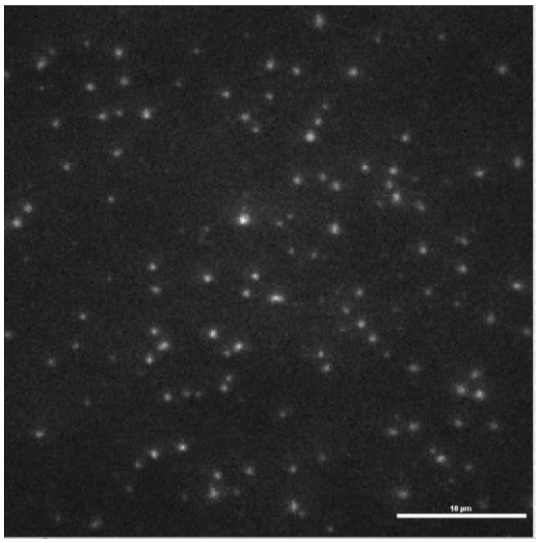

Figure 38D: Images of the NIS-Elements of the signal of nano star (>70nm).

After many attempts at adhesion of the nanoparticles with the different protocols and after having identified the A4 protocol as the best for the prolonged attachment of the nanoparticles on the coverslip, we continued by analyzing the various sizes and shapes as we show in the figures just reported. It was noted that for the spherical nanoparticles, the smaller ones had much difficulty in attaching compared to the larger ones. For the stars, being all large, they did not show any difficulty in attaching to the glass.

3.5.2 TIRF images at different wavelengths

The reflection signal, generated by the NPs present on the surface of the slide or membrane, allows the exact position of the nanoparticles to be mapped. Because TIRF microscopy illuminates only a small region near the surface, it is particularly effective at revealing structures that lie very close to the interface, such as nanoparticles. The position of the reflection signal therefore provides a direct indication of where the nanoparticles are located in the evanescent field. Combining TIRF with DNA-PAINT offers a highly precise approach to visualize the interaction between nanoparticles and functionalized DNA molecules. The TIRF reflection signal provides direct visual guidance, limiting the interrogation to only the regions immediately close to the NPs, while DNA-PAINT allows for super-resolution imaging, improving the ability to observe the molecular organization around the nanoparticles. For each sample, 4 images were acquired for each wavelength corresponding to the three lasers of the microscope, 488 nm, 561 nm and 647 nm. What we noticed is that at the wavelength of 488 nm all the samples give unclear images and the nanoparticles turn out to have very low brightness. Samples related to spherical nanoparticles show higher brightness at wavelengths of 561 nm while stars on the other hand show higher brightness at wavelengths of 647 nm. The larger the size of the particle, regardless of its shape, the higher the brightness will be at longer wavelengths. However, this is not an entirely good thing since the imager strand we purchased shines at wavelengths of 647 nm. Ideally, we would like to have nanoparticles with higher brightness at 561 nm so that we can notice the difference when we add the imager to our sample and then perform DNA PAINT. We show below a series of images of our samples using the three different lasers, so we will notice the different brightness at different wavelengths.(Figure39)

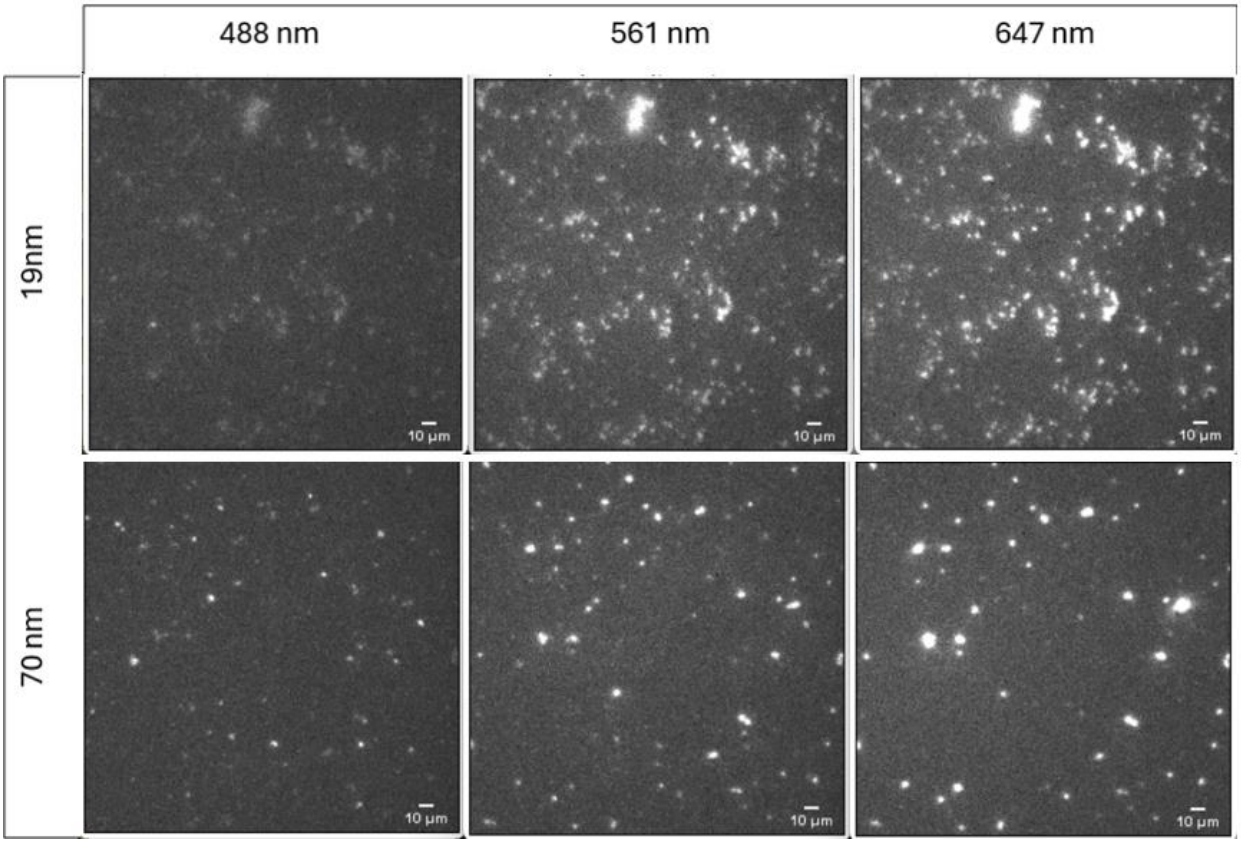

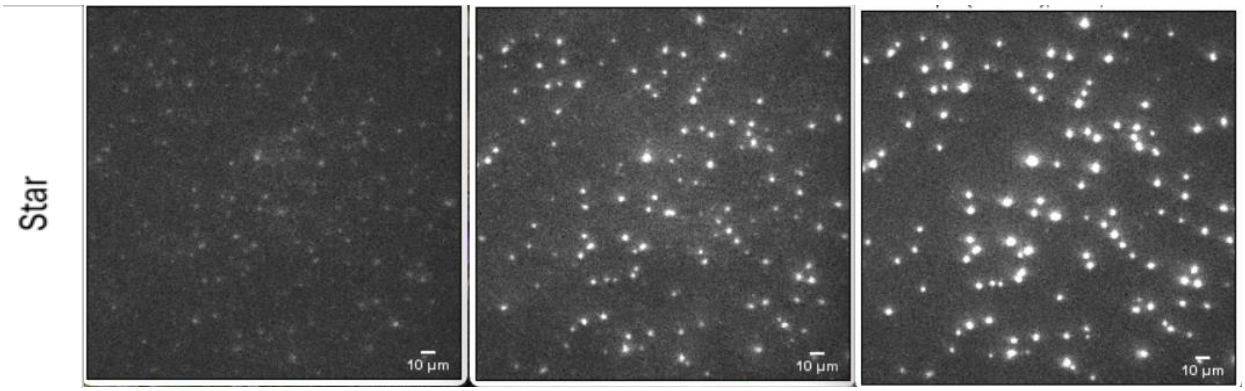

Figure 39: Images of the NIS-Elements of the signal of NPs 19 and 70 nm (spherical) and Star-Shape for different lasers at different nm.

Then we analyzed using the ImageJ program all the intensities of the different nanoparticles at different wavelengths. We averaged and visualized where they were brightest. We report that analysis below (Figure40):

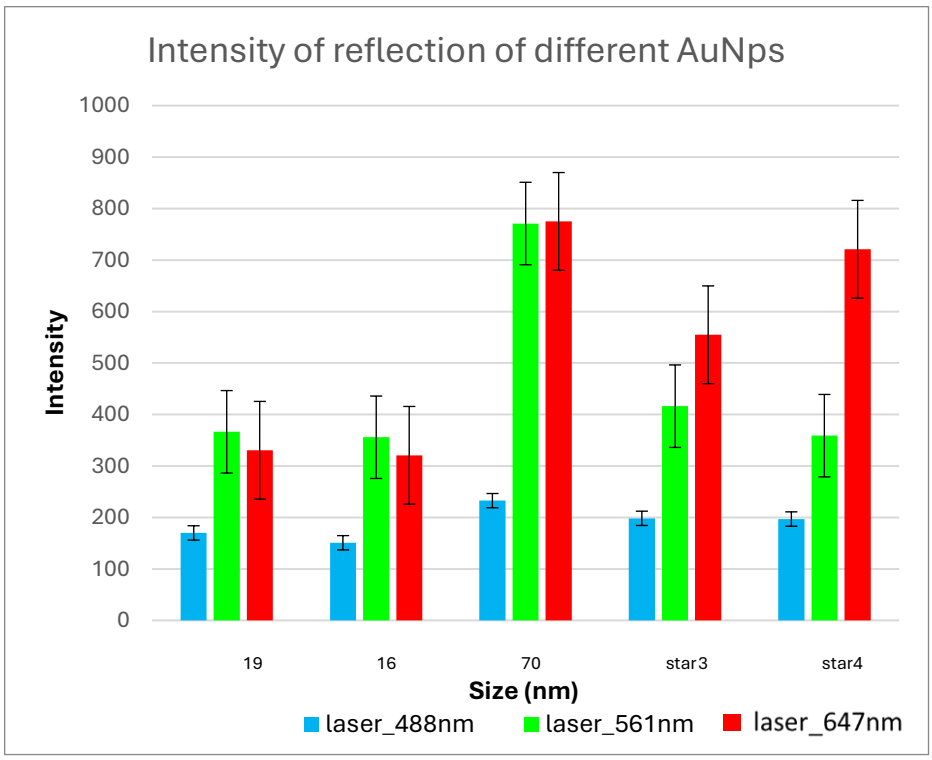

Figure 40: Plot for the mean intensity of reflection of AuNPs at different wavelength (488, 561 and 674 nm). Instagram representation.

Two lasers are used during image acquisition, one channel at 647 nm and one at 561 nm. In the case of stars, because of their larger size, the strongest intensity is that related to the 647 laser. In the case of spherical NPs, the strongest intensity is in the case of laser 561 as we desired since we will later add the imager shining at 647 nm.

Ultimately for this reason we use the 561 channel nm for all nanoparticles. The Atto647N-Imager strand signal was collected using the 647 nm (160 mW) laser with 60% power and the AuNP reflection signal using the 561 nm laser (80 mW) with 10% power.

3.6 DNA-PAINT microscopy

The DNA-PAINT microscope allows images of the position of nanoparticles (green laser, channel 561) and the constant position of the imager strands with ATTO-647N i.e., the imager (red channel, channel 647) in order to visualize their hybridization and detachment with the NPs docking strands. The time required for the acquisition of each image was ~25 min. To perform image analysis of the images of the images, drift correction was first performed. Next, a density filter was applied to clean background of the images. In addition, once the data and image acquisition were finished, if the NIS-Elements module could not correct the mechanical drift, the acquired data became useless. In this thesis, the NPs were all conjugated to the P1 docking strands and then used two different imagers I1 (complementary) and I2 (non-complementary). These were in the first case what one expects a significant amount of signal around the NPs. In contrast, for the control samples, with the I2 imagers strands, generating no or minimal signal around the NPs. As we will see this difference is much more visible in nanoparticles of larger size but at the same time in nanoparticles that have a more regular shape as in the case of spherical ones. We show below some of the images STORM obtained after DNA-PAINT analysis with NIS-Elements software (Figure 41)

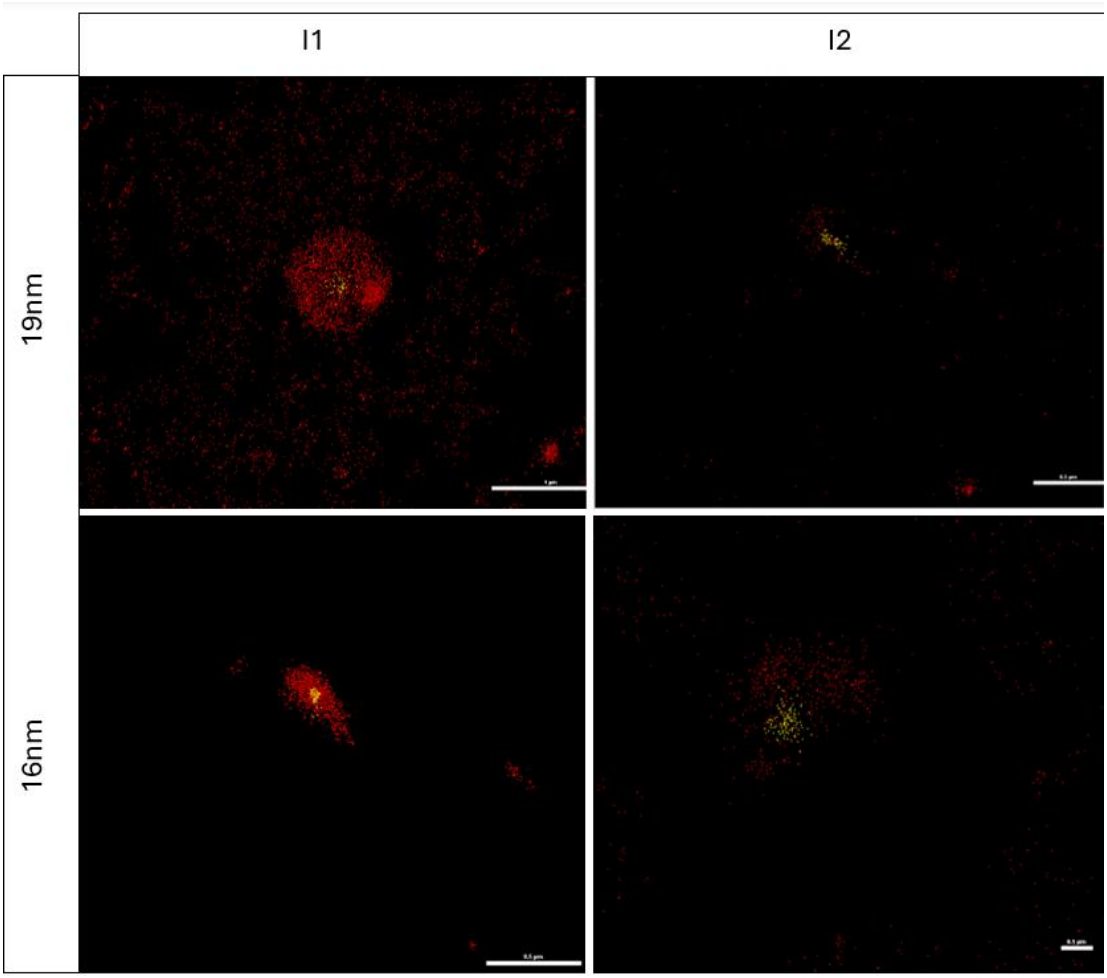

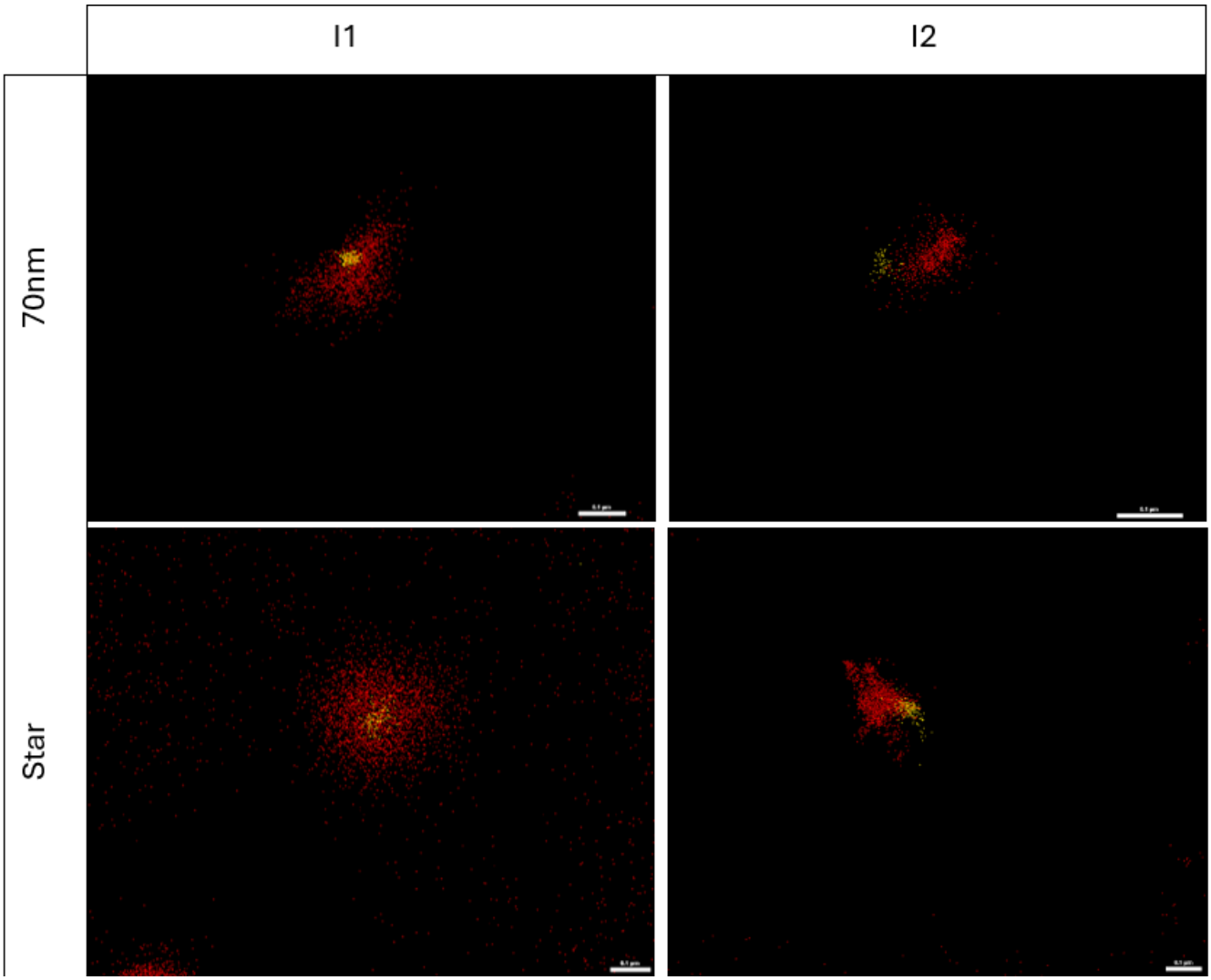

Figure41: Zoom images of a DNA-PAINT analysis of different spherical and star Nps. The yellow part is the nanoparticle reflection and the red one is the imager. I1 is related at complementary imager , I2 is related at no-complementary imager.

As we see in the figures, for spherical nanoparticles the difference between the complementary I1 and the noncomplementary I2 imager is quite clear. The I1 imager positions itself around the nanoparticle providing a strong signal while the noncomplementary imager provides little or no signal, in fact it does not surround the nanoparticle. In contrast, in the case of stars , probably because of their irregular shape, it is not so clear. The I2 imager in fact, in this case gives us equally results. In the last image we see an example of a nanoparticle without the drift correction due to the downward motion of the nanoparticle during the 25-minute analysis.

3.6.1 Drift correction

In the next figure, in the red circle, we see an example of a nanoparticle without the drift correction due to the downward motion of the nanoparticle during the 25-minute analysis (Figure42A-B).

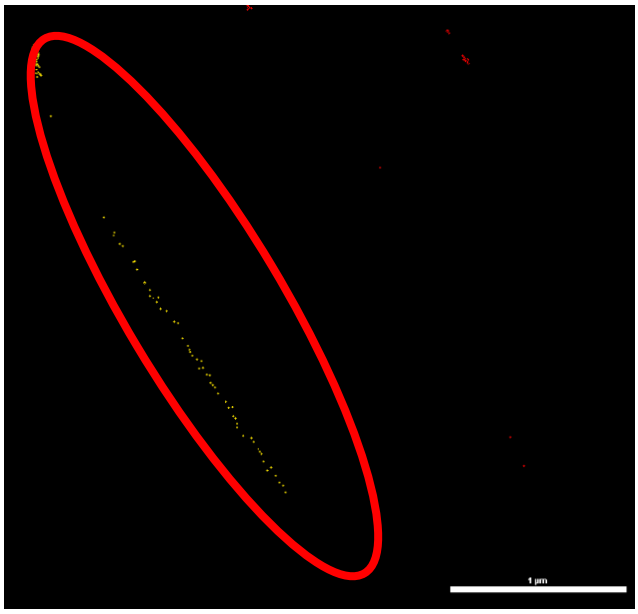

Figure42A: example of a drift of a gold spherical nanoparticles before of correction

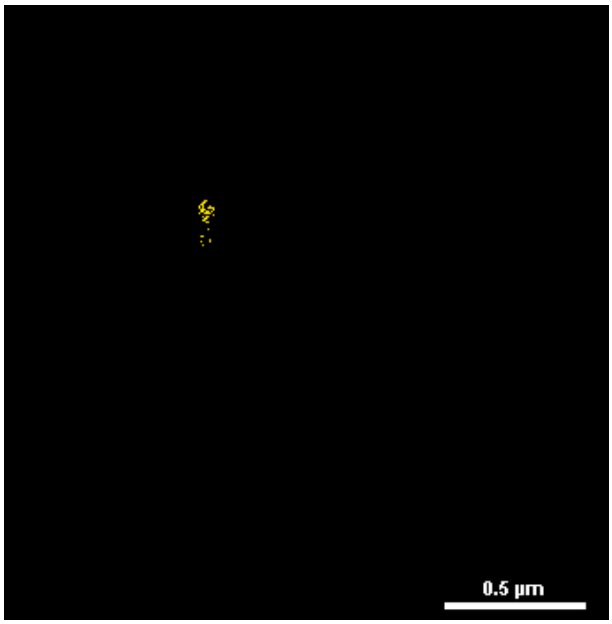

Figure42B: example of a drift correction of a gold spherical nanoparticles.

3.7 Data analysis

We used a previously written Matlab code for data analysis. With the first script (ReadCoords2.m), the cluster position of the 561nm trust channel and thus the center of each individual NP is identified. In the second script (Cluster2.m), the clustering algorithm, several parameters are selected, such as the maximum NP size and the minimum positions for each individual NP, among others. The goal of this analysis was to obtain the exact number of imager strands locations for each individual NP. Therefore, the expected results are to obtain the maximum number of imager strands locations on the surface of NPs conjugated with docking strands complementary to the imager strands used. On the other hand, for the control samples, i.e. with the non-complementary I2 imager, were to obtain zero or minimal imager strands locations on the surface of the conjugated NPs. Therefore, finally through MatLab analysis with DNA-PAINT data, a histogram with imager strands positions for the NPs and their normalized frequency will be obtained.

3.7.1 Matlab results

Here we report examples of MatLab analysis. The results were obtained using a previously created Matlab code. The graphs we report below are for the 16 nm spherical nanoparticle sample with I1, the imager complementary to the DNA strands on the nanoparticle surface. In the first two figures we can see a magenta ellipse indicating a valid particle, a cyan ellipse for an invalid particle, and a yellow ellipse showing a non isolated particle. Red dots indicate the 647 nm-channel (imager) and the blue dots are the fiduciary channel (561 nm). In the 3rd figure the black ellipse are circle fitting, red dots are selected-NP localized, and black dots are other localization. Finally, the script generates a histogram showing the frequency of localizations per individual nanoparticle, based on thousands of measurements taken along the imaging chain. The crosses we notice in the images are the centers of each individual nanoparticle. (Figure43 A-E)

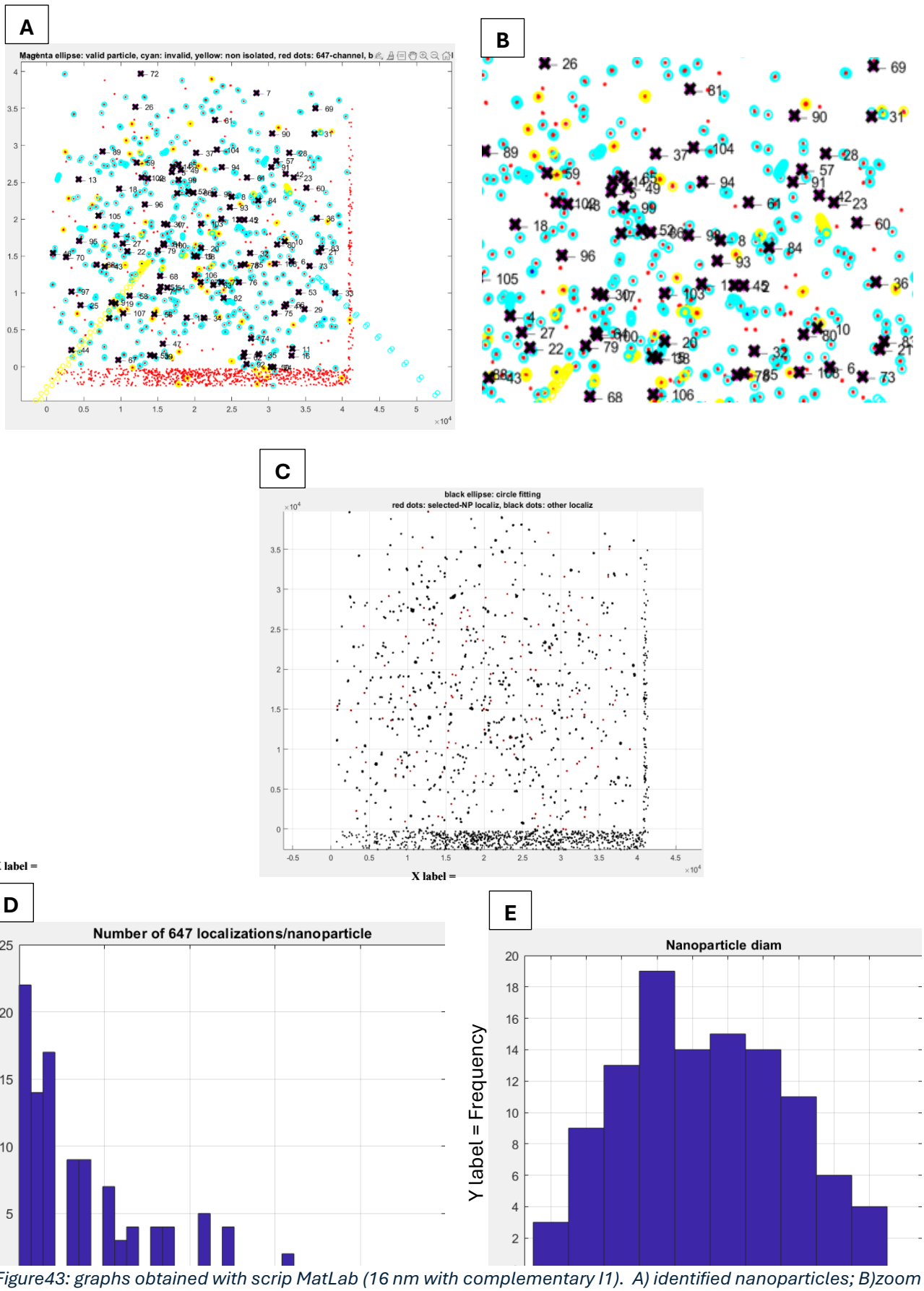

Figure43: graphs obtained with scrip MatLab (16 nm with complementary I1). A) identified nanoparticles; B)zoom of a part of image A; C) black ellipse is the circle fitting, red dots are the selected nanoparticle localization and black dots are the other localizations. (D) histogram showing the frequency of localizations by single nanoparticle. E) histogram showing the size of nanos.

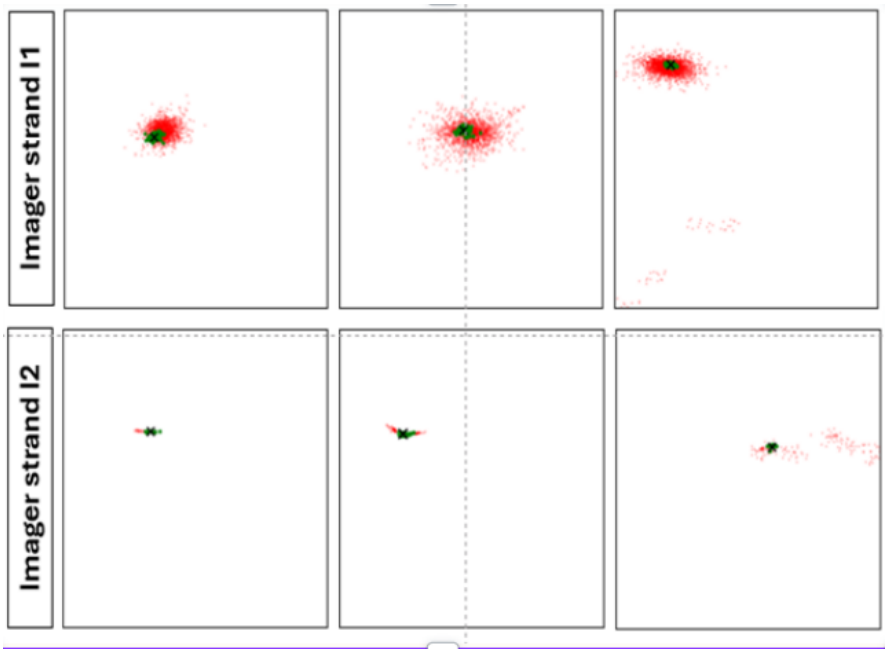

Figure 44: Image obtained by Matlab analysis for 70 nm nanoparticles using two different imager strands I1 and I2.

The first line shows the behavior of the particle when the complementary strand imager I1 is used, which attaches to the nanoparticle. In the second line, what happens when the non-complementary imager 2 is used. This behavior was found more in spherical nanoparticles than in star shaped ones probably because of their irregular shape

4. Conclusions

In this thesis, we focused on the creation and optimization of a one-pot assay applied to be applied in nanomedicine, using barcoded nanoparticles, the decoding of which was performed by DNA-PAINT microscopy. Gold nanoparticles were the focus of our investigation, and through various experiments, we reached several relevant conclusions regarding their synthesis, their conjugation with specific docking strand, and their subsequent detection by DNA-PAINT.

The synthesis of nanoparticles has produced very promising results, particularly for particles of small size and spherical shape. These smaller spherical nanoparticles demonstrated high stability over time, remaining intact for an observation period of two months. In contrast, larger spherical and stellate nanoparticles showed lower colloidal stability, deteriorating over time. This implies that, for such larger particles, it is crucial to proceed quickly with the analysis following their synthesis. In particular, it is advisable to perform DNA-PAINT analysis promptly to prevent the colloidal sample from precipitating, rendering the solution unusable.

Dynamic Light Scattering (DLS), Zeta Potential (ZP) and UV-Vis spectroscopy (UV-Vis) have proven to be effective in verifying the conjugation of docking strands on the surface of nanoparticles. However, both DLS and ZP presented difficulties in obtaining accurate results. This is due to the need to optimize sample dilution; inadequate dilution can lead to inaccurate measurements, thus compromising data interpretation.

A crucial aspect of the work was the optimization of the process of attaching gold nanoparticles to the glass slide for subsequent analysis by DNA-PAINT. It was found that the optimal treatment for the coverslip is to use the APTES reagent, combined with thorough cleaning of the slide using acids. In addition, the incubation period of the nanoparticles on the slide was crucial, which should be extended overnight to ensure effective adhesion of the particles to the surface.

From the image analysis, we evaluated the brightness of each sample at different wavelengths each corresponding to a different laser. It was noticed that the smaller nanoparticles were brighter at 561 nm, which is optimal since the imager we purchased employs 647 nm excitation. In contrast, the larger particles appeared to be brighter at a wavelength of 647 nm. This initially made us doubt the success of the final DNA-PAINT analysis. The larger nanoparticles, however, allow images with better resolution to be obtained and the structures are very clearly visible, which is not the case in N-STORM images of the smaller ones, in which the image is unclear and appears with a lot of background noise, despite then successful subsequent analysis.

Through DNA-PAINT analysis we noticed a clear difference between complementary and noncomplementary filaments in all the different samples. In spherical nanoparticles this difference appeared much more visible. In star-shaped nanoparticles there is not much difference in results when one imager is used rather than another. Generally, spherical nanoparticles showed better performance than star-shaped nanoparticles. This result can be attributed to their regular shape, which probably facilitates the uniform placement of oligonucleotides on the surface of the particles. Indeed, the spherical geometry seems to promote better interaction with DNA strands, thus improving the quality and reliability of detection in PAINT analysis.

In summary, the results obtained provide important indications for the future use of gold nanoparticles in nanomedicine, highlighting the need to adapt synthesis and analysis methodologies according to the specific morphology and size of the particles used.

5. Future developments

In the future, our work will continue with significant efforts toward optimizing the conjugation of gold nanoparticles (AuNPs) with docking strands, especially in the case of non-regularly shaped particles. This is of crucial importance because proper conjugation is the foundation for effective detection and subsequent analysis using the DNA-PAINT technique. Therefore, we will focus not only on perfecting the conjugation techniques but also on the detailed characterization of the nanoparticles with the aim of verifying the efficiency and specificity of the binding between the AuNPs and the docking strands. This characterization will be carried out through the use of advanced techniques such as DLS, ZP and UV-Vis spectroscopy, with the aim of obtaining increasingly precise and reproducible data. Another aspect of great importance will be the optimization of the entire DNA-PAINT analysis procedure. In this context, we aim to examine the performance of AuNPs not only according to their shape and size, but also according to the variety of docking strands used. In addition to this, we also propose to vary the imager strands used during DNA-PAINT analysis. In the present research, we mainly used ATTO-647 imager strands, but we intend to extend the investigation to other fluorophores, such as ATTO-561. This extension will allow us to explore potential differences in emission, stability, and interaction with docking strands, providing a more complete understanding of the molecular dynamics involved. By analyzing similarities and differences between these different imagers, we aim to identify the optimal conditions for each type of nanoparticle, maximizing the effectiveness of the DNA-PAINT technique. In addition, another important step forward will be the

exploration of experiments in which the synthesized nanoparticles will no longer be analyzed individually, but in mixtures containing several different samples. This approach, known as the 'one-pot bar-coded assay', not only allows the detection and localization of individual nanoparticles on the basis of their barcodes, but also offers the practicality of rapid and efficient evaluation of drug-loaded nanoparticles. This novel strategy will allow us to evaluate the ability of AuNPs to simultaneously identify multiple distinct targets, paving the way for multiplex analysis that could revolutionize the field of nanomedicine. The ability to detect and distinguish multiple biomarkers in a single analysis is an ambitious but critical goal for the development of new therapies and more accurate and timely diagnoses. All these optimization processes were designed with the ultimate goal of building a comprehensive and versatile library of AuNPs, characterized by different docking chains optimized for specific biological targets. This preparatory work is essential for the next step in our project: the initiation of in vitro cell culture assays. These tests represent a crucial step in evaluating the future efficacy and future safety of nanoparticles in a complex biological context, bringing us ever closer to the possible clinical application of AuNPs. The long-term goal will then be to develop gold nanoparticles not only as advanced research tools, but as true therapeutic and diagnostic agents for precision medicine [59], [60], [61], [62].

Bibliography

[1] ‘2014 National Nanotechnology Initiative Strategic Plan’.

[2] T. J. Webster, ‘Nanomedicine: what’s in a definition?’, *Int. J. Nanomedicine*, vol. 1, no. 2, pp. 115–116, Jun. 2006.

[3] S. Parveen and S. K. Sahoo, ‘Nanomedicine’, *Clin. Pharmacokinet.*, vol. 45, no. 10, pp. 965–988, Oct. 2006, doi: 10.2165/00003088-200645100-00002.

[4] ‘ESF publishes “forward look” for nanomedicine’, CORDIS | European Commission. Accessed: Sep. 08, 2024. [Online]. Available: https://cordis.europa.eu/article/id/23445-esf-publishes-forward-look-for-nanomedicine

[5] E. H. Chang *et al.*, ‘Nanomedicine: Past, present and future – A global perspective’, *Biochem. Biophys. Res. Commun.*, vol. 468, no. 3, pp. 511–517, Dec. 2015, doi: 10.1016/j.bbrc.2015.10.136.

[6] K. Riehemann, S. W. Schneider, T. A. Luger, B. Godin, M. Ferrari, and H. Fuchs, ‘Nanomedicine—Challenge and Perspectives’, *Angew. Chem. Int. Ed.*, vol. 48, no. 5, pp. 872–897, 2009, doi: 10.1002/anie.200802585.

[7] B. Y. S. Kim, J. T. Rutka, and W. C. W. Chan, ‘Nanomedicine’, *N. Engl. J. Med.*, vol. 363, no. 25, pp. 2434–2443, Dec. 2010, doi: 10.1056/NEJMra0912273.

[8] W. Kang, Y. Liu, and W. Wang, ‘Light-responsive nanomedicine for cancer immunotherapy’, *Acta Pharm. Sin. B*, vol. 13, no. 6, pp. 2346–2368, Jun. 2023, doi: 10.1016/j.apsb.2023.05.016.

[9] T. Andrian, S. Pujals, and L. Albertazzi, ‘Quantifying the effect of PEG architecture on nanoparticle ligand availability using DNA-PAINT’, *Nanoscale Adv.*, vol. 3, no. 24, pp. 6876–6881, doi: 10.1039/d1na00696g.

[10] A. Z. Wang, R. Langer, and O. C. Farokhzad, ‘Nanoparticle Delivery of Cancer Drugs’, *Annu. Rev. Med.*, vol. 63, no. Volume 63, 2012, pp. 185–198, Feb. 2012, doi: 10.1146/annurev-med-040210-162544.

[11] R. Mout, D. F. Moyano, S. Rana, and V. M. Rotello, ‘Surface functionalization of nanoparticles for nanomedicine’, *Chem. Soc. Rev.*, vol. 41, no. 7, pp. 2539–2544, Mar. 2012, doi: 10.1039/C2CS15294K.

[12] G. Pasparakis, ‘Recent developments in the use of gold and silver nanoparticles in biomedicine’, *WIREs Nanomedicine Nanobiotechnology*, vol. 14, no. 5, p. e1817, 2022, doi: 10.1002/wnan.1817.

[13] C. G. Galbraith and J. A. Galbraith, ‘Super-resolution microscopy at a glance’, *J. Cell Sci.*, vol. 124, no. 10, pp. 1607–1611, May 2011, doi: 10.1242/jcs.080085.

[14] N. Sun, Y. Jia, S. Bai, Q. Li, L. Dai, and J. Li, ‘The power of super-resolution microscopy in modern biomedical science’, *Adv. Colloid Interface Sci.*, vol. 314, p. 102880, Apr. 2023, doi: 10.1016/j.cis.2023.102880.

[15] L. Schermelleh *et al.*, ‘Super-resolution microscopy demystified’, *Nat. Cell Biol.*, vol. 21, no. 1, pp. 72–84, Jan. 2019, doi: 10.1038/s41556-018-0251-8.

[16] J. Schnitzbauer, M. T. Strauss, T. Schlichthaerle, F. Schueder, and R. Jungmann, ‘Super-resolution microscopy with DNA-PAINT’, *Nat. Protoc.*, vol. 12, no. 6, pp. 1198–1228, Jun. 2017, doi: 10.1038/nprot.2017.024.

[17] M. Bates, S. A. Jones, and X. Zhuang, ‘Stochastic optical reconstruction microscopy (STORM): a method for superresolution fluorescence imaging’, *Cold Spring Harb. Protoc.*, vol. 2013, no. 6, pp. 498–520, Jun. 2013, doi: 10.1101/pdb.top075143.

[18] M. M. E. Tholen, R. P. Tas, Y. Wang, and L. Albertazzi, ‘Beyond DNA: new probes for PAINT super-resolution microscopy’, *Chem. Commun. Camb. Engl.*, vol. 59, no. 54, pp. 8332–8342, doi: 10.1039/d3cc00757j.

[19] T. Eustaquio, C. L. Cooper, and J. F. Leary, ‘Single-cell imaging detection of nanobarcoded nanoparticle biodistributions in tissues for nanomedicine’, in *Reporters, Markers, Dyes,*

Nanoparticles, and Molecular Probes for Biomedical Applications III, SPIE, Feb. 2011, pp. 93–103. doi: 10.1117/12.874290.
[20] H. Li, C. Lau, and J. Lu, 'Carrier-resolved technology for homogeneous and multiplexed DNA assays in a "one-pot reaction"', *Analyst*, vol. 133, no. 9, pp. 1229–1236, Aug. 2008, doi: 10.1039/B804096F.
[21] 'Come preparare la soluzione salina tamponata con fosfato (PBS)'. Accessed: Sep. 08, 2024. [Online]. Available: https://stjohnslabs.com/how-to-prepare-phosphate-buffered-saline-pbs/?srsltid=AfmBOortkqvaZdmS-VRU1kvo0nUnh2EmacDLkBUSa1mRmC2tDZ1LiniX
[22] 'Nanoparticelle d'oro Proprietà e applicazioni'. Accessed: Sep. 08, 2024. [Online]. Available: https://www.sigmaaldrich.com/IT/it/technical-documents/technical-article/materials-science-and-engineering/biosensors-and-imaging/gold-nanoparticles
[23] J. Fan, Y. Cheng, and M. Sun, 'Functionalized Gold Nanoparticles: Synthesis, Properties and Biomedical Applications', *Chem. Rec. N. Y. N*, vol. 20, no. 12, pp. 1474–1504, Dec. 2020, doi: 10.1002/tcr.202000087.
[24] P. Singh, S. Pandit, V. R. S. S. Mokkapati, A. Garg, V. Ravikumar, and I. Mijakovic, 'Gold Nanoparticles in Diagnostics and Therapeutics for Human Cancer', *Int. J. Mol. Sci.*, vol. 19, no. 7, p. 1979, Jul. 2018, doi: 10.3390/ijms19071979.
[25] G. Frens, 'Controlled Nucleation for the Regulation of the Particle Size in Monodisperse Gold Suspensions', *Nat. Phys. Sci.*, vol. 241, no. 105, pp. 20–22, Jan. 1973, doi: 10.1038/physci241020a0.
[26] J. Polte *et al.*, 'Mechanism of Gold Nanoparticle Formation in the Classical Citrate Synthesis Method Derived from Coupled In Situ XANES and SAXS Evaluation', *J. Am. Chem. Soc.*, vol. 132, no. 4, pp. 1296–1301, Feb. 2010, doi: 10.1021/ja906506j.
[27] S. He, M. W. C. Kang, F. J. Khan, E. K. M. Tan, M. A. Reyes, and J. C. Y. Kah, 'Optimizing gold nanostars as a colloid-based surface-enhanced Raman scattering (SERS) substrate', *J. Opt.*, vol. 17, no. 11, p. 114013, Oct. 2015, doi: 10.1088/2040-8978/17/11/114013.
[28] C. Deriu, A. Bracho, and B. McCord, 'Tailored Colloidal Nanostars for Surface-Enhanced Raman Spectroscopy: Optimization of Formulation Components and Study of the Stabilizer–Nanoparticle Interactions', *J. Phys. Chem. C*, vol. 126, no. 4, pp. 2023–2040, Feb. 2022, doi: 10.1021/acs.jpcc.1c08145.
[29] 'Acqua regia'. Accessed: Sep. 07, 2024. [Online]. Available: https://ehs.princeton.edu/book/export/html/508
[30] 'Aqua Regia', Office of Environmental Health and Safety. Accessed: Sep. 08, 2024. [Online]. Available: https://ehs.princeton.edu/laboratory-research/chemical-safety/chemical-specific-protocols/aqua-regia
[31] D. R. Baer, D. J. Gaspar, P. Nachimuthu, S. D. Techane, and D. G. Castner, 'Application of surface chemical analysis tools for characterization of nanoparticles', *Anal. Bioanal. Chem.*, vol. 396, no. 3, pp. 983–1002, Feb. 2010, doi: 10.1007/s00216-009-3360-1.
[32] N. Raval, R. Maheshwari, D. Kalyane, S. R. Youngren-Ortiz, M. B. Chougule, and R. K. Tekade, 'Chapter 10 - Importance of Physicochemical Characterization of Nanoparticles in Pharmaceutical Product Development', in *Basic Fundamentals of Drug Delivery*, R. K. Tekade, Ed., in Advances in Pharmaceutical Product Development and Research. , Academic Press, 2019, pp. 369–400. doi: 10.1016/B978-0-12-817909-3.00010-8.
[33] S. K. Brar and M. Verma, 'Measurement of nanoparticles by light-scattering techniques', *TrAC Trends Anal. Chem.*, vol. 30, no. 1, pp. 4–17, Jan. 2011, doi: 10.1016/j.trac.2010.08.008.
[34] A. C. Quevedo *et al.*, 'UV-Vis Spectroscopic Characterization of Nanomaterials in Aqueous Media', *JoVE J. Vis. Exp.*, no. 176, p. e61764, Oct. 2021, doi: 10.3791/61764.
[35] W. Wang, X. Ding, Q. Xu, J. Wang, L. Wang, and X. Lou, 'Zeta-potential data reliability of gold nanoparticle biomolecular conjugates and its application in sensitive quantification of surface absorbed protein', *Colloids Surf. B Biointerfaces*, vol. 148, pp. 541–548, Dec. 2016, doi: 10.1016/j.colsurfb.2016.09.021.

[36] F. S. Rocha, A. J. Gomes, C. N. Lunardi, S. Kaliaguine, and G. S. Patience, ‘Experimental methods in chemical engineering: Ultraviolet visible spectroscopy—UV-Vis’, *Can. J. Chem. Eng.*, vol. 96, no. 12, pp. 2512–2517, 2018, doi: 10.1002/cjce.23344.
[37] B. G. Hill, C. Reily, J.-Y. Oh, M. S. Johnson, and A. Landar, ‘Methods for the determination and quantification of the reactive thiol proteome’, *Free Radic. Biol. Med.*, vol. 47, no. 6, pp. 675–683, Sep. 2009, doi: 10.1016/j.freeradbiomed.2009.06.012.
[38] X. Liu, M. Atwater, J. Wang, and Q. Huo, ‘Extinction coefficient of gold nanoparticles with different sizes and different capping ligands’, *Colloids Surf. B Biointerfaces*, vol. 58, no. 1, pp. 3–7, Jul. 2007, doi: 10.1016/j.colsurfb.2006.08.005.
[39] L. M. Demers *et al.*, ‘A Fluorescence-Based Method for Determining the Surface Coverage and Hybridization Efficiency of Thiol-Capped Oligonucleotides Bound to Gold Thin Films and Nanoparticles’, *Anal. Chem.*, vol. 72, no. 22, pp. 5535–5541, Nov. 2000, doi: 10.1021/ac0006627.
[40] T. A. Taton, ‘Preparation of gold nanoparticle-DNA conjugates’, *Curr. Protoc. Nucleic Acid Chem.*, vol. Chapter 12, p. Unit 12.2, Aug. 2002, doi: 10.1002/0471142700.nc1202s09.
[41] H. H. Kyaw, S. H. Al-Harthi, A. Sellai, and J. Dutta, ‘Self-organization of gold nanoparticles on silanated surfaces’, *Beilstein J. Nanotechnol.*, vol. 6, no. 1, pp. 2345–2353, Dec. 2015, doi: 10.3762/bjnano.6.242.
[42] T. Karakouz, B. M. Maoz, G. Lando, A. Vaskevich, and I. Rubinstein, ‘Stabilization of Gold Nanoparticle Films on Glass by Thermal Embedding’, *ACS Appl. Mater. Interfaces*, vol. 3, no. 4, pp. 978–987, Apr. 2011, doi: 10.1021/am100878r.
[43] T. Okamoto and I. Yamaguchi, ‘Optical Absorption Study of the Surface Plasmon Resonance in Gold Nanoparticles Immobilized onto a Gold Substrate by Self-Assembly Technique’, *J. Phys. Chem. B*, vol. 107, no. 38, pp. 10321–10324, Sep. 2003, doi: 10.1021/jp034537l.
[44] H. Weinrib, A. Meiri, H. Duadi, and D. Fixler, ‘Uniformly Immobilizing Gold Nanorods on a Glass Substrate’, *J. At. Mol. Phys.*, vol. 2012, no. 1, p. 683830, 2012, doi: 10.1155/2012/683830.
[45] H. Cho *et al.*, ‘Aptamer-Based SERRS Sensor for Thrombin Detection’, *Nano Lett.*, vol. 8, no. 12, pp. 4386–4390, Dec. 2008, doi: 10.1021/nl802245w.
[46] T. Andrian, P. Delcanale, S. Pujals, and L. Albertazzi, ‘Correlating Super-Resolution Microscopy and Transmission Electron Microscopy Reveals Multiparametric Heterogeneity in Nanoparticles’, *Nano Lett.*, vol. 21, no. 12, pp. 5360–5368, Jun. 2021, doi: 10.1021/acs.nanolett.1c01666.
[47] N. Feiner-Gracia *et al.*, ‘Super-Resolution Microscopy Unveils Dynamic Heterogeneities in Nanoparticle Protein Corona’, *Small*, vol. 13, no. 41, p. 1701631, 2017, doi: 10.1002/smll.201701631.
[48] J. Xu, H. Ma, and Y. Liu, ‘Stochastic Optical Reconstruction Microscopy (STORM)’, *Curr. Protoc. Cytom.*, vol. 81, p. 12.46.1-12.46.27, Jul. 2017, doi: 10.1002/cpcy.23.
[49] ‘N-STORM’, Nikon Instruments Inc. Accessed: Sep. 07, 2024. [Online]. Available: https://www.microscope.healthcare.nikon.com/products/super-resolution-microscopes/n-storm-super-resolution
[50] P. Delcanale and L. Albertazzi, ‘DNA-PAINT super-resolution imaging data of surface exposed active sites on particles’, *Data Brief*, vol. 30, p. 105468, Jun. 2020, doi: 10.1016/j.dib.2020.105468.
[51] M. Kreft, M. Stenovec, and R. Zorec, ‘Focus-drift correction in time-lapse confocal imaging’, *Ann. N. Y. Acad. Sci.*, vol. 1048, pp. 321–330, Jun. 2005, doi: 10.1196/annals.1342.029.
[52] ‘Drift Correction is Illustrated with Imaris and Fast4DReg’, Oxford Instruments. Accessed: Sep. 07, 2024. [Online]. Available: https://andor.oxinst.com/learning/view/article/drift-and-drift-correction-in-time-lapse-microscopy

[53] J. Yguerabide and E. E. Yguerabide, ‘Light-scattering submicroscopic particles as highly fluorescent analogs and their use as tracer labels in clinical and biological applications’, *Anal. Biochem.*, vol. 262, no. 2, pp. 157–176, Sep. 1998, doi: 10.1006/abio.1998.2760.
[54] W. D. Pyrz and D. J. Buttrey, ‘Particle Size Determination Using TEM: A Discussion of Image Acquisition and Analysis for the Novice Microscopist’, *Langmuir*, vol. 24, no. 20, pp. 11350–11360, Oct. 2008, doi: 10.1021/la801367j.
[55] M. Garo, ‘Deviazione Standard: co-protagonista dell’analisi dati’, Mathsly Research. Accessed: Sep. 07, 2024. [Online]. Available: https://www.mathsly.it/wordpress/deviazione-standard-co-protagonista-dellanalisi-dati/
[56] J. C. Potts, A. Jain, D. B. Amabilino, F. J. Rawson, and L. Pérez-García, ‘Molecular Surface Quantification of Multifunctionalized Gold Nanoparticles Using UV–Visible Absorption Spectroscopy Deconvolution’, *Anal. Chem.*, vol. 95, no. 35, pp. 12998–13002, Sep. 2023, doi: 10.1021/acs.analchem.3c01649.
[57] W. Haiss, N. T. K. Thanh, J. Aveyard, and D. G. Fernig, ‘Determination of Size and Concentration of Gold Nanoparticles from UV−Vis Spectra’, *Anal. Chem.*, vol. 79, no. 11, pp. 4215–4221, Jun. 2007, doi: 10.1021/ac0702084.
[58] V. Amendola and M. Meneghetti, ‘Size Evaluation of Gold Nanoparticles by UV−vis Spectroscopy’, *J. Phys. Chem. C*, vol. 113, no. 11, pp. 4277–4285, Mar. 2009, doi: 10.1021/jp8082425.
[59] G. Jarockyte, V. Karabanovas, R. Rotomskis, and A. Mobasheri, ‘Multiplexed Nanobiosensors: Current Trends in Early Diagnostics’, *Sensors*, vol. 20, no. 23, Art. no. 23, Jan. 2020, doi: 10.3390/s20236890.
[60] Q. Ding, W. Qiu, C. Sun, H. Ren, and G. Liu, ‘Comparison of DNA–Gold Nanoparticle Conjugation Methods: Application in Lateral Flow Nucleic Acid Biosensors’, *Molecules*, vol. 28, no. 11, Art. no. 11, Jan. 2023, doi: 10.3390/molecules28114480.
[61] S. Strauss and R. Jungmann, ‘Up to 100-fold speed-up and multiplexing in optimized DNA-PAINT’, *Nat. Methods*, vol. 17, no. 8, pp. 789–791, Aug. 2020, doi: 10.1038/s41592-020-0869-x.
[62] K. Tapio and I. Bald, ‘The potential of DNA origami to build multifunctional materials’, *Multifunct. Mater.*, vol. 3, no. 3, p. 032001, Jul. 2020, doi: 10.1088/2399-7532/ab80d5.

Attachment 1

- ReadCoords2.m script

```
function
    [XCoords647,YCoords647,TCoords647,XCoordsFid,YCoordsFid,TCoordsFid]=
    ReadCoords2(FileName, InputType, varargin)

        %%%%%  READCOORDS: reads raw data from SMLM
        %%%%% read raw data (TXT or CSV) obtained from SMLM analysis in
        %%%%% NIS-elements (Nikon N-STORM) or ONI software, and extract
        %%%%% coordinates of interest for further processing. It
            generates
        %%%%% txt file of 3 columns containing XYT coordinates to use
            for
        %%%%% further processing.
        %%%%%

        %-----------------------------------------------------------
        % INPUTS:
        % FileName: name of the file with extension, e.g. 'MyFile.txt'
        % InputType: denotes the type of file, type 'N-STORM' for Nikon
        % software TXT files, or 'ONI' for CSV files from ONI.
        %
        % N.B.
        % only two-channels can be read: main-channel (named 647) and
        % fiducial markers channels (named Fid). File format should be
        % checked.
        %
        % N-STORM files (TXT) are supposed to be 26-column, columns
            4-5-13 are
        % read as X-Y-T.      %
        % ONI files (CSV) are supposed to be 11-columns, columns 3-4-2
            are
        % read as X-Y-T.
        %
```

```
        %-------------------------------------------------------------
        % OUTPUTS:
        % X-Y-TCoords647: X, Y, T(frames) coordinates of localization
            in
        % the main channel, named 647, expressed in nanometers
        %
        % X-Y-TCoordsFid: X, Y, T(frames) coordinates of localization i
        % the second channel (typically fiducial markers), expressed in
        % nanometers
        %
        %
        %-------------------------------------------------------------

p = inputParser; %init parser object
validChar = @(x) ischar(x);
validNum = @(x) isreal(x);
% here add something to read the coordinate file


%define defaults values for optional param:
defaultSTORMname = '405/647'; % main channel name for N-STORM data
defaultONIname = 1 ; % main channel name for ONI
defaultSTORMref = 'Bead Drift Correction'; % ref channel name for
    N-STORM data
defaultONIref = 0 ; % ref channel name for ONI

%define required and optional input parameters:
addRequired(p,'FileName',validChar);
addRequired(p,'InputType',validChar);

addParameter(p,'STORMname', defaultSTORMname, validChar);
addParameter(p,'STORMref', defaultSTORMref, validChar);
addParameter(p,'ONIname', defaultONIname, validNum);
addParameter(p,'ONIref', defaultONIref, validNum);

%read input values:
parse(p, FileName, InputType, varargin{:});
```

```
%assign the parsed values:
FileName = p.Results.FileName; % file name
InputType = p.Results.InputType;
STORMname = p.Results.STORMname;
STORMref = p.Results.STORMref;
ONIname = p.Results.ONIname;
ONIref = p.Results.ONIref;

switch InputType

    %%%%%%%%%%%%%%%%%%%%%%%%%%%%%%%%%%%%%%%%%%%%%%%%%%%%%%%%%%%%%%%%%%%%%%%
    %%%%------ TXT file from N-STORM ------------------------------
    %%%%%%%%%%%%%%%%%%%%%%%%%%%%%%%%%%%%%%%%%%%%%%%%%%%%%%%%%%%%%%%%%%%%%%%

    case 'N-STORM'

        %%%----- Read text file (check format)---
        disp('Importing N-STORM data...');
        fileID = fopen(FileName,'r');
        DataIn = textscan(fileID,'%s %f %f %f %f %f %f %f %f %f %f %f
            %f %f %f %f %f %f %f %f %f %f %f %f %f
            %f','Delimiter','\t','HeaderLines',1); % Saving data as a
            cell, check the numb of columns
        fclose(fileID);

        %%%--- Retrieve useful information (channel, corrected XY
            location and frame number or the localization)
        XCoords = cell2mat(DataIn(4)); %% colum 2 X non drift
            corrected, 4 X drift corrected
        YCoords = cell2mat(DataIn(5)); %% colum 3 Y non drift
            corrected, 5 Y drift corrected
        TCoords = cell2mat(DataIn(13)); %% column 13 Frame
        Channel = DataIn(1);
        clear DataIn;

        %%%--- Split channel based on first column and generate output
        %%%--- main channel is 647 (first column of TXT file)
        Channel647=strcmp(Channel{1},STORMname);%Check in the .txt if
```

```
    647 or 405/647
XCoords647=XCoords(Channel647);
YCoords647=YCoords(Channel647);
TCoords647=TCoords(Channel647);
ChannelFid=strcmp(Channel{1},STORMref);%Check in the .txt if
    647 or other name
XCoordsFid=XCoords(ChannelFid);
YCoordsFid=YCoords(ChannelFid);
TCoordsFid=TCoords(ChannelFid);

%%%--- Export a txt file with XYT coords
n=length(XCoords647);
nref=length(XCoordsFid);
A=zeros(n,3);
Ref=zeros(nref,3);
A(:,1)=XCoords647;
A(:,2)=YCoords647;
A(:,3)=TCoords647;
Ref(:,1)=XCoordsFid;
Ref(:,2)=YCoordsFid;
Ref(:,3)=TCoordsFid;
save XYTcoordinates.txt A -ascii
save XYTref.txt Ref -ascii


%%%%%%%%%%%%%%%%%%%%%%%%%%%%%%%%%%%%%%%%%%%%%%%%%%%%%%%%%%%%%%%%%%%%%%%%
%%%%------ CSV file from ONI ----------------------------------
%%%%%%%%%%%%%%%%%%%%%%%%%%%%%%%%%%%%%%%%%%%%%%%%%%%%%%%%%%%%%%%%%%%%%%%%

case 'ONI'

    %%%----- Read text file (check format)---
    disp('Importing ONI data...');
    fileID = fopen(FileName,'r');
    DataIn = textscan(fileID,'%f %f %f %f %f %f %f %f %f %f
        %f','Delimiter',',','HeaderLines',1); % Saving data as a
        cell, check the numb of columns
    fclose(fileID);
```

```
%%%--- Retrieve useful information (channel, corrected XY
    location and frame number or the localization)
XCoords = cell2mat(DataIn(3)); %% colum 3 X coords
YCoords = cell2mat(DataIn(4)); %% colum 4 Y coords
TCoords = cell2mat(DataIn(2)); %% column 2 Frame coords
Channel = DataIn(1);
clear DataIn;


%%%--- Split channel based on first column and generate output
Channel647= (Channel{1}==ONIname); % 647-channel with 1
XCoords647=XCoords(Channel647);
YCoords647=YCoords(Channel647);
TCoords647=TCoords(Channel647);
ChannelFid= (Channel{1}==ONIref);%C Fiducial-channels denoted
    with 0
XCoordsFid=XCoords(ChannelFid);
YCoordsFid=YCoords(ChannelFid);
TCoordsFid=TCoords(ChannelFid);

%%%--- Export a txt file with XYT coords
n=length(XCoords647);
nref=length(XCoordsFid);
A=zeros(n,3);
Ref=zeros(nref,3);
A(:,1)=XCoords647;
A(:,2)=YCoords647;
A(:,3)=TCoords647;
Ref(:,1)=XCoordsFid;
Ref(:,2)=YCoordsFid;
Ref(:,3)=TCoordsFid;
save XYTcoordinates.txt A -ascii
save XYTref.txt Ref -ascii

%%%%%%%%%%%%%%%%%%%%%%%%%%%%%%%%%%%%%%%%%%%%%%%%%%%%%%%%%%%%%%%%%%%%%%%
%%%------ CSV file from Thunderstorm ----------------------
%    %%%%%%%%%%%%%%%%%%%%%%%%%%%%%%%%%%%%%%%%%%%%%%%%%%%%%%%%%%%%%%%%%%%
```

```
%
    case 'THUNDER'

        %%%----- Read text file (check format)---
        disp('Importing Thunder data...');
        fileID = fopen(FileName,'r');
        DataIn = textscan(fileID,'%f %f %f %f %f %f
            %f','Delimiter',',','HeaderLines',1); % Saving data as a
            cell, check the numb of columns
        fclose(fileID);

        %%%--- Retrieve useful information (channel, corrected XY
            location and frame number or the localization)
        XCoords = cell2mat(DataIn(3));
        YCoords = cell2mat(DataIn(4));
        TCoords = cell2mat(DataIn(2));
        XCoordsFid = 0;
        YCoordsFid = 0;
        TCoordsFid = 0;
%         Channel = DataIn(1);
        %clear DataIn;


        %%%--- Split channel based on first column and generate output
        %Channel647= (Channel{1}==1); % 647-channel denoted with 1
        XCoords647=XCoords;
        YCoords647=YCoords;
        TCoords647=TCoords;
%         ChannelFid= (Channel{1}==0);%C Fiducial-channels denoted
    with 0
%         XCoordsFid=XCoords(ChannelFid);
%         YCoordsFid=YCoords(ChannelFid);
%         TCoordsFid=TCoords(ChannelFid);
%
    otherwise
        disp('invalid InputType!');
end
end
```

- Cluster2.m script

```
function [C, ClustSize,
    Loc2particleMain]=Cluster2(FileNameMain,FileNameRef, Bandwidth,
    MinPts, MaxDiam, Maxdistance, varargin)
%%%%%%%%%%%%%%%%%%%%%%%%%%%%%%%%%%%%%%%%%%%%%%%%%%%%%%%%%%%%%%%%%%%%%%%%
%%%%%% CLUSTER2: perform mean-shift clustering of (X,Y,T) coordinates
    of REFERENCE
%%%%%% channel in order to roughly identify centers of valid
    particles.
%%%%%% Then, the localizations in MAIN channel within a defined
    distance
%%%%%% from centers are stored.
%%%%%%%%%%%%%%%%%%%%%%%%%%%%%%%%%%%%%%%%%%%%%%%%%%%%%%%%%%%%%%%%%%%%%%%%

%%%%%% REQUIRED INPUTS:
%%%%%% FileNameMain: txt file with XYT coords of main channel, in nm
    and frames
%%%%%% FileNameRef: txt file with XYT coords of ref channel, in nm
    and frames
%%%%%% bandwidth: parameter for clustering, in nm
%%%%%% MinPts: minimum number of localiz in a cluster
%%%%%% MaxDiam: maximum diameter (longest axis), in nm
%%%%%% Maxdistance: maximum distance between particle center and
%%%%%% localization in main channel to be considered attached, in nm

%%%%%% OPTIONAL INPUTS:
%%%%%% Elong: max ellipse elongation allowed, default=10.0
%%%%%% ScaleFactor: scale factor in ellipse fit, default=1.0
%%%%%% MinClustDist: minimum distance between clusters (in nm),
    default=300
%%%%%% AggrDist: minimum distance between clusters to be
    non-aggregates (in
%%%%%% nm), default like MinClustDist

%%%%%% OUTPUTS:
```

```
%%%%%% Loc2particleMain: cell array with XYT of MAIN channel for each
    selected
%%%%%% cluster
%%%%%% C: XY coordinates of detected particles centers
%%%%%% ClustSize: for each selected cluster, number of counted
%%%%%% localizations in the MAIN channel
%%%%%%%%%%%%%%%%%%%%%%%%%%%%%%%%%%%%%%%%%%%%%%%%%%%%%%%%%%%%%%%%%%%%%%%

%%%%%%%%% beginning of function...%%%%%%%%%%%%%%%%%%%%%%%%%%%

%%% Parse input data ======================================

tic

p = inputParser; %init parser object
validNum = @(x) isnumeric(x) && (x > 0); %define valid inputs:
    positive num
validChar = @(x) ischar(x);

%define defaults values for optional param:
defaultElong = 10.0; %elongation in ellipse fit
defaultScaleFactor= 1.0; %scale factor in ellipse fit
defaultMinClustDist = 300; % min distance between clusters
defaultAggrDist = defaultMinClustDist; % min distance between
    clusters to be non-aggregate, by default like MinClustDist

%define required and optional input parameters:
addRequired(p,'FileNameMain',validChar);
addRequired(p,'FileNameRef',validChar);
addRequired(p,'Bandwidth',validNum);
addRequired(p,'MinPts',validNum);
addRequired(p,'MaxDiam', validNum);
addRequired(p,'Maxdistance', validNum);

addParameter(p,'Elong', defaultElong, validNum);
addParameter(p,'ScaleFactor', defaultScaleFactor, validNum);
addParameter(p,'MinClustDist', defaultMinClustDist, validNum);
addParameter(p,'AggrDist', defaultAggrDist, validNum);
```

```
%read input values:
parse(p,FileNameMain, FileNameRef, Bandwidth, MinPts, MaxDiam,
    Maxdistance, varargin{:});

%assign the parsed values:
Last = Inf; % Limit the number of points processed (set to Inf to
    process all)
MaxParticleElongation = p.Results.Elong; % max elongation allowed in
    ellipse fit
EllipseFitScaleFactor = p.Results.ScaleFactor; % scale factor in
    ellipse fit
MinClustDst = p.Results.MinClustDist; % min distance of closest
    cluster to be considered isolated
distanceAggregates = p.Results.AggrDist; % min distance between
    clusters to be non-aggregate

% % if not introduced, by default distance aggregate is set as
    MinClustDst:
% if (MinClustDst ~= defaultMinClustDist) && (distanceAggregates ==
    defaultAggrDist)
%     distanceAggregates = defaultMinClustDist;
%


%%% Read coordinates ========================================

disp('Reading data...');

% read XYT coords on MAIN channel in txt file:
CoordinatesMain=importdata(FileNameMain);
% %%%read txt with more complex file structure:
% % delimiterIn = ' ';
% % headerlinesIn = 1;
% % Coordinates = importdata(FileNameMain,delimiterIn,headerlinesIn);

% assign X-Y-T coordinates of MAIN channel:
XCoords647 = CoordinatesMain(:,1); %X coords in first column
```

```
YCoords647 = CoordinatesMain(:,2); %Y coords in second column
TCoords647 = CoordinatesMain(:,3); %T coords in third column

% read XYT coords on REF channel in txt file:
CoordinatesRef=importdata(FileNameRef);
% %%%read txt with more complex file structure:
% % delimiterIn = ' ';
% % headerlinesIn = 1;
% % Coordinates = importdata(FileNameRef,delimiterIn,headerlinesIn);

% assign X-Y-T coordinates of REF channel:
XCoordsFid = CoordinatesRef(:,1); %X coords in first column
YCoordsFid = CoordinatesRef(:,2); %Y coords in second column
%TCoordsFid = CoordinatesRef(:,3); %T coords in third column


% Plot raw coordinates data:
XCoords647 = XCoords647(1:min(Last,numel(XCoords647)));
YCoords647 = YCoords647(1:min(Last,numel(YCoords647)));
XCoordsFid = XCoordsFid(1:min(Last,numel(XCoordsFid)));
YCoordsFid = YCoordsFid(1:min(Last,numel(YCoordsFid)));
plot(XCoords647,YCoords647,'.r'); axis equal; hold on;
plot(XCoordsFid,YCoordsFid,'.b'); axis equal;
hold on;

%%% Clustering in REF channel ============================

% Clustering using mean-shift:
disp('Clustering...');
PtsFid = [XCoordsFid YCoordsFid];
[clustCentFid,~,clustMembsCellFid] =
    MeanShiftCluster(PtsFid.',Bandwidth);
%ClustSizeFid = cellfun(@numel, clustMembsCellFid);
NClustFid = numel(clustMembsCellFid);
disp(strcat(['Found ' num2str(NClustFid) ' clusters in Fid
    channel']));

% Flag isolated Nanoparticles
```

```
[D, ~] = pdist2(clustCentFid',clustCentFid','euclidean','Smallest',2);
isolatedFid = (D(2,:) >= MinClustDst);

%%% Filter by localization number and elongation ===============

disp('Filtering...');

 IndexRightClustFid=false(NClustFid,1); % Initialization logical
     array to identify valid clusters
 RightClustFid=1:1:NClustFid; % Intialization cluster indexes;
 massCenter=clustCentFid; %Initialization centers coords of clusters;
r=0;
for i = 1 : NClustFid
    A = [XCoordsFid(cell2mat(clustMembsCellFid(i)))';
        YCoordsFid(cell2mat(clustMembsCellFid(i)))' ];
    if(size(A,2) >= MinPts)
        % Filter particle based on ellipse elongation & major axis
            length
        % Plot ellipse as reference
        ellipse_t =
            fit_ellipse(A(1,:),A(2,:),gcf,EllipseFitScaleFactor,
            MaxParticleElongation,MaxDiam, isolatedFid(i));
        valid = ellipse_t.valid;
        if valid == 1
            IndexRightClustFid(i)=true; % Indentify as true the valid
                cluster (numb points and elongation)
        end
    else
      disp(strcat( ['#' num2str(i) ' cluster has few localizations
          and has been excluded']));
      r=r+1;
    end
end

%filter indexes and centers by localiz N and elongation
RightClustFid=RightClustFid(IndexRightClustFid);
massCenter=massCenter(:,IndexRightClustFid);
```

```
disp(strcat( [num2str(NClustFid-length(RightClustFid)-r) ' clusters
    have been excluded due to unrealistic size or elongation']));

hold on
plot(massCenter(1,:), massCenter(2,:), 'xk', 'LineWidth',3,
    'MarkerSize',10);
%this is to visualize the label of the identified clusters
for i = 1 : length(massCenter)
txt1 = ['\leftarrow ' num2str(i)];
text(massCenter(1,i),massCenter(2,i),txt1)
end


%%% Filter particle too close /aggregates ===============

distanceCenters=pdist2(massCenter',massCenter'); %euclidean dist
    between previously filtered cluster centers
[rows,~]=find((distanceCenters~=0) &
    (distanceCenters<distanceAggregates)); %index of clusters closer
    than threshold dist
AggregateMember= rows';
Aggregates=RightClustFid(AggregateMember); %store the index of
    previously filtered clusters corresponding to aggregates
AggrMembr=clustMembsCellFid(Aggregates); %for every aggregate which
    points are in it
RightClustFid(AggregateMember)=[]; %filter index of clusters
    corresponding to aggregates
NPMembs=clustMembsCellFid(RightClustFid); %for every selected cluster
    which points are in it
NPSizeFid = cellfun(@numel, NPMembs); % for each selected cluster,
    counts the number of points in it

disp(strcat( [num2str(length(AggregateMember)) ' clusters have been
    excluded because were forming aggregates']));
disp(strcat(['Identified ' num2str(length(RightClustFid)) '
    nanoparticles candidates from ' num2str(NClustFid) ' candidate
    clusters']));
```

```
figure(2)
hold on
for i=1: length(Aggregates)
    AggregateData=[XCoordsFid(cell2mat(AggrMembr(i))),
        YCoordsFid(cell2mat(AggrMembr(i)))];
    plot(AggregateData(:,1), AggregateData(:,2), 'xy')
end


%%% Size Check ========================================

DataType='SolidSphere';
nclusters=length(RightClustFid);
%SizeCheck=zeros(nclusters,1);
C=zeros(nclusters,2);
R=zeros(nclusters,1);
Rcheck=zeros(nclusters,1);
RCheckLow=5;
RCheckHigh=400;
discard=0;
IndexToRemove=true(nclusters,1); % Pietro: logical array to remove
    index of cluster discarded
for i=1:nclusters
    switch DataType
        %case 'HollowSphere'
           %
               [C(i,1),C(i,2),R(i)]=circfit(StoreClusterCoords{i,1}(:,1),
               StoreClusterCoords{i,1}(:,2));
        case 'SolidSphere'
            ClusterData=[XCoordsFid(cell2mat(NPMembs(i))),
                YCoordsFid(cell2mat(NPMembs(i)))];
            plot(ClusterData(:,1), ClusterData(:,2), 'xg')
            Cinitial=[mean(ClusterData(:,1)) mean(ClusterData(:,2))];
            FracThreshold=0.85;
            CovMat=cov(ClusterData);
            Rinitial=1.5*mean([sqrt(CovMat(1,1)) sqrt(CovMat(2,2))]);

            % Now the location of the center of the smallest sphere
```

```
% encompassing 95% of the datapoints is determined.
CenterSampleSizeAz=10; CenterSampleSizeRad=4;
CenterLocation=zeros(CenterSampleSizeAz+1,2,CenterSampleSizeRad);
TrackLocNumber=zeros(CenterSampleSizeAz+1,CenterSampleSizeRad);

for n=1:CenterSampleSizeRad
    t2 = linspace(0,2*pi,CenterSampleSizeAz);
    XCurrentCircle=0.05*n*Rinitial*cos(t2)+Cinitial(1);
    YCurrentCircle=0.05*n*Rinitial*sin(t2)+Cinitial(2);
    for o1=1:CenterSampleSizeAz
            CenterLocation(o1,:,n)=[XCurrentCircle(o1)
                YCurrentCircle(o1)];
            LocDistCheck=find(((ClusterData(:,1)-
                XCurrentCircle(o1)).^2+(ClusterData(:,2)-
                YCurrentCircle(o1)).^2) < Rinitial^2);
            TrackLocNumber(o1,n)=length(LocDistCheck);
    end
end

RefLocCheck=find(((ClusterData(:,1)-Cinitial(1)).^2+
    (ClusterData(:,2)-Cinitial(2)).^2) < Rinitial^2);
RefLocNumber=length(RefLocCheck);
MaxLoc=max(max(TrackLocNumber));
if MaxLoc > RefLocNumber
    [I,J]=find(TrackLocNumber==MaxLoc);
    MaxLocMinRadTemp=[I J];
    MaxLocMinRadInd=find(J==min(J));
    MaxLocMinRad=MaxLocMinRadTemp(MaxLocMinRadInd,:);
    Cfinal=mean(CenterLocation(MaxLocMinRad(:,1),:,min(J)),1);
else
    Cfinal=Cinitial;
end

RadiusVec=linspace(0,3*Rinitial,1500);
RadiusNumLoc=zeros(length(RadiusVec),1);
for p=1:length(RadiusVec)
    LocDistCheckRad=find(((ClusterData(:,1)-Cfinal(1)).^2+
        (ClusterData(:,2)-Cfinal(2)).^2) < RadiusVec(p)^2);
```

```
            RadiusNumLoc(p)=length(LocDistCheckRad);
        end

        RadTrack=1;
        while RadiusNumLoc(RadTrack) < FracThreshold *
            size(ClusterData,1)
            RadTrack=RadTrack+1;
        end
        Rfinal=RadiusVec(RadTrack);

        C(i,:)=Cfinal';
        Rcheck(i)=Rfinal;
    end
    if Rcheck(i) >= RCheckLow && Rcheck(i) <= RCheckHigh
        R(i)=Rfinal;
    else
        disp(['Cluster #' num2str(i) ' has been excluded from the
            analysis due to an unrealistic size:'
            num2str(round(Rcheck(i))*2)])
        IndexToRemove(i) = false; % Pietro: collect the indexes of the
            clusters to remove
        discard=discard+1;
    end
end
disp(strcat(['Identified ' num2str(nclusters-discard) ' valid
    nanoparticles from ' num2str(nclusters) ' candidate
    nanoparticles']));
NPselect= R~=0;
R=R(NPselect);
R=round(R);
C=[C(NPselect,1), C(NPselect,2)];
NPSizeFid = NPSizeFid(IndexToRemove); %Pietro: remove the discarded
    cluster
%NPMembs=NPMembs(IndexToRemove); %Pietro: remove discarded clusters,
    after size check

for m=1:length(R)
      t = linspace(0,2*pi,100);
```

```
    plot(R(m)*cos(t)+C(m,1),R(m)*sin(t)+C(m,2),'k','LineWidth', 1)
    hold on
%     axis image
    %axis([C(m,1)-500 C(m,1)+500 C(m,2)-500 C(m,2)+500])
end

%%% Identifying localizations in MAIN around each center=====

disp('Creating output...');

A=[XCoords647 YCoords647 TCoords647];
Loc2particleMain = cell(length(C),1); %init: for every REF particle
    which MAIN-localiz are around, also 0 localizations are included
figure(2)
hold on
plot(XCoords647,YCoords647,'.k'); axis equal; hold on;
for k = 1:length(C)
    distanceMassCenter = pdist2(C(k,:), [XCoords647 YCoords647]); %
        distance between center and all the MAIN-localiz
    Close = (distanceMassCenter <= Maxdistance); % select
        MAIN-localiz closer than Maxdistance
    ClosePoint=A(Close,:);
    %DistClose=distanceMassCenter(Close);
    %Y = prctile(DistClose,100);              % option for a further
        selction of points within a percentage
    %Select=DistClose < Y;
    %DistAttach=DistClose; %(Select);
    Localization=ClosePoint; %(Select,:);
    Loc2particleMain{k} = Localization;
    plot(Maxdistance*cos(t)+C(k,1),Maxdistance*sin(t)+C(k,2),'r',
        'LineWidth', 1)
    hold on
    plot(ClosePoint(:,1), ClosePoint(:,2), 'c.'); hold on;
    plot(Localization(:,1), Localization(:,2), 'r.'); hold on;
    %this is to visualize the label of the identified clusters
    txt2 = ['\leftarrow ' num2str(k)];
    plot(C(k,1), C(k,2), 'xk', 'LineWidth',1, 'MarkerSize',5); hold
        on;
```

```
    text(C(k,1),C(k,2),txt2)
end

title({'black ellipse: circle fitting';'Green dots: NP, red dots: 647
    attached to NP, black dots: 647 other'});grid on;axis equal;

% Statistics
ClustSize = cellfun(@numel, Loc2particleMain); %how many MAIN-localiz
    for particle
ClustSize=ClustSize/3; %IMPORTANT! Because count 1 localization as 3
    (3 coordinators)
figure(6);hist(ClustSize,60);grid on;title('Number of 647
    localizations/nanoparticle');
%save('Data','ClustSize','-append')

toc

end
```

Ringraziamenti